



Virginia Commonwealth University
VCU Scholars Compass

Theses and Dissertations


Graduate School

2019

Nanostructured Materials for Photocatalysis, Water Treatment and Solar Desalination

Hiran D. Kiriarachchi
Virginia Commonwealth University

Follow this and additional works at: <https://scholarscompass.vcu.edu/etd>

 Part of the [Materials Chemistry Commons](#), and the [Physical Chemistry Commons](#)

© The Author

Downloaded from

<https://scholarscompass.vcu.edu/etd/5886>

This Dissertation is brought to you for free and open access by the Graduate School at VCU Scholars Compass. It has been accepted for inclusion in Theses and Dissertations by an authorized administrator of VCU Scholars Compass. For more information, please contact libcompass@vcu.edu.

Nanostructured Materials for Photocatalysis, Water Treatment and Solar Desalination

A dissertation submitted in partial fulfillment of the requirements for the degree of
Doctor of Philosophy at Virginia Commonwealth University

By

Hiran Danushka Kiriarachchi

B.S., University of Kelaniya, Kelaniya, Sri Lanka, 2013

Director: M. Samy El-Shall

Professor, Department of Chemistry

Virginia Commonwealth University

Richmond, Virginia

May 2019

©Hiran Danushka Kiriarachchi 2019

All Rights Reserved

Acknowledgment

First, I would like to acknowledge my beloved parents Chandra Jatungama and Chandrasiri Kiriarachchi, my endearing wife Shamara Weeraratne, my sister Hishani Kiriarachchi, my parents-in-law Lakshman Weeraratne and Kanthi Ruhunage, and my sister-in-law Samadhi Weeraratne for their constant encouragement, support, and unconditional love. I wouldn't have been here without them.

I would like to extend my sincere gratitude to my advisor Dr. M. Samy El-Shall for his guidance and encouragement. I am extremely thankful for him for accepting me into his lab and mentoring me to become a competent individual. His remarkable passion for chemistry and never-ending thirst to venture new fields of research motivated me so much and it helped me to build my character and gain various skills. I appreciate the support and constructive criticism provided by my thesis committee: Dr. James Turner who, although no longer with us, continues to inspire me by his example, Dr. Indika U. Arachchige, Dr. Sally S. Hunnicutt and Dr. Shiv N. Khanna. I am extremely grateful to Dr. Indika U. Arachchige for guiding me throughout these years and letting me use the facilities in his lab. I am also thankful to Dr. Khaled Abouzeid, Dr. Amr Awad, Dr. Amr Hassan and Dr. Longli Bo for their mentorship and guidance and Dr. Ümit Özgür in the School of Engineering for the instrumental facilities provided.

I would also like to express my sincere gratitude to Dr. Fathi Awad for his research collaborations and for being such a wonderful person. I also take this opportunity to thank Dr. Julian Bobb and Dr. Andrew Lin for their support with the instrument handling and training. I'm also thankful for current and former members of the El-Shall group, Ayyob Bakry, Mrinmoy Das, Atanu Giri, Vitaly Kisurin, Kyle Mason, Adam Percy and Zachary Christensen for their support and making

my life in the lab so joyful. A special thank should go to Dr. Joseph Turner for his assistance and guidance in the instrumental facility. I would like to be thankful to all the administrative staff especially to Rhea Miller, Joia Nesby, John Arnold, Michael Morris, Edith Allin and Joann Williams for being such nice a group of people and assisting me in numerous ways. I am also thankful to all my Sri Lankan friends in Richmond for their support and making my stay in VCU so homely.

Finally, I would like to extend my sincere gratitude to my two aunts, Thilaka Jathungama and Sriyalatha Kiriarachchi for supporting me through difficult times of my life and Dr. Shyamal Premaratne for his mentorship. I am forever grateful for your encouragement and support through out this venture.

Table of Contents

List of Figures	x
List of Tables	xv
List of Abbreviations	xvi
Abstract	xviii
Chapter 01: Introduction	1
1.1. Fundamental Principles of Water Desalination	2
1.1.1. Solar Stills and Their Limitations	3
1.1.2. The Utility of Photothermal Materials to Increase the Efficiency	7
1.2. Fundamental Principles of Semiconductor Photocatalysis	11
1.2.1. Mechanism of ZnO Photocatalysis	12
1.3. An Overview of Heavy Metal Removal	15
Chapter 02: Characterization Techniques	18
2.1. X-ray Diffraction	18
2.2. X-ray Photoelectron Spectroscopy	19
2.3. Transmission Electron Microscopy	20
2.4. Scanning Electron Microscopy	20
2.5. Fourier Transform Infrared Spectroscopy	21
2.6. UV-Visible Spectroscopy	22
2.7. Raman Spectroscopy.....	22

Chapter 03: Plasmonic Graphene Polyurethane Nanocomposites for Efficient Solar Water Desalination	24
3.1. Introduction.....	24
3.2. Materials and Methods.....	27
3.2.1. Materials	27
3.2.2. Material Preparation.....	27
3.2.3. Characterization of Materials.....	28
3.2.4. Solar Steam Generation Experiments	29
3.2.5. Solar Water Desalination Tests.....	30
3.2.6. Solar Steam Generation Recycling Experiments	30
3.3. Results and Discussion	31
3.4. Conclusions.....	46
Chapter 04: Plasmonic Chemically Modified Cotton Nanocomposite Fibers for Efficient Solar Water Desalination and Wastewater Treatment	48
4.1. Introduction.....	48
4.2. Materials and Methods.....	49
4.2.1. Materials	49
4.2.2. Material Preparation.....	49
4.2.3. Characterization	50
4.2.4. Solar Steam Generation Experiments	50

4.2.5. Solar Water Desalination Experiments	51
4.2.6. Wastewater Treatment	51
4.2.7. Solar Steam Generation Recycling Experiments	52
4.3. Results and Discussion	52
4.4. Conclusions.....	65
Chapter 05: Low-Cost Functionalized Carbonized Cotton Device for Efficient Solar Steam Generation.....	66
5.1. Introduction.....	66
5.2. Materials and Methods.....	67
5.2.1. Materials	67
5.2.2. Material Preparation.....	68
5.2.3. Characterization	69
5.2.4. Solar Steam Generation Experiments	69
5.2.5. Wastewater Treatment	70
5.2.6. Recycling Study of the CC Solar Steam Generation Device	70
5.3. Results and Discussion	70
5.4. Conclusions.....	78
Chapter 06: Growth Mechanism of “Sea Urchin” ZnO Nanostructures and their Photocatalytic Activity for the Degradation of Organic Dyes.....	79
6.1. Introduction.....	79

6.2. Materials and Methods.....	81
6.2.1. Materials	81
6.2.2. Preparation of ‘Sea Urchin’ Shaped ZnO Nanorod Clusters	81
6.2.3. Characterization of Materials.....	82
6.2.4. Photocatalytic Experiments	82
6.3. Results and Discussion	83
6.3.1. Material Characterization.....	83
6.3.2. Photocatalytic Activity of ZnO Nanorods and SU ZnO Nanorod Clusters	90
6.4. Conclusions.....	93
Chapter 07: Iron Carbide and Aminated Graphene Oxide Composite for Chromium Removal in Wastewater.....	95
7.1. Introduction.....	95
7.2. Materials and Methods.....	97
7.2.1. Materials	97
7.2.2. Material Preparation.....	97
7.2.3. Characterization	99
7.2.4. Cr (VI) Removal Experiments	99
7.3. Results and Discussion	101
7.3.1. Material Characterization.....	101
7.3.2. Removal of Cr (VI) from Aqueous Solution by Fe ₅ C ₂ NPs	111

7.4. Conclusions.....	119
Chapter 08: Summary and Conclusions.....	120
References.....	124
Vita.....	145

List of Figures

Figure 1.1. Different types of water desalination technologies.	2
Figure 1.2. Schematic of basic solar still	4
Figure 1.3. Solar irradiance spectrum at airmass 1.5G	5
Figure 1.4. Schematic diagrams of (A) multi-effect basin still, (B) diffusion still and (C) wick still. ^{6, 13}	6
Figure 1.5. Origin of SPR due to the interaction of delocalized electrons with the electric field of the incident light.	9
Figure 1.6. Different SPR bands observed in different shapes of Au NPs ¹⁵	10
Figure 1.7. General steps involved in heterogeneous photocatalytic oxidation ⁴⁶	12
Figure 1.8. General steps involved in a photocatalytic mechanism. (1) excitons are formed upon irradiation, (2) recombination of excitons (radiative or non-radiative decay), (3) An oxidative pathway is initiated by the holes in the valence band, (4) A reduction pathway is initiated by the electrons in the conduction band, (5) Photocatalytic reactions yield mineralized products.	13
Figure 3.1. The experimental set up of the solar steam generation measurement unit. (A) Schematic representation of the steam generation setup during the experiment. (B) An actual image of the solar simulator when it is switched off.	29
Figure 3.2. Design strategy and general steps involved in the synthesis of the PGPU nanocomposite foam.	32
Figure 3.3. (A) XRD patterns and (B) FTIR spectra of GO and TDI-GO nanosheets.	33
Figure 3.4. (A) XRD patterns and (B) UV-Vis absorption spectra of Au-GO-PU, Ag-GO-PU and Ag/Au-GO-PU composites.	35
Figure 3.5. SEM images of the Au-PU foam (top) and Au-GO-PU (bottom).	36
Figure 3.6. TEM images of the Au-PU nanocomposite.....	37
Figure 3.7. Optical images of the solar absorber foams: (1) PU (polyurethane), (2) Ag-PU (0.2 wt% Ag in PU), (3) Au-PU (0.2 wt% Au in PU), (4) Ag/Au-PU (0.1 wt% Ag and 0.1 wt% Au in PU), (5) GO-PU (0.5 wt% GO in PU), (6) Ag-GO-PU (0.2 wt% Ag, 0.5 wt% GO in PU), (7) Au-GO-PU (0.2 wt% Au, 0.5 wt% GO in PU, and (8) Ag/Au-GO-PU (0.1 wt% Ag, 0.1 wt% Au, 0.5 wt% GO in PU. Each sample is 6 cm in diameter and 1.5 cm in thickness.....	39

Figure 3.8. Steam generation from water surface using different solar absorbers and photothermal converters under one sun illumination.	40
Figure 3.9. Solar evaporation of different foam samples using solar simulator with light densities of (A) 1 kWm^{-2} (optical concentration $C_{\text{opt}} = 1$), and (B) 5 kWm^{-2} (optical concentration $C_{\text{opt}} = 8$). (C) 8 kWm^{-2} (optical concentration $C_{\text{opt}} = 8$) (D) Temperature change at the surface of different foam absorbers and DI water after solar illumination for 30 min under optical concentrations of $C_{\text{opt}} = 5$ and 8.	42
Figure 3.10. Solar-to-vapor efficiency of (A) different PGPU samples at solar intensities of 1, 5 and 8 sun and (B) of the Ag/Au-GO-PU foam in comparison with other reported photothermal conversion materials.	44
Figure 3.11. (A) Concentrations of three primary ions in the synthesized seawater sample determined by ICP-OES before and after SWD using the Ag/Au-GO-PU foam. (B) The evaporation cycle performance of the Ag/Au-GO-PU foam under constant illumination of 5 sun for 30 min for each cycle.	46
Figure 4.1. Design strategy and general steps involved in the synthesis of PFC samples.....	53
Figure 4.2. The difference of the hydrophilicity of the pure cotton and TDI functionalized cotton.	54
Figure 4.3. FT-IR spectra of pure cotton and TDI functionalized cotton. (A) Full scale, (B) Expanded region between 1500 cm^{-1} and 1900 cm^{-1}	55
Figure 4.4. UV-Vis absorption spectra of (A) Au-f-C, (B) Ag-f-C nanocomposite fibers and (C) Solar spectral irradiance (AM 1.5 G) with the UV-Vis absorption spectra of the Au-f-C and Ag-f-C fibers (inset).....	56
Figure 4.5. XPS spectra of the Au 4f electron (A) and the Ag 3d electron (B) in the Au-f-C and Ag-f-C fibers, respectively.....	57
Figure 4.6. SEM images of nanoparticle free functionalized cotton fibers (A and B), Au-f-C nanocomposites (C and D) and Ag-f-C nanocomposites (E-G). The scale bars of the images A to G are 100, 10, 5, 0.5, 5, 1 and $0.5 \mu\text{m}$, respectively.	58
Figure 4.7. Visual images of the PFC samples during the steam generation experiment.....	59
Figure 4.8. Solar steam generation data for different PFC samples under different solar intensities (A) 1 kW m^{-2} (optical concentration $C_{\text{opt}} = 1$), and (B) 5 kW m^{-2} (optical concentration $C_{\text{opt}} = 5$). (C) 5 kW m^{-2} (optical concentration $C_{\text{opt}} = 5$) and (D) Temperature change at the surface of different PFC samples and DI water after solar illumination for 30 min under optical concentrations of $C_{\text{opt}} = 8$	60

Figure 4.9. The evaporation efficiency of different PFC samples under 1, 5, and 8 kW m ⁻² solar illumination.	62
Figure 4.10. (A) The concentrations of three primary metal ions in an artificial seawater sample before and after desalination and (B) Recyclability test of the Ag/Au-f-C sample during 10 cycles under constant illumination of 5 kW m ⁻² for 30 minutes.	64
Figure 4.11. Applications of the PFC materials (Ag/Au-f-C as the representative sample) in wastewater treatment. (A) Stability of the Ag/Au-f-C sample in extreme pH values (pH 2 and 10) and (B) UV-vis spectra of the model pollutant methylene blue, before the steam generation experiment and after condensation of the steam.	65
Figure 5.1. Schematic representation of the solar evaporation setup.....	68
Figure 5.2. FT-IR spectra of pure cotton and acid treated CC.....	71
Figure 5.3. XPS survey spectra of CC before and after acid treatment (A), C 1s spectra of CC before (B) and after (C) acid treatment.	72
Figure 5.4. SEM images of PC fibers (A), (B) and CC (C), (D)	73
Figure 5.5. Raman spectrum of CC.....	74
Figure 5.6. Optical properties of the CC material. (A), the reflectance spectrum of CC and (B), percentage absorbance of CC in comparison with.....	75
Figure 5.7. Solar steam generation data for CC, PC and DI water at solar intensities of (A), 1 kW m ⁻² (1 sun) and (B), 8 kW m ⁻² (8 sun). (C), The solar-to-vapor evaporation efficiency of CC, PC and DI water. (D), the Surface temperature profile of CC, PC and DI water at 8 sun.	76
Figure 5.8. (A), UV visible spectra of 10 ppm MB dye solution and collected condensed steam sample, a photograph of the setup is shown in the inset and (B), Recyclability test of the CC device during 10 cycles of constant solar irradiation under the solar intensity of 5 sun.....	78
Figure 6.1. TEM and SEM images of ZnO seeds (a, b and c, d respectively).....	83
Figure 6.2. TEM images showing the sequential growth of ZnO seeds at different time intervals, 5 minutes (A), 15 minutes (B), 30 minutes (C), 60 minutes (D) and respective UV-Vis spectra (E).	84
Figure 6.3. TEM images showing the sequential growth of ZnO seeds in the presence of CTAB at different time intervals, 5 minutes (A), 15 minutes (B), 30 minutes (C), 60 minutes (D) and respective UV-Vis spectra (E).	85
Figure 6.4. TEM image (A) and SEM image (B) of SU ZnO nanorod clusters, TEM images showing the sequential growth of SU ZnO at different stages, 0 min (C), 15 min (D), 30 min (E),	

60 min (F) and UV/vis spectra of the SU ZnO at different growth time intervals (G)..... 86

Figure 6.5. TEM images of ZnO rods synthesized with CTAB capped ZnO seeds (A, B) and the UV-Vis spectrum (C)..... 88

Figure 6.6. XRD patterns of SU ZnO (A), ZnO seeds (B) and TEM images showing how the seeds transformed into SU shaped ZnO. 89

Figure 6.7. Raman spectra for SU ZnO and ZnO rods. 90

Figure 6.8. Photocatalytic activity of SU ZnO in degrading organic dyes (A) Rh B, (B) IC, (C) MB and (D) the apparent rate constants for the photodegradation of Rh B, IC and MB. 91

Figure 6.9. Comparison of photocatalytic activities of SU ZnO and ZnO rods prepared using CTAB capped ZnO seeds in photodegrading Rh B. (A and B) UV-visible spectra of Rh B showing photodegradation by SU ZnO and ZnO rods respectively and (C and D) kinetic plots of the photodegradation reaction by SU ZnO and ZnO rods respectively. 93

Figure 7.1. TEM images of Fe₅C₂ NPs synthesized using OAm 102

Figure 7.2. Magnified TEM images of the Fe₅C₂ rods indicating the carbon shell 103

Figure 7.3. TEM images of the Fe₅C₂ samples obtained at different stages of the reaction. (A), after reaching 180 °C, (B) and (C), After reaching 350 °C and (D), 20 minutes after reaching 350 °C. 104

Figure 7.4. TEM images of Fe₅C₂ NPs synthesized using OAm to OAc molar ratio of 7:2 106

Figure 7.5. TEM images of Fe₅C₂ NPs synthesized using OAm to OAc molar ratio of 14:1 ... 107

Figure 7.6. XRD of Fe₅C₂ NPs synthesized using (A) OAm and (B) mixture of OAc and OAm (1:14 molar ratio) 108

Figure 7.7. XPS data for Fe₅C₂ NPs synthesized using (A and B) OAm and (C and D) OAm/OAc (14:1)..... 109

Figure 7.8. Raman spectra of Fe₅C₂ NPs synthesized using (A) OAm and (B) OAm/OAc (14:1) 110

Figure 7.9. Room temperature magnetization dependence on external magnetic field for Fe₅C₂ NPs..... 111

Figure 7.10. (A) Effect of pH of the solution on the removal of Cr (VI) by Fe₅C₂, IGO-NH₂, and Fe₅C₂-IGO-NH₂ nanocomposite. (Conditions: C₀ = 22 mg/L for Fe₅C₂ nanoparticles, and 25 mg/L for IGO-NH₂, and Fe₅C₂-IGO-NH₂ nanocomposite. T= 273 K, Adsorbent dose = 0.005 g in 5 mL and (B) visual images of solutions of Cr(VI) at different pH values (from left to right pH 1, 2, 4, 6

and 8). 112

Figure 7.11. The effect of the initial concentration of Cr(VI) on the removal by Fe_5C_2 , IGO- NH_2 , and Fe_5C_2 -IGO- NH_2 nanocomposite. (Conditions: $[\text{Cr(VI)}] = 0.5 - 250 \text{ mg/L}$, $T = 273\text{K}$, $\text{pH} = 2$ for Fe_5C_2 , Fe_5C_2 -IGO- NH_2 and $\text{pH} = 3$ for IGO- NH_2 , Adsorbent dose = 0.005 g/5 mL) 113

Figure 7.12. The effect of contact time on the removal of Cr(VI) by Fe_5C_2 , IGO- NH_2 , and Fe_5C_2 -IGO- NH_2 nanocomposite. (Conditions: $[\text{Cr(VI)}] = 22, 50, 100$ for Fe_5C_2 , IGO- NH_2 , and Fe_5C_2 -IGO- NH_2 respectively. $T = 273 \text{ K}$, $\text{pH} = 2$ for Fe_5C_2 , Fe_5C_2 -IGO- NH_2 nanocomposite, $\text{pH} = 3$ for IGO- NH_2 , Adsorbent dose = 0.005 g/5 mL) 115

Figure 7.13. Effect of adsorbent dose on the removal of Cr(VI) by Fe_5C_2 , IGO- NH_2 , and Fe_5C_2 -IGO- NH_2 nanocomposite. (Conditions: $[\text{Cr(VI)}] = 10, 50, 100$ for Fe_5C_2 , Fe_5C_2 -IGO- NH_2 , IGO- NH_2 , respectively. $T = 273 \text{ K}$, $\text{pH} = 2$ for Fe_5C_2 and Fe_5C_2 -IGO- NH_2 nanocomposite, $\text{pH} = 3$ for IGO- NH_2 , Adsorbent dose = $0.005 - 0.03 \text{ g/10 mL}$) 116

List of Tables

Table 3.1. Steam generation rates of DI water, pure PUF and all the PGPU samples at different solar intensities.....	43
Table 7.1. Desorption studies of Cr(VI) from at pH 10 using NaOH after the adsorption of 15, 50 and 100 mg/L of Cr(VI).....	117
Table 7.2. Comparison of the adsorption capacities of various adsorbents for Cr(VI) removal	118

List of Abbreviations

1D	One dimensional
2D	Two dimensional
3D	Three dimensional
BET	Brunauer–Emmett–Teller
CC	Carbonized cotton
CTAB	Cetyltrimethylammonium bromide
DI	Deionized
DMF	Dimethylformamide
GO	Graphene oxide
HTA	Hexamethylenetetramine
IC	Indigo carmine
ICP-OES	Inductively coupled plasma optical emission spectroscopy
IGO	Improved graphene oxide
IGO-NH ₂	Aminated improved graphene oxide
MB	Methylene blue
MWI	Microwave irradiation
NHE	Normal hydrogen electrode
NIR	Near infra-red
NP	Nanoparticle
OAc	Oleic acid
OAm	Oleylamine
PC	Pristine cotton
PFC	Plasmonic functionalized cotton
PGPU	Plasmonic graphene polyurethane
PU	Polyurethane
PUF	Polyurethane foam

PXRD	Powder X-ray diffraction
RGO	Reduced graphene oxide
Rh B	Rhodamine b
SEM	Scanning electron microscope
SPR	Surface plasmon resonance
SU	Sea urchin
SWD	Seawater desalination
TDI	Toluene diisocyanate
TEM	Transmission electron microscope
UV	Ultra violet
VSM	Vibrating-sample magnetometer
XPS	X-ray photoelectron spectroscopy

Abstract

NANOSTRUCTURED MATERIALS FOR PHOTOCATALYSIS, WATER TREATMENT AND SOLAR DESALINATION

By: Hiran Danushka Kiriarachchi

A dissertation submitted in partial fulfillment of the requirements for the degree of Doctor of Philosophy at Virginia Commonwealth University.

Virginia Commonwealth University, 2019

Director: M. Samy El-Shall, Professor, Department of Chemistry

Maintaining a constant supply of clean drinking water is among the most pressing global challenges in our time. About one-third of the population is affected by the water scarcity and it can only get worse with climate change, rapid industrialization, and the population growth. Even though nearly 70 percent of the planet is covered by water, the consumable freshwater content is only 2.5 percent of it. Unfortunately, the accessible portion of it is only 1 percent. Even so, most of the freshwater bodies are choked with pollution. Considering the vast availability of saline water on the planet and the increasing wastewater generation, seawater desalination, and wastewater treatment and recycling seem to have the potential to address current water-related issues. Therefore, it is necessary to find efficient techniques for seawater desalination and wastewater treatment. The use of nanostructured materials for these applications is becoming a popular approach due to the unique chemical and physical properties they possess compared to bulk materials

Solar energy is the cleanest and most abundant renewable natural resource available. Materials for solar photothermal energy conversion are highly sought after for their cost savings, clean

environment, and broad utility in providing water heating and/or steam for many applications including domestic water heating and solar-driven desalination. Extensive research efforts have been made to develop efficient solar absorbers with characteristics such as low weight, low thermal conductivity, broad solar absorption and porosity to be able to float on water to provide more efficient and cost-effective solar steam generation systems. Metal NPs have been proposed to take advantage of the high efficiency of the photothermal energy conversion associated with surface plasmon resonance absorption. Nanostructured carbon-based materials such as graphene oxide, carbon nanotubes, carbonized biomass are also in use due to their excellent photothermal energy conversion ability over the range of the visible and near infra-red region of the electromagnetic spectrum.

In this dissertation, five projects based on the utility of nanostructured materials for desalination, photocatalysis and water treatment will be discussed. The first three projects involve the fabrication and design of plasmonic and carbon-based photothermal materials for applications in solar steam generation, water desalination, and wastewater treatment. In the fourth project, a unique shape of ZnO nanostructure was synthesized for photodegradation of organic dyes in industrial wastewater. The final project demonstrates the shape-controlled synthesis of iron carbide nanostructures and composite materials of aminated graphene oxide for the removal of Cr(VI) from wastewater.

Chapter 01: Introduction

For a considerable portion of the world population, access to safely managed water is not a certainty. During the last few decades, fast-growing demand for freshwater has become a serious threat to the sustainability of human society. In a recent annual risk report presented by the World Economic Forum, the water crisis was mentioned as the largest global risk in the modern era in terms of potential impact.¹ Accelerated population growth, industrial expansion, improved living standards, and large-scale irrigation agriculture are considered as the key reasons for the high demand for freshwater.²⁻³

Even though 70% of the earth surface is covered with water, the distribution of freshwater on the planet is extremely uneven. Despite the fact that most of the water content on the planet is brackish, the total amount of freshwater on the planet is more than necessary to fulfill the global freshwater demands. Unfortunately, the majority of the earth's freshwater content is not readily accessible. About 69% of the total freshwater content is trapped as glaciers/ice caps and 30% is hidden underneath the earth crust as groundwater.⁴ The available surface freshwater bodies are choked with pollution due to the release of untreated wastewater by municipal and industrial sources. According to the United Nations World Water Development Report, 2017, it is estimated that about 80% of the wastewater worldwide (more than 95% in some of the developing countries) is released to the natural environment without any treatment.⁵ The consequences of these actions are affecting communities all over the world. During the last decade, a considerable number of research efforts have been dedicated to utilizing nanotechnology to find solutions related to water scarcity and pollution. This dissertation will mainly focus on the use of nanostructured materials to solve water-related issues by solar water desalination photocatalysis and water treatment.

1.1. Fundamental Principles of Water Desalination

Considering the vast abundance of seawater (~97% of the total water content) on our planet, desalination seems to be the most sensible solution for the current freshwater crisis. Desalination process involves the extraction and removal of salts and minerals from saline water to produce potable water or water that is low in total dissolved solids. There are about 15,000 large scale desalination units established around the world and the production capacity of them exceeds 8.5 billion gallons per day.⁶ In general, desalination techniques can be categorized into two main classes: (1) techniques based on the phase change of water/distillation through evaporation and (2) filtration through membranes. Figure 1.1 illustrates the currently used desalination techniques in the world.⁷

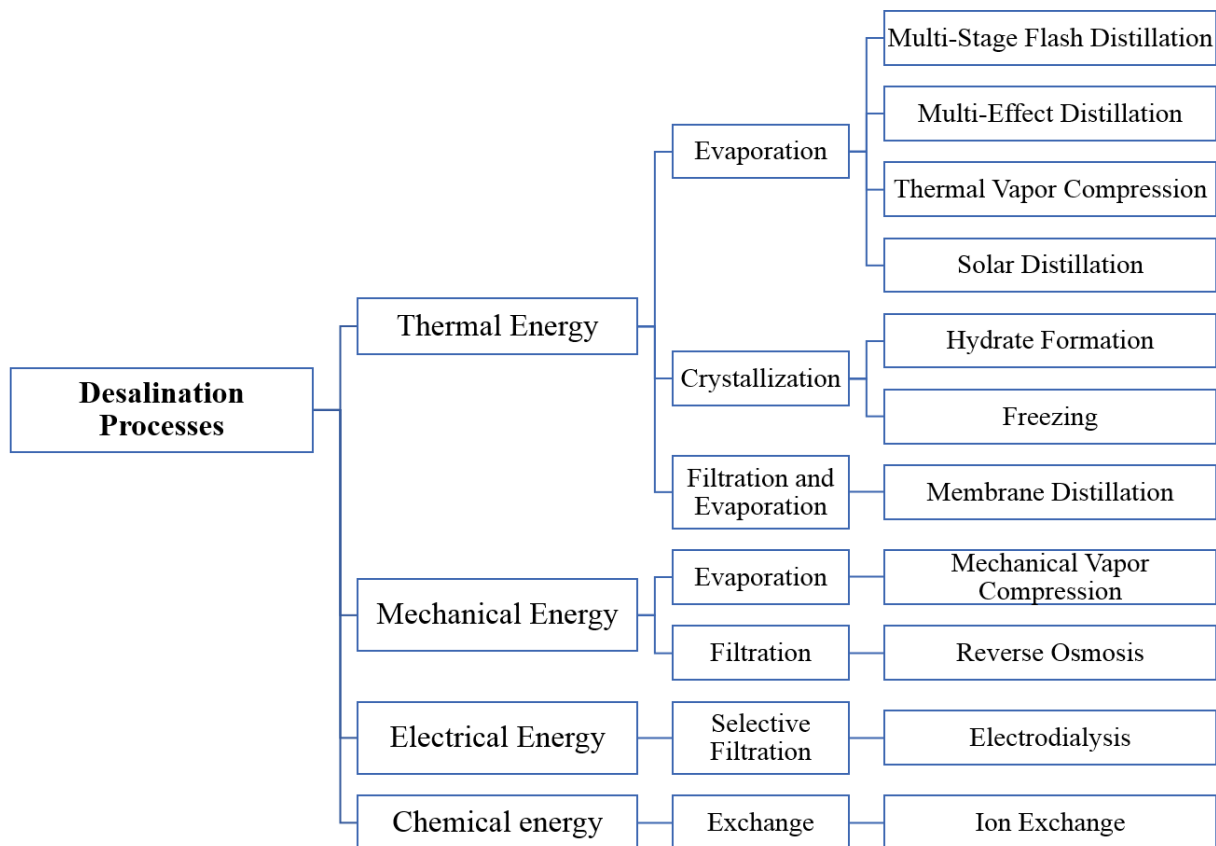


Figure 1.1. Different types of water desalination technologies.

Considering the production capacity, reverse osmosis is the leading technology to date representing 44% of the total capacity. Thermal technologies such as multi-stage flash distillation (40%), multiple-effect desalination (4%) and vapor compression (3%) and membrane processes such as electrodialysis (6%) share the rest.⁶ However, the high energy demand associated with these techniques is a major concern. Most of the energy requirements for desalination are coming from fossil fuel which is one of the key sources for climate change. Therefore, renewable energy-based water desalination techniques are ideal considering both the production cost and the environmental impact.

Solar energy is the cleanest and most abundant energy source available. Therefore, solar water desalination seems to be the most ideal solution to address the current water crisis. Solar desalination is not a new technology and it has been used for centuries by humankind. In fact, the first reports of seawater desalination date back to ancient Greece where Aristotle (384–322 BC) writes about seawater desalination: “Saltwater when it turns into vapor becomes sweet, and the vapor does not form salt water when it condenses again. This is known by experiment”.⁸ Since then numerous research efforts have been devoted to invent efficient solar desalination devices.

1.1.1. Solar Stills and Their Limitations

Currently, solar energy is used in two forms for desalination applications: as electrical energy using photovoltaic arrays to indirectly heat water or as thermal energy to directly heat water.⁹ The use of thermal energy is cost-effective but suffers from low productivity. However, a group of devices called solar stills utilizes solar thermal energy to convert saline water into potable water in a similar way how the sun generates rain. A simplified schematic of a solar still is illustrated in Figure 1.2. First, saline or brackish water is contained in a sealed chamber with a transparent roof. IR radiation of the sunlight passes through the glass roof and heats up the water promoting

evaporation. Then, this vapor is condensed on the glass roof and can be collected for consumption after minimal treatment. The most basic type of solar still is called the basin type which is the oldest and the least productive model. There are two main reasons for the low productivity of the basin type solar stills. Owing to the fact that water has a large specific heat capacity ($4.2 \text{ kJ kg}^{-1} \text{ }^{\circ}\text{C}^{-1}$), energy loss to heat bulk water is a major drawback. Most of the energy entered into the solar still is consumed to increase the temperature of the bulk water but not to generate steam. Also, all the basic solar stills are only harnessing the IR radiation of the solar spectrum which is not the spectral region with the highest irradiance level.

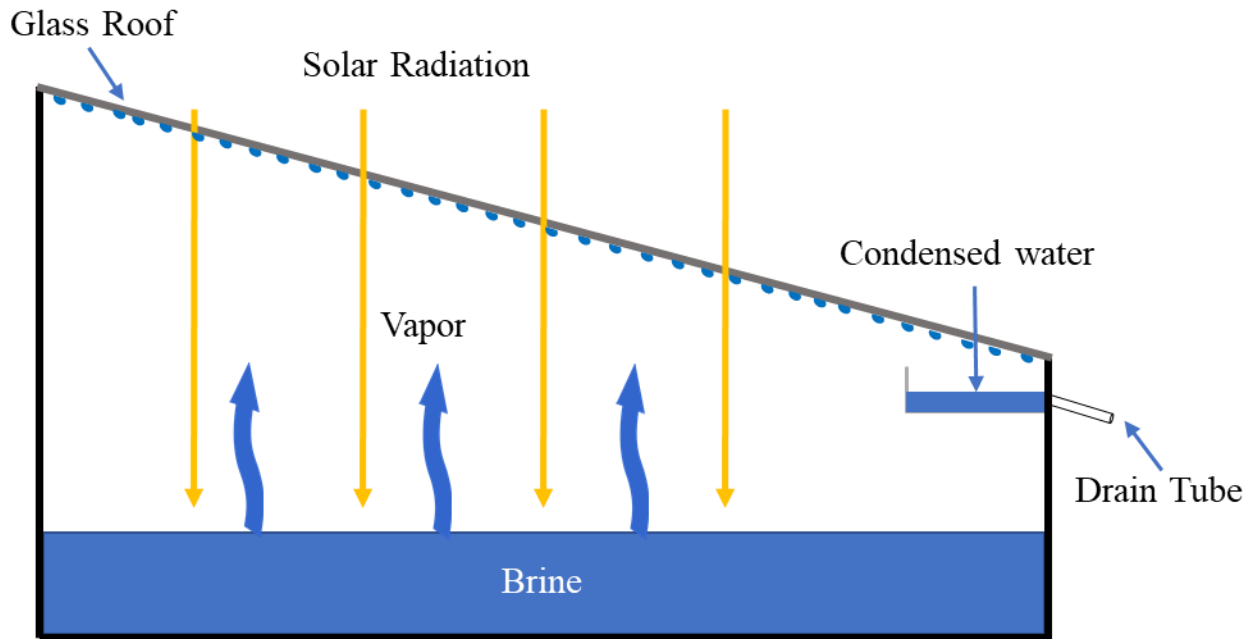


Figure 1.2. Schematic of basic solar still

Figure 1.3 shows the solar irradiance spectrum (AM 1.5G) and where the IR region is located.¹⁰

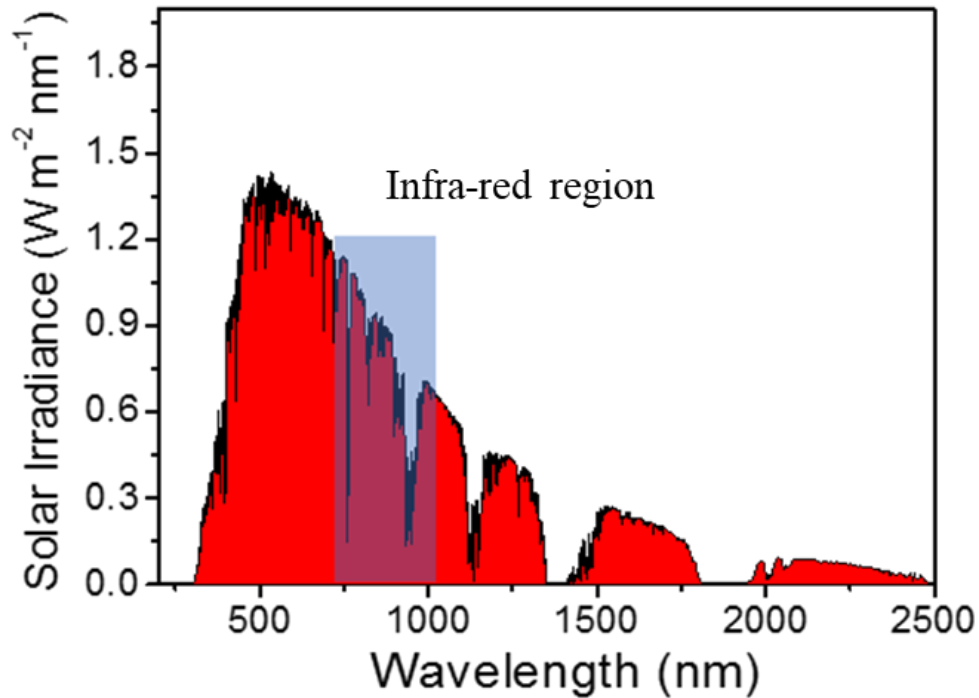


Figure 1.3. Solar irradiance spectrum at airmass 1.5G

However, a new set of solar stills were introduced with modifications in the design to address some of the limitations associated with the basin type solar stills. Wick stills, multiple-effect basin stills, and diffusion stills are a few examples for improved solar still designs. Wick still addresses the issue of bulk heating present in basin type solar stills by using capillary forces to drive water to the irradiation surface which is a thin layer of hydrophilic material. The main reason for the high efficiency of wick stills is the efficient heating of water due to the slow rate of feed input. Also, the tilted bed of the wick system results in low reflectance of solar radiation. Multiple-effect basin stills utilize the heat of evaporation to heat up bulk water by using multiple layers placed on top of each other. The water in the bottom basin evaporates and condenses on the bottom surface of the reservoir above. During the condensation, the heat of the vapor is transferred to the basin above which will increase the evaporation rate of the second basin. This dual action will increase the productivity of the system compared to the single layer systems.^{9, 11} A diffusion still is made of

two units, a distillation chamber and a heat storage unit connected to a solar collector. Distillation chamber has several closely packed cells called multiple effect-diffusion units. Each cell consists of a heating surface and a porous material which is attached on one side of the heating plate. The saline feedwater is supplied to the wick (porous material) from the top. The heating surface absorbs latent heat from the condensing vapor and conducts the heat through the plate to the saturated porous wick at the other side to evaporate the water. The vapor diffuses and condenses on the heating plate of the next cell. The processes cycles until the heat dissipate to the external environment.¹²⁻¹³ Figure 1.4 shows the schematic representations of the three solar stills discussed above.

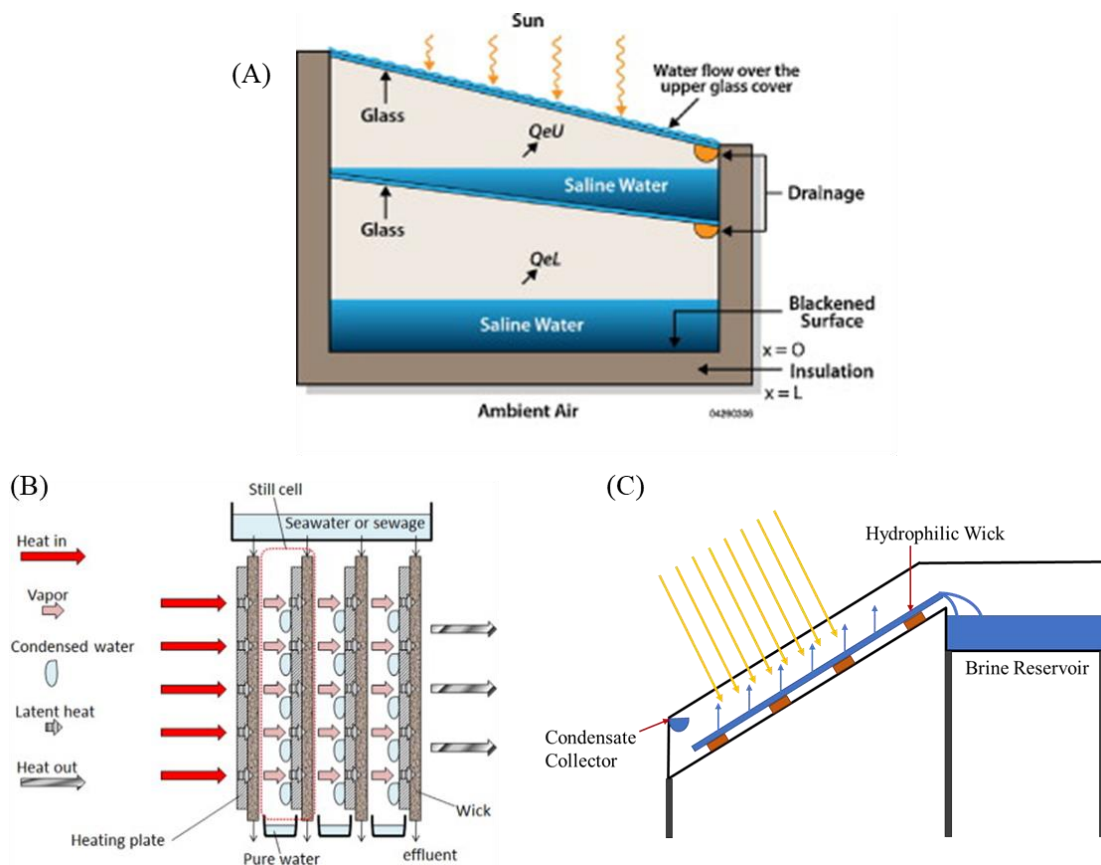


Figure 1.4. Schematic diagrams of (A) multi-effect basin still, (B) diffusion still and (C) wick still.^{6, 13}

Even after the modifications, the energy efficiency of the current solar stills fails to reach more than 50% and the daily production of freshwater is ranging from 4-6 L m⁻².¹¹ Most of the input energy is still consumed to heat the bulk water but not to generate steam. Therefore, it is necessary to incorporate an efficient solar absorber that can efficiently evaporate water without heating up the bulk reservoir.

1.1.2. The Utility of Photothermal Materials to Increase the Efficiency

With the rapid advancement in the fields of material science and nanotechnology, scientists started to incline towards nanomaterials that can efficiently convert light energy into heat to be utilized in solar steam desalination applications. Especially, carbon-based materials such as graphene-based materials and plasmonic NPs have shown promising results in efficient photothermal energy conversion. In fact, our lab is one of the pioneers to demonstrate the utility of GO/RGO nanosheets and Au NPs for efficient heating of bulk water under the laser and solar irradiation.¹⁴⁻¹⁶ In 2012, Naomi J. Halas and her research group in Rice University introduced the principles and applications of photothermal energy conversion of plasmonic and carbon-based NPs to generate steam by localized heating.¹⁷ Since then, a plethora of advanced photothermal materials is introduced for applications such as sewage treatment, distillation and especially for solar water desalination.

To be an efficient solar steam generation device, there are two very important properties that the desired material should possess. Most importantly the photothermal material should be able to harness a broad region of the solar spectrum. Secondly, the material should float on the surface of the water and channel the bulk water to the irradiation surface. It is highly important to have a minimal amount of water in contact with the solar absorber, so the generated heat will be enough to instantaneously vaporize the water to generate steam. In this dissertation, mainly the utility of

plasmonic metal NPs (Au and Ag) and carbon-based materials (GO and carbonized cellulose) incorporated with polymer supports for solar water desalination and wastewater treatment will be demonstrated.

1.1.2.1. Plasmonic Metal Nanoparticles and Surface Plasmonic Resonance

Heat generation upon illumination is a well-known effect observed in metals and this effect is wavelength independent within the optical range for bulk metals. Also, it does not depend on the crystal size or shape. However, this phenomenon is completely different and complicated when it comes to metal NPs. In the subwavelength scale, the light induced heating in metal NPs becomes strongly dependent on both the illumination wavelength and size and shape of the NP.¹⁸ When the particle size of the metals drops below the mean free path the scattering from the bulk minimizes. Thus, all the interactions are expected to be limited to the surface. If the particle size of the NP is below the illumination wavelength, the delocalized electron density of the NPs can strongly couple with the electromagnetic radiation via a phenomenon called surface plasmon resonance. In SPR, delocalized electrons interact with the electric field of the incident radiation and polarize to one surface and oscillate in resonance with the frequency of the incident light (Figure 1.5) When the size and the geometry of the NP changes, it causes changes in the electric field density on the surface. These changes result in different oscillation frequencies of the free electrons giving rise to different absorption bands in the UV-visible absorption spectrum.¹⁹

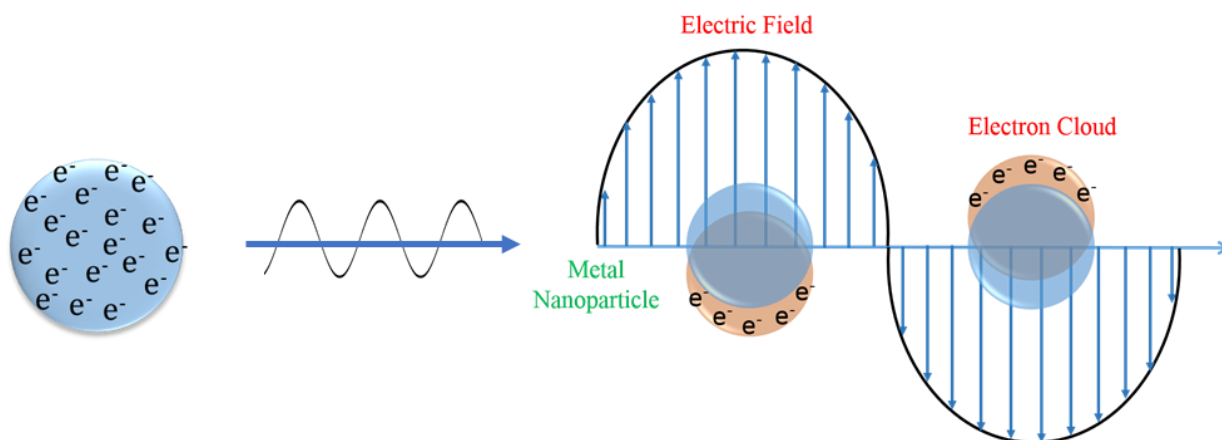


Figure 1.5. Origin of SPR due to the interaction of delocalized electrons with the electric field of the incident light.

Figure 1.6 shows the different SPR bands observed in different shapes of Au NPs. It is a clear observation of size and shape dependence of the resonance frequency observed in metal NPs. When the plasmonic NPs are excited on resonance, the absorbed energy can be dissipated in two ways. Namely, luminescence (emission of photons) and non-radiative decay (Landau damping/emission of phonons).²⁰ To be utilized as an efficient photothermal material for solar steam generation, metal NPs should have a large absorption efficiency and low luminescence quantum yield to ensure efficient light-to-heat energy conversion. Au, Ag, and Pt are ideal candidates due to their chemical inertness and outstanding photothermal properties. However, Cu, Al and In NPs have also been used as cost-effective options but the susceptibility for surface oxidation limits them from long term applications.²¹⁻²³

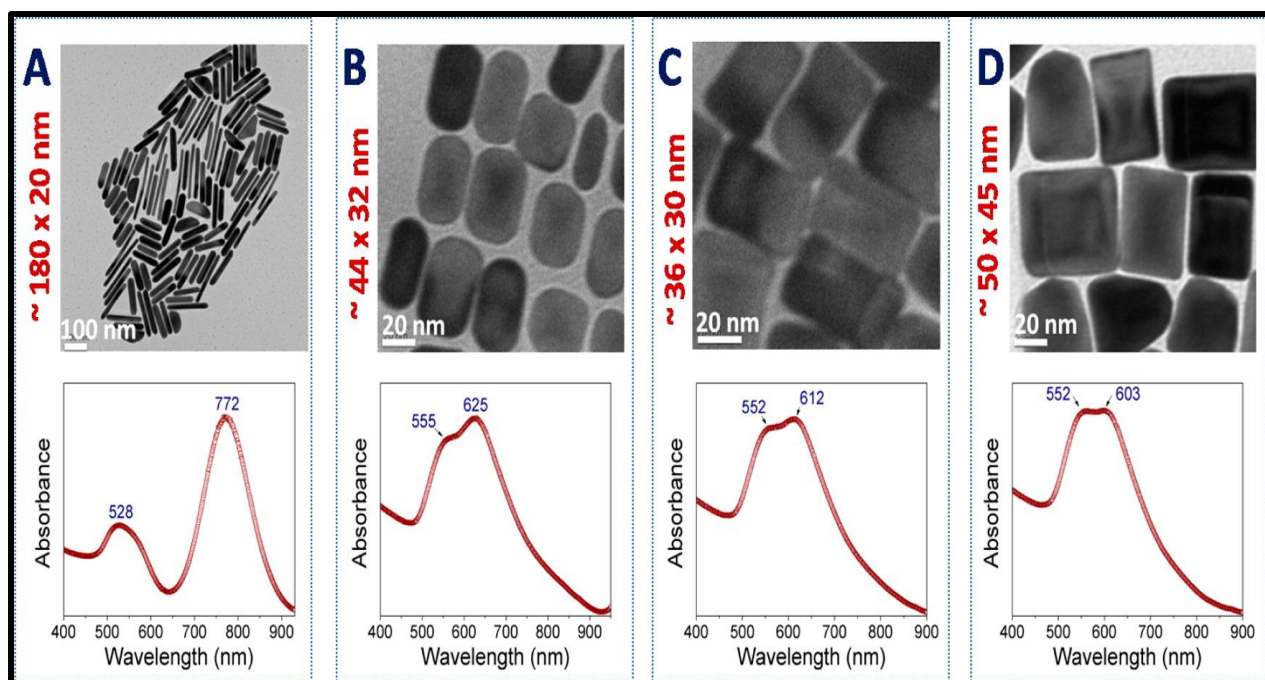


Figure 1.6. Different SPR bands observed in different shapes of Au NPs¹⁵

1.1.2.2. Carbon Based Materials as Photothermal Materials

Among the solar absorbers used for solar desalination, carbon-based materials considered as a scalable candidate due to the low fabrication cost, abundance, reusability, and excellent photothermal properties. Graphite, graphene, carbonized biomass, carbon black, carbon nanotubes and carbon composites are some of the carbon-based materials that have been tested for efficient solar steam generation.²⁴⁻³⁰ Among them, graphene-based materials such as GO and RGO have been thoroughly researched due to their unique features such as low-cost and scalability in fabrication, broadband absorption, tunable hydrophilicity, functionalizability, low cross-plane thermal conductivity (~ 0.2 W/mK) and flexibility.³¹⁻³⁶ The high performance of graphene-based materials in photothermal energy conversion to generate heat under UV, visible and NIR irradiation particularly for heating water was first demonstrated in our lab in 2010.¹⁶ The mechanism of the photothermal effect of carbon-based materials is still under debate. However,

the suggested mechanism for GO photothermal effect involves absorption of photon energy by GO resulting in the formation of a heated electron gas that rapidly cools down by dissipating the heat to the GO lattice.¹⁶

Carbonized biomass is another potential candidate to be used as a scalable photothermal material. In several studies, considerably high solar-to-vapor efficiencies were obtained by carbonized cellulose-based materials. In recent studies, surface carbonized wood,³⁷ carbonized mushroom,²⁹ carbonized wood embedded in polyethylene foam³⁸ and carbonized wood/carbon nanotube membranes³⁹ demonstrated cost-efficient and scalable properties with promising steam generation efficiencies (80-90%). However, the durability of carbonized materials is not the best compared to other photothermal materials. To address the durability problem, carbonized materials can be incorporated with polymer matrices to obtain reusable and efficient solar steam generation devices.

1.2. Fundamental Principles of Semiconductor Photocatalysis

With the overwhelming boost in the industrialization and increasing population, water pollution by organic contaminants is becoming a huge concern. Over the years, biological and physical treatments have been used to treat the organic contaminants in wastewater. However, these techniques are less effective in removing certain anthropogenic contaminants that are harmful at very low concentrations. Therefore, it is necessary to deploy novel techniques, which are capable of functioning at low concentrations and transforming hazardous materials into non-hazardous or less hazardous components. To be utilized in mass scale, these techniques should be efficient enough to remove pollutants rapidly at low concentrations, inexpensive and also should have a low energy demand.⁴⁰

After the discovery of photocatalysis on a TiO₂ rod in 1972, the utility of semiconductor photocatalysts for the removal of organic pollutants has been widely studied over the years.

Especially, ZnO and TiO₂ can be considered as two of the most widely studied semiconductors used for the photodegradation of different organic contaminants due to their stability, high photosensitivity and large bandgap.⁴¹⁻⁴⁵ In this dissertation, the sixth chapter explains the synthesis of unique shape of ZnO and its utility in photodegrading different organic dyes.

1.2.1. Mechanism of ZnO Photocatalysis

The photodegradation mechanism of ZnO is thoroughly studied. In general, there are four main steps taking place during the heterogeneous photodegradation reaction in ZnO as shown in Figure 1.7.

1. Diffusion of organic pollutants to the surface ZnO
2. Surface adsorption of the organic pollutants
3. Redox reactions in the adsorbed phase
4. Desorption of the products from the surface of ZnO
5. Removal of the products from the interface region

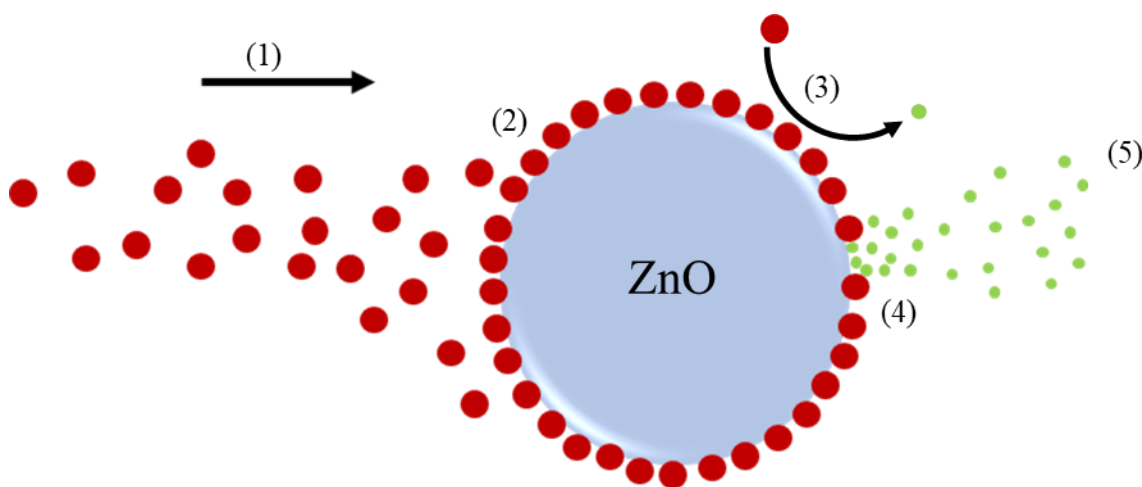


Figure 1.7. General steps involved in heterogeneous photocatalytic oxidation⁴⁶

When ZnO is illuminated with an appropriate light source with photonic energy equal or larger than the band gap, electrons in the valence band are excited into the conduction band resulting in free electrons in the conduction band and positive holes in the valence band. These electron-hole pairs, also called excitons are highly reactive and capable of initiating a chain of reactions that ultimately convert the target organic pollutants into mineralized products. It is proven that most of the toxic pollutants are degraded by this process. However, the extent of mineralization is considered as the most important quality to evaluate the feasibility of the photodegradation because partial oxidation can lead to generating intermediate species that can be more dangerous compared to the parent pollutant.⁴⁷ Figure 1.8 shows the general steps involved in photodegradation mechanism.

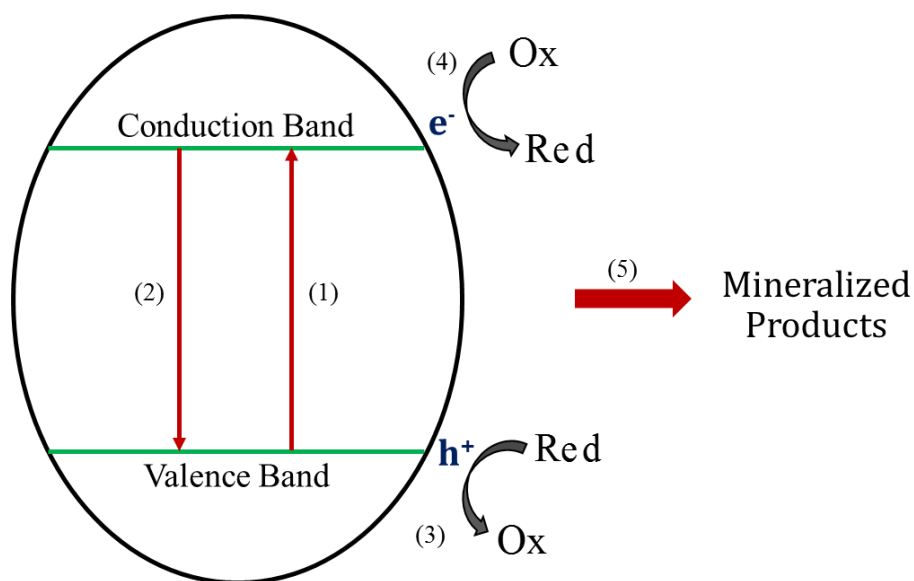
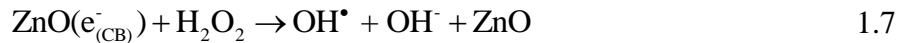
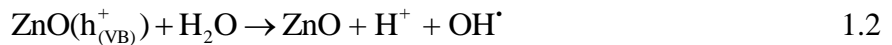
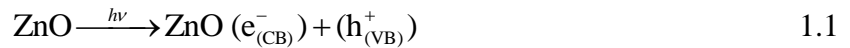
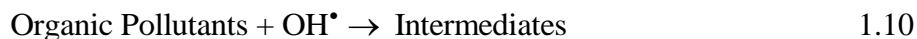
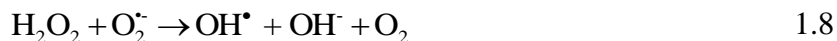


Figure 1.8. General steps involved in a photocatalytic mechanism. (1) excitons are formed upon irradiation, (2) recombination of excitons (radiative or non-radiative decay), (3) An oxidative pathway is initiated by the holes in the valence band, (4) A reduction pathway is initiated by the electrons in the conduction band, (5) Photocatalytic reactions yield mineralized products.

The generated electron-hole pairs can have two fates. They can undergo recombination, releasing energy as photons or heat or can migrate to the surface of the photocatalyst. To be an efficient photocatalyst, it is important to prevent electron-hole recombination. Photodegradation occurs only if the excitons migrate to the surface of the semiconductor and react with surface-bound electron donors and acceptors. This process is called trapping of charge carriers which occurs due to the surface defects and surface-bound scavengers. In semiconductors, the conduction band electrons are highly reactive with chemical potentials ranging from +0.5 to -1.5 V relative to the NHE. Therefore, they can act as strong reducing agents. On the other hand, holes in the valence band possess the oxidative potentials ranging between +1.0 to +3.5 V compared to the NHE making them good oxidizing agents.⁴⁸ These reactive charge carriers trigger a series of redox reactions with surface bounds scavengers such as H₂O and O₂ molecules and generated reactive oxygen species. These reactive oxygen species are the key components of the photodegradation reaction. The key mechanistic steps involved in the photodegradation reaction can be summarized as follows.⁴⁹⁻⁵⁰





The hydroxyl radicals act as a strong oxidizing agent that promote oxidation of the organic pollutants on the surface. To track the photodegradation efficiency, highly conjugated organic dyes are used because of their bright colors. Upon degradation, the change of the color can be easily monitored using UV-visible spectroscopy.

1.3. An Overview of Heavy Metal Removal

Over the years, heavy metal contamination has become an alarming environmental concern. Heavy metals are defined as metals having atomic weights between 63.5 and 200.6 and a specific gravity greater than 5.0.⁵¹⁻⁵² Among many toxic pollutants, heavy metals are considered as the most harmful pollutants to living beings due the adverse effects they can cause at very low concentration and bioaccumulation (long half-life which increases their potential for bioaccumulation and retains in the ecosystems for a long time). Even though the anthropogenic sources are considered as the main source for heavy metals, they can also be introduced to the environment through geogenic sources such as metal ores.⁵³

With the rapid development of industries including metal processing, leather tanning, metal polishing, electroplating, paint manufacturing, metal plating, mining, jewelry, battery manufacturing, oil refining, fertilizers, paper, and pulp and rubber processing, there is a significant increase in the discharge of heavy metal contaminated wastewater into the environment especially

in the developing countries.⁵⁴ Some of the common heavy metals found in industrial wastewater include Cr, Cd, Pb, Co, Cu, Fe, Ni, Zn, As, etc. in different oxidation states.

Currently, several treatment techniques are available to remove heavy metals from the wastewater. More traditional methods include chemical precipitation, ion exchange, filtration, reverse osmosis, electrocoagulation, dialysis/electrodialysis, etc.⁵⁵⁻⁶¹ These techniques have their own advantages and disadvantages. For example, chemical precipitation can be very efficient in removing heavy metals and easier to perform at a minimal cost.⁶² However, it has a huge disadvantage in disposing of resultant sludge creating a secondary pollutant. Ion exchange, reverse osmosis, and membrane filtration are efficient techniques except for the fact that they require expensive and regular maintenance.

Adsorption technique can address some of these limitations due to its attractive features such as simplicity, recyclability, low energy demand, and sludge free operation.^{51, 63-64} Due to the simple operation and low cost, adsorption technique can be a suitable method for wastewater treatment in developing countries. Currently, the most commonly used adsorbent is activated carbon which is relatively costly for large scale applications. Therefore, the search for an inexpensive and efficient adsorbent with a good selectivity is an active field of research. Generally, the adsorption process involves the transferring of heavy metal from the bulk solution to the surface of the adsorbent. The interaction between the pollutant and the adsorbent can be physical (Van der Waals forces) or electrostatic depending on the nature of the adsorbent. In order to understand the nature of the interactions and optimize the adsorption mechanisms, it is important to have a good understanding of the adsorption isotherm models. In general, adsorption isotherms explain the mechanism of retention or mobility of a component from the aqueous solutions to a solid adsorbent at constant

temperature and pH.⁶⁵⁻⁶⁶ Langmuir and Freundlich models are the most widely used isotherm models to study the nature of the interaction between the adsorbent and the pollutant.⁶⁷⁻⁶⁸

Over the years, various types of sorbents have been introduced for the removal of toxic heavy metals such as zeolites,⁶⁹ clay,⁷⁰ chitosan,⁷¹ activated carbon,⁷² modified silica,⁷³ various polymers,⁷⁴ chelating materials, etc. However, now there is a significant interest to utilize nanomaterials as adsorbents due to the attractive features they possess including high specific area, tunable pore sizes, short intraparticle diffusion distance and unique surface properties.⁷⁵ Nanosorbents have shown significantly high adsorption capacities owing to their large specific surface area and high surface energy. Moreover, nanomaterial surfaces can be easily functionalized due to the presence of unsaturated surface atoms. These active surface atoms can easily bind with other atoms giving rise to various composite materials with enhanced features such as magnetic, electric and optical properties.

Regeneration and recycling are considered as two major practical limitations in the adsorption technique since they can limit the large-scale application of the method. Generally, the adsorption process is carried out either by passing contaminated water through the packed adsorbents or dispersing the adsorbent in a pool of wastewater. After the adsorption, the material has to be retrieved and regenerated in order to reuse. If the adsorbent is magnetic, it is easier to separate the material from the treatment plant simply by employing a magnet.⁷⁶⁻⁷⁸ The last chapter of this thesis focuses on the preparation of iron carbide magnetic nanostructures and a composite of iron carbide and aminated graphene oxide for the removal of Cr(VI) from wastewater.

Chapter 02: Characterization Techniques

2.1. X-ray Diffraction

XRD is a highly useful nondestructive technique to obtain information about the crystal structure of a material. According to the arrangement of the atoms, solids can be either amorphous or crystalline. In crystalline materials, the atoms are arranged in an orderly manner whereas in amorphous solids atoms are arranged randomly. XRD technique utilizes the elastic scattering of x-ray photons by atoms in a periodic lattice yielding a fingerprint signal that can be used for identification and to obtain valuable data related to the crystal structure. The principle of XRD is based on the well-known Bragg's law which is given in the equation 2.1.

$$n\lambda = 2d \sin \theta \quad 2.1$$

Where n is an integer called the order of diffraction (often unity), λ is the wavelength of the x-ray source, d is the interplanar distance and θ is the angle between the incident/diffracted beam and the crystal plane. When the x-ray beams satisfy the Bragg's law, the x-ray beams that scattered from the adjacent planes in the crystalline solid will travel distances that differ exactly by one wavelength or multiples of incident wavelength. Those beams that scattered from successive planes will constructively interfere and register an intense beam in the detector which is called a diffracted beam.

In this work, XRD characterizations were done using Panalytical X'Pert Pro diffractometer with Cu K α 1 radiation. All measurements were carried out under ambient conditions. Diffraction patterns were analyzed using X'Pert Highscore Plus software and the database used for identification of crystal structures was the International Centre for Diffraction Data/Joint Committee on Powder Diffraction Standards (ICDD-JCPDS) diffraction pattern library.

2.2. X-ray Photoelectron Spectroscopy

XPS is the most widely used surface analysis technique because of its ability to provide valuable quantitative and chemical state information for a broad range of materials. In a typical XPS measurement, the depth of analysis is about 5-10 nm. Also, it is possible to carry out depth profiling analysis if the XPS instrument is coupled with a sputtering source. The XPS technique is based on the photoelectric effect. When a sample is irradiated with x-ray, photoelectrons are subsequently ejected from the core levels of the atoms near the surface. These photoelectrons are escaped into the vacuum chamber and an electron energy analyzer is used to measure the kinetic energy of the emitted electrons. The energy of a photoelectron depends on the nature of the atomic and molecular environment of the material. Therefore, it provides useful information about the material of interest. The relationship between the incident photon energy and the kinetic energy is given by the modified Einstein equation:

$$KE = h\nu - (BE + \phi + d) \quad 2.2$$

where KE is the kinetic energy of the photoelectron, $h\nu$ is the energy of the x-ray source, BE is the binding energy of the photoelectron, ϕ is the work function of the instrument and d is the positive charge of the sample (if the sample is charging). The value of binding energy and chemical shift (difference from the elemental state) are used for identification of the element and understand its chemical bonding nature in the material.

All the XPS data reported in this dissertation were collected using PHI VersaProbe III Scanning XPS Microprobe. Data analysis was performed using CasaXPS processing software.

2.3. Transmission Electron Microscopy

TEM is a powerful imaging technique that can be used to visualize sample morphology, NP size, and distribution. TEM follows the same basic principles as an optical microscope but in the case of TEM, an electron beam is used instead of light. Due to the low wavelength of the electron beam compared to the visible light, TEM allows visualization of materials with atomic resolution. During the operation, a beam of electrons is sent with high acceleration using an electron gun. This beam is focused into a small, thin, coherent beam by the use of the condenser lenses. Then the electron beam passes through a thin specimen and focused by the objective lens into an image on a phosphor screen or charge coupled device camera.

In this work, TEM images were obtained using Joel JEM-1230 electron microscope operated at 120 kV equipped with Gatan UltraScan 4000SP 4K \times 4K CCD camera. Samples for TEM were prepared by placing a droplet of colloidal suspension in a suitable solvent on a supported film of Formvar carbon-coated, 300-mesh copper grid (Ted Pella) and allowing them to dry under an IR lamp for one hour.

2.4. Scanning Electron Microscopy

The SEM uses a focused beam of high energy electrons which interact with the external surface of the specimen to generate a variety of signals. These signals derived from the interactions between the sample and the electrons, provide useful information about the external morphology, chemical composition and crystalline structure of the specimen. When the electron source produces a beam of electrons by thermionic heating, they are accelerated to a voltage between 1-40 kV and condensed into a narrow beam using condenser lenses. After the beam is focused, scanning coils is employed to deflect the beam in the X and Y axes so it can scan over the surface of the sample. This sample-electron interaction generates different signals. These signals include secondary

electrons, backscattered electrons, diffracted backscattered electrons, x-rays, visible light, and heat. Secondary electrons are used for the imaging, backscattered and diffracted backscattered electrons are used to determine the crystal structure and the characteristic x-rays are used for elemental analysis. In a conventional SEM technique, magnifications ranging from 20 \times to approximately 500,000 \times and spatial resolution of 1 to 20 nm can be achieved depending on the instrument.

In the projects reported in this dissertation, SEM characterization was done using Hitachi SU-70 FE-SEM. Samples were prepared by dispersing a solid sample on the surface of a sticky carbon tape adhered on to an SEM sample holder. Then, the free unadhered samples are removed using clean compressed air flow. Certain non-conductive samples required a conductive coating to increase the conductivity. A thin layer of Pt was coated on materials such as functionalized cotton and carbonized cotton discussed in chapters 4 and 5, for enhanced resolution. A Sputter-coater was used for this purpose.

2.5. Fourier Transform Infrared Spectroscopy

FT-IR is a widely utilized technique to identify certain functional groups in compounds. It detects the vibrational characteristics of functional groups in a sample by shining IR radiation. The energy of IR radiation is not large enough to induce electronic excitations. However, it is large enough to induce bond vibrations such as stretching, contraction, and bending. As a result, when irradiated with IR radiation, certain chemical groups tend to absorb the energy at certain wavelengths. Thereby, a spectrum can be obtained representing absorbance or transmittance as a function of the wavenumber. Typical components of a FT-IR spectrometer include IR source (usually a glowing black- body source that emits radiation through an aperture which controls the amount of energy

delivered to the sample/detector), interferometer (composed of beam splitter, fixed and moving mirror), laser for aligning the mirrors and for internal calibration and a detector.

FT-IR characterizations reported in this dissertation are obtained using a Nicolet-Nexus 670 FT-IR spectrometer with the diamond attenuated total reflection.

2.6. UV-Visible Spectroscopy

UV-Visible spectroscopy is one of the most important characterization techniques that help to understand the optical properties of a material. It provides useful quantitative data obtained from absorption of near-ultraviolet (180–390 nm) or visible (390–780 nm) radiation by chemical species in solution or in the gas phase. The near-ultraviolet and the visible regions of the electromagnetic spectrum provide enough energy that can induce electronic transitions. Due to the superimposition of vibrational and rotational transitions, the UV-vis spectra of analytes in solution do not provide fine a structure. Therefore, this technique is not suitable for identification purposes. However, under controlled conditions, the amount of radiation absorbed by the analyte is directly proportional to the concentration. This relationship is known as Beer's law which is the basis of quantitative application of this technique.

In this work, UV-visible spectra were obtained using an HP-8453 spectrophotometer operating with ChemStation software. Samples were placed in quartz cuvettes with a pathlength of 1 cm. Background spectra were recorded with the respective solvent prior to each measurement.

2.7. Raman Spectroscopy

Raman spectroscopy is a sensitive and non-destructive technique which relies on inelastic scattering or Raman scattering of monochromatic light. Raman spectroscopy provides insight about vibrational, rotational and other low-frequency modes in a material. It is commonly used in

material science to obtain structural fingerprints to identify molecules. Raman spectroscopy is generally considered as complementary to IR spectroscopy. A molecular vibration is only IR active if there is a change in the dipole moment during the vibration. To be Raman active, there should be a change in polarizability or distortion of the electron cloud around the vibrating molecule. Generally, selection rules are used to determine which modes are Raman or IR active.

In a typical Raman experiment, a solid or liquid sample is irradiated with a laser source. Upon interaction with the sample, light scatters and reach the detector which measures the frequency of the scattered light. Majority of the scattered light has the same frequency as the incident light which is known as Raleigh or elastic scattering. A small fraction ($\sim 0.00001\%$) of the scattered light may have higher or lower frequency compared to the incident light. This shift in frequency from the incident laser frequency is due to the different interactions between the incident light and the vibrational energy levels of the molecules in the sample. A Raman spectrum is generated by plotting the intensity of the shifted light versus the energy shift in wavenumbers.

In this work, Raman spectra were recorded using Thermo Scientific DXR Smart Raman Spectrometer with 532 nm excitation laser source. The laser power was 5 mW, the spectral resolution was $\sim 4\text{ cm}^{-1}$ and the spectrum acquisition consisted of 100 accumulations with a total acquisition time of 15 min.

Chapter 03: Plasmonic Graphene Polyurethane Nanocomposites for Efficient Solar Water Desalination

3.1. Introduction

Freshwater scarcity has become one of the most serious global challenges humans are facing now.⁷⁹ Considering the vast availability of saline water on the planet, seawater desalination seems to be the best option to solve this issue. Even though there are a plethora of techniques available for desalination, most of the techniques suffer from high associated energy cost.⁸⁰ Therefore, solar desalination can be the cleanest and most cost-effective way to desalinate seawater. During the last ten years, there has been a great interest in finding materials for solar photothermal energy conversion for their cost savings, clean environment and broad utility in providing water heating and/or steam for many applications including domestic water heating and solar-driven desalination.^{79, 81-84} Moreover, solar photothermal energy conversion is used in industrial applications such as solar crop drying technologies, and basic solar stills to purify water in remote regions. Solar steam generation and solar water desalination are among the most important technologies to address the increasing global water scarcity.^{79, 81-84}

In some of the current photothermal energy conversion systems, copper or aluminum solar absorbers are used due to the low cost. However, they have limited utility because of the inflexibility for tailored applications, reactivity, and limited availability.^{81, 83-84} Due to the vulnerability for surface oxidation, these bulk metals are not very efficient in absorbing the solar spectrum. Moreover, due to the ineffectiveness of solar collectors to convert most of the solar energy into heat and heat loss through bulk water, the current solar thermal desalination devices suffer from low efficiency and low water productivity.⁸¹⁻⁸⁴ To address these issues, extensive research efforts have been dedicated to developing broadband solar absorption materials with

hydrophilic, flexible, porous, and low weight properties that can float on the water surface to provide more efficient and cost-effective solar thermal systems.⁸⁵⁻⁸⁸ Metallic microcavities, metallic gap resonators, and nanostructured gratings have been proposed to take advantage of the efficient photothermal energy conversion associated with SPR absorption.⁸⁹⁻⁹⁵ In some reports, plasmonic metal NPs have been used for efficiently heating ice and liquid water to temperatures above the boiling point of water under nonequilibrium conditions.⁹⁶⁻⁹⁷ Also, aqueous dispersions of gold and carbon NPs were demonstrated to produce water vapor upon solar irradiation without the requirement of heating the bulk liquid.^{17, 98} Several examples of noble-metal and carbon-based nanofluids have also been reported for solar steam generation.⁹⁹⁻¹⁰³

In addition to plasmonic NPs, carbon-based nanomaterials such as single-wall carbon nanotubes, GO and RGO have recently been applied in photothermal energy conversion as they can absorb light over the visible and NIR parts of the electromagnetic spectrum and convert the absorbed energy into heat through nonradiative decay processes.^{86, 104-110} The efficient photothermal effects of graphene-based materials for the conversion of visible, UV and infrared radiation into usable heat particularly for heating bulk water was first demonstrated in 2010.¹⁶ The enhanced photothermal effects by plasmonic metal-graphene nanocomposites consisting of gold, silver or copper NPs and GO nanosheets have also been demonstrated.^{15, 111} Furthermore, it has been shown that the GO interface facilitates the photochemical synthesis and stability of the plasmonic gold NPs which enhances the photothermal energy conversion and results in significant increase in the temperature of water above 105 °C after 60 min illumination with direct sunlight without any focusing lenses or mirrors.¹⁴ These results indicate that the plasmonic-graphene nanocomposites have excellent photothermal properties which make them the best candidates to be used in solar heating or photothermal water distillation systems.

Even though plasmonic-graphene nanocomposites are proven materials with excellent photothermal properties for heating up bulk water for a variety of applications, they are not effective in the water evaporation and steam generation required for solar water desalination. It is mainly because of the heat loss to bulk water due to the large heat capacity of water. If the photothermal materials are immersed in bulk water, it is practically impossible to generate steam due to the heat dissipation to bulk water. Therefore, photothermal materials must be floating on the water surface while a supporting material on which the solar absorbers are anchored, must transport water on to the irradiation surface so the converted heat can efficiently convert that small layer of water into steam. To achieve this goal, herein, we report on the development of a new generation of highly efficient, flexible, low weight and cost-effective Plasmonic Graphene Polyurethane nanocomposite foams for efficient Solar Water Desalination.¹¹² The PGPU nanocomposites contain plasmonic NPs that absorb sunlight much more efficiently than bulk metals or pure carbon materials.^{17, 97-98} The PGPU materials are produced as porous foams that float on top of the evaporating water pools.^{87, 95, 104-105} Therefore, these materials significantly enhance the absorption of solar energy and the high conversion efficiency of sunlight into heat. Furthermore, the materials can be directly applied to the existing solar thermal water heating and desalination devices and plants without any changes or modifications required in the design and construction. These materials also offer advantages over the less durable pure polymeric materials which have the limitations in thermal stability and the challenges of the long-term stability and weathering during operation. This chapter is adapted from the article published in the journal of ACS Applied Energy Materials.¹¹²

3.2. Materials and Methods

3.2.1. Materials

Graphite flakes (99.9999%), potassium permanganate (99.0%), sulfuric acid (98.0%), hydrogen peroxide (35.0%), sodium nitrate (99.0%), polypropylene glycol ($M_n = 400$), 2,4-tolylene diisocyanate (TDI, 95.0%), triethylamine (> 99.5%), stannous octoate (95%), methylene chloride, gold(III) chloride solution (99.99%), silver nitrate (99.0%), magnesium sulfate (99.99%), calcium chloride (99.9%), sodium chloride (> 99.0%). All reagents were purchased from Sigma-Aldrich and used without further purification. DI water was used in all the experiments.

3.2.2. Material Preparation

3.2.2.1. Synthesis of Flexible Polyurethane Foam

To prepare PUFs, 12.5 g of polypropylene glycol, 0.8 mL of DI water, 1.9 mL of methylene chloride, 50 μ L of triethylamine, and 110 μ L of stannous octoate were mixed under gentle stirring then poured into a plastic cup containing 9.1 g of TDI and the mixture was stirred vigorously for about 10 seconds and then left undisturbed for 1 hr to let the foam to grow and dry.

3.2.2.2. Synthesis of 0.5 wt% GO-Polyurethane Composite Foam

GO prepared via the improved Hummer method.¹¹³ 109.0 mg of GO was suspended in 1.1 mL of DI water and sonicated well for 30 min. Then, 12.5 g of polypropylene glycol, 1.9 mL of methylene chloride, 60 μ L triethylamine, and 120 μ L stannous octoate were added into the GO suspension, mixed well for 5 min and poured into the plastic cup containing 9.3 g of TDI. After 1 hour, the GO-PU composite foam was removed from the plastic cup and kept at room temperature overnight to dry.

3.2.2.3. Synthesis of PGPU Nanocomposite Foams

To synthesize 0.2 wt% Au-GO-PU or 0.2 wt% Ag-GO-PU composites, a cylindrical shape (6 cm diameter, 1.5 cm height) piece of the GO-PU composite foam block was cut out and contained in a 50 mL solution containing HAuCl_4 or AgNO_3 for 8 hr. The gold or silver ions were reduced using the free amino and amide groups on the surface of PUF under microwave irradiation using a 700 W microwave oven for 50 s (in 10 s intervals). Afterward, the samples were washed several times with cold water then dried overnight at room temperature.

3.2.2.4. Synthesis of the 0.1 wt% Ag-0.1 wt% Au-GO-PU Nanocomposite Foam

First, a cylindrical shape (6 cm diameter, 1.5 cm height) piece of the GO-PU foam was immersed in 50 mL of the 0.1 wt% HAuCl_4 in water for 8 hr, then the sample was washed with DI water to remove the non-adsorbed gold ions. The sample was then immersed in 50 mL of the 0.1 wt% silver nitrate in water for 8 hr. Then the gold and silver ions adsorbed within the GO-PU foam were reduced under MWI for 50 s (in 10 s intervals). Finally, the resulting Ag/Au PGPU nanocomposite foam was washed several times with cold DI water and dried overnight at room temperature.

3.2.3. Characterization of Materials

The PGPU nanocomposite foams were characterized by the FT-IR spectroscopy using the Nicolet-Nexus 670 FT-IR spectrometer (4 cm^{-1} resolution and 32 scans), diamond attenuated total reflectance. X-ray diffraction patterns were recorded with a scanning speed of 2° in $2\theta/\text{min}$ using an X'Pert Philips Materials Research diffractometer. The morphology of the foams and the nanoparticle size distribution were determined by SEM (Hitachi SU-70 FE-SEM) and TEM (Joel JEM-1230) microscopes, respectively. The optical reflectance, transmission, and absorbance of plasmonic NPs were measured using a superior micro spectrophotometer (Olis 14 CD), with reflectance power supply (CRAIC Technology, 75 W Xenon). The natural sunlight was generated

by Sol2A, Newport sun simulator. The concentration of metal ions in solution before and after desalination was determined by ICP-OES.

3.2.4. Solar Steam Generation Experiments

The experimental set up is shown in Figure 3.1. The solar steam generation rates of eight solar absorber foam samples: PU, Au-PU, Ag-PU, Ag/Au-PU, GO-PU, Au-GO-PU, Ag-GO-PU, and Ag/Au-GO-PU were measured and compared with pure DI water under three solar irradiation intensities of 1 kW/m², 5 kW/m² and 8 kW/m² over 30 min. The different solar intensities were obtained using a focusing lens (208.2-mm focal length and 279.4-mm diameter). The foam sample

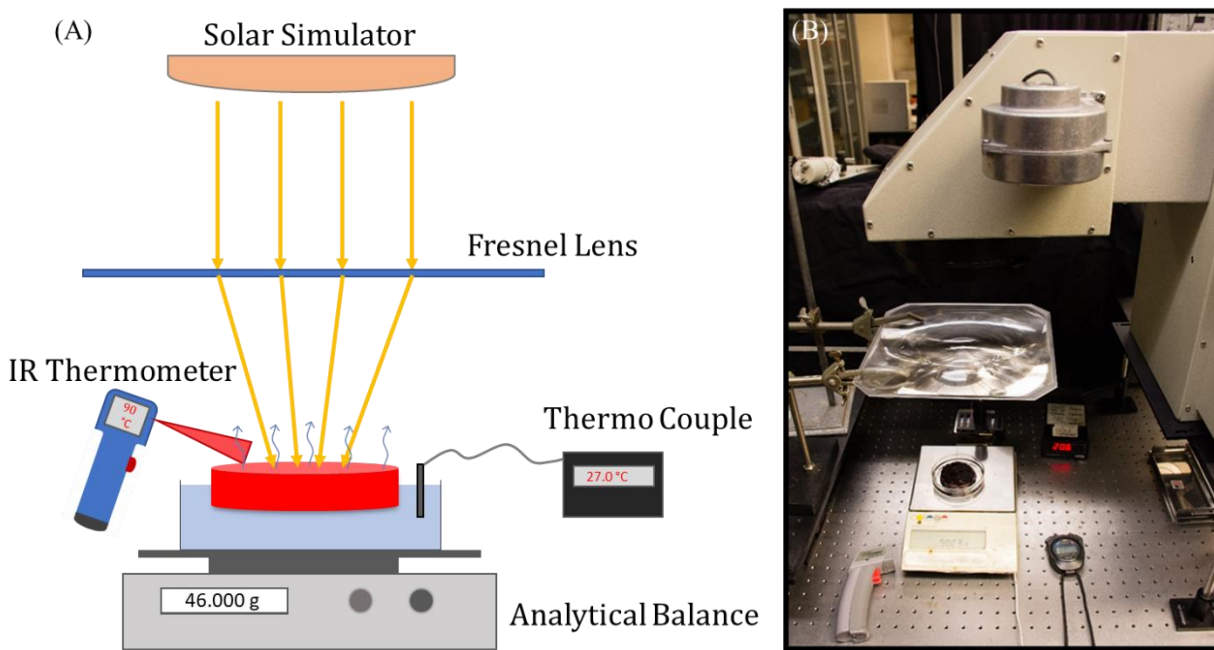


Figure 3.1. The experimental set up of the solar steam generation measurement unit. (A) Schematic representation of the steam generation setup during the experiment. (B) An actual image of the solar simulator when it is switched off.

with a diameter of 6 cm and a thickness of 1.5 cm was floated on top of the water surface in a 50 mL Petri dish with 7 cm inner diameter placed on a calibrated electronic balance. All the samples were immersed in DI water to be wetted before floated on the water surface. The temperatures of

the irradiation surface and bulk water (water below the sample) were recorded using an IR heat sensor and a thermocouple, respectively. Once the samples are irradiated, generated steam escaped the sample of which the amount can be estimated using the weight change displayed in the analytical balance. The steam generation rates were then reported as the change in the recorded mass of water normalized by irradiation area and time. The weight changes were recorded every five minutes and then used to calculate the evaporation rate and efficiencies of the solar steam generation. All the experiments were carried out at room temperature of 20 ± 1 °C and humidity of ~40%.

3.2.5. Solar Water Desalination Tests

To determine the utility of the Ag/Au-GO-PUF composite in SWD, artificial seawater sample containing 1500 ppm Mg^{2+} , 1250 ppm Ca^{2+} , and 1000 ppm Na^+ was employed. Then, the steam generation test was conducted for the prepared artificial seawater sample using Ag/Au-GO-PUF device under fixed solar illumination (5 sun) was investigated. The generated steam was condensed instantly on the quartz cover of the evaporation chamber when Ag/Au-GO-PU composite is used, while without this plasmonic sample the amount of generated water is minimal. The condensed water can be easily collected using a pipette, after which ICP-OES measurements were carefully performed to check the concentrations of the primary ions (Na^+ , Mg^{2+} , and Ca^{2+}) naturally existed in the seawater.

3.2.6. Solar Steam Generation Recycling Experiments

Ten solar steam generation cycles were carried out to evaluate the sustainability and stability of Ag/Au-GO-PU nanocomposite foam. For each cycle, the foam sample was illuminated under solar light supplied by the solar simulator (Sol2A, Newport) with a light density of 5 kWm^{-2} . After 30

min, the weight changes of water and the temperature of the steam were determined. After each cycle, the wetted Ag/Au-GO-PU foam was dried and cooled down and used for the next cycle.

3.3. Results and Discussion

The synthetic strategy utilized for the design of the PGPU nanocomposite foams is described in Figure 3.2. The design strategy involves covalent attachment of the GO sheets to the PUF matrix via a reaction between isocyanate groups of the TDI molecules and phenol hydroxyl groups in the basal planes of the GO nanosheets. These covalent attachments increase the inter-planar distance between the GO nanosheets which prevent the stacking and aggregation of the GO nanosheets. The TDI molecules can also react with the carboxylic functional groups at the edges of the GO nanosheets to form connections between GO nanosheets and PUF matrix. The TDI molecules attached to the edges of GO react with polypropylene glycol in the presence of triethylamine and stannous octoate catalysts to undergo in situ polymerization to form the arms of the PU chains extended from the edges of the GO nanosheets. The crosslinked PU arms provide a highly porous matrix in which the GO nanosheets are well dispersed. The resulting composite is dark ash in color in contrast to the white color of the pure PUF. GO-PU has the advantages of enhanced photothermal energy conversion due to the strong light absorption by GO in the visible and NIR regions and the enhanced evaporation rates of water due to the highly porous network provided by the PU matrix. The photothermal energy conversion can further be enhanced by the dispersion of the plasmonic metal NPs within the GO-PU composite. To accomplish this goal, gold or silver ions are anchored to the surface of the GO-PU composite immersed in water through strong electrostatic adsorption at the amino and amide groups of the GO-PU composite which are considered to be strong chelating ligands due to the presence of lone pairs of electrons that can coordinate with the metal ions. The next step involves the rapid reduction of the metal ions on the

surface of the GO-PU composite by the amino and amide groups under fast microwave heating (50 s). The rapid reduction of the adsorbed metal ions is expected to lead to pulse nucleation under limited growth conditions due to the low concentration of the metal ions thus resulting in the formation of well-dispersed plasmonic NPs within the PGPU nanocomposite foam.¹¹⁴

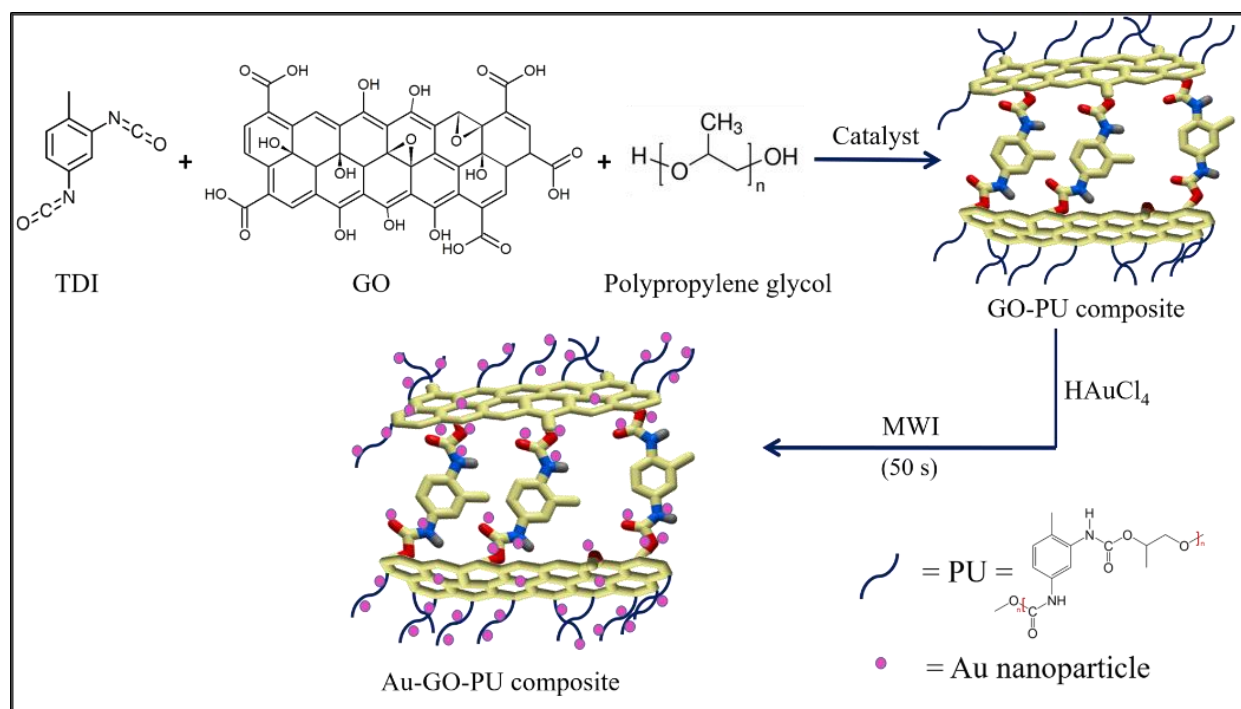


Figure 3.2. Design strategy and general steps involved in the synthesis of the PGPU nanocomposite foam.

Figure 3.3A displays the XRD diffraction patterns of GO and the TDI-GO composite. The sharp diffraction peak of GO at $2\theta = 10.8^\circ$ indicates an interlayer spacing of 8.2 \AA resulting from the presence of the oxygen functional groups on the surface of the GO sheets as compared to the 3.4 \AA spacing between the graphene sheets in graphite.^{16, 114} However, the XRD pattern of the TDI-GO composite shows a downshift of the GO peak to $2\theta = 5.6^\circ$ indicating a significant increase in the interlayer spacing to 15.6 \AA due to the covalent attachments of the TDI molecules between GO layers in the TDI-PU composite.¹¹⁵ Therefore, it is fair to conclude that the TDI molecules are

covalently linking the basal planes of the GO nanosheets in the TDI-PU composite. This is further supported by comparing the FTIR spectra of GO and TDI-GO displayed in Figure 3.3B. The FTIR spectrum of GO shows various types of oxygen-containing functional groups such as the broad peak at 3335 cm^{-1} due to O-H stretching vibration of hydroxyl groups and the peak at 1733 cm^{-1} for the C=O moiety of the COOH groups.¹¹⁶ The bands at 1156 cm^{-1} and 1080 cm^{-1} are ascribed to epoxy and alkoxy stretching, respectively.¹¹⁶ The TDI modified GO composite displays a new stretching peak at around 1655 cm^{-1} assigned to the carbonyl group of amide or carbamate/urethane stretching.⁴⁰ In addition, the intensity of O-H stretching in GO is either reduced or disappeared and instead, a new intense band at around 3288 cm^{-1} corresponds to the N-H stretching vibrations appears. Furthermore, the TDI-GO spectrum shows a characteristic band at 2271 cm^{-1} ascribed to the isocyanate-terminated GO-PU polymer composite thus confirming the formation of the PU arms attached to the edges of GO in the GO-PU composite.¹⁰⁸

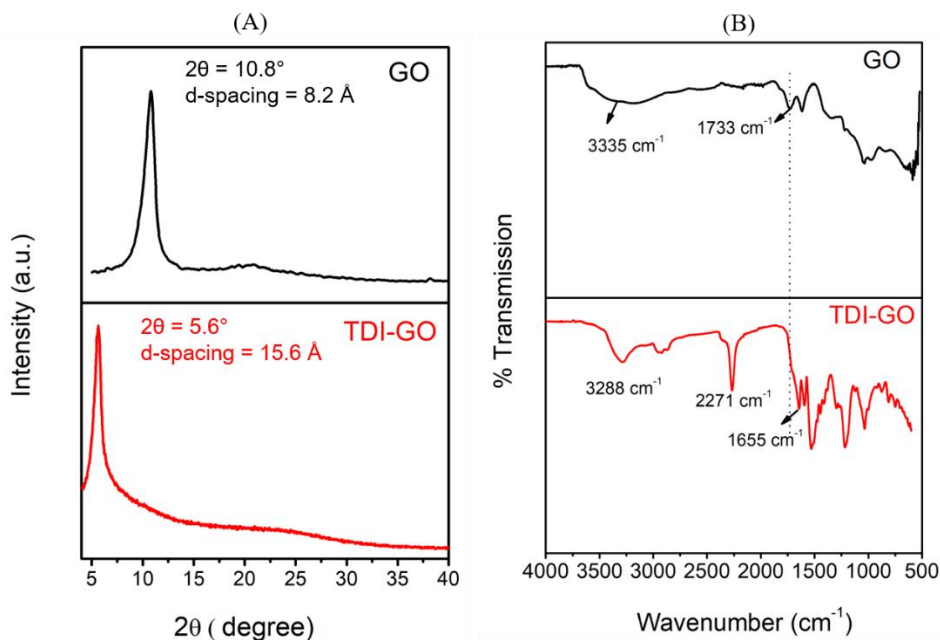


Figure 3.3. (A) XRD patterns and (B) FTIR spectra of GO and TDI-GO nanosheets.

Therefore, the results shown in Figure 3.3A and B confirm the successful chemical reaction between the hydroxyl functional groups on the top and bottom surfaces of GO and the carboxyl functional groups at the edges of GO with TDI molecules which lead to the formation of a urethane/carbamate ester or amide bonds in the GO-PU composite.

The XRD patterns of the Au-GO-PU, Ag-GO-PU and Ag/Au-GO-PU composites clearly confirm the incorporation of the plasmonic NPs within the GO-PU composites as shown in Figure 3.4A. The XRD peaks at $2\theta = 38.1^\circ$, 44.3° , 64.5° and 77.4° displayed in Figure 3.4A are assigned to the characteristic (111), (200), (220) and (311) reflections from the face centered cubic (fcc) crystals of gold (JCPDS76-1802) and silver (JCPDS 4-0783).^{15, 111, 117} The well-defined intense peaks in the diffraction pattern confirm the excellent crystallinity of the gold and silver NPs incorporated within the GO-PU composites. Figure 3.4B displays the UV-Vis absorption spectra of the Au-GO-PU, Ag-GO-PU and Ag/Au-GO-PU composites. The spectra of the Au-GO-PU and Ag-GO-PU composites show broad bands with maxima at 533 nm and 414 nm correspond to the SPR absorption of Au and Ag NPs, respectively.^{15, 111} The spectrum of the Ag/Au-GO-PU composite exhibits a very broad extended absorption between 402–650 nm that indicates the presence of both gold and silver NPs on the surface of the GO-PU composite.

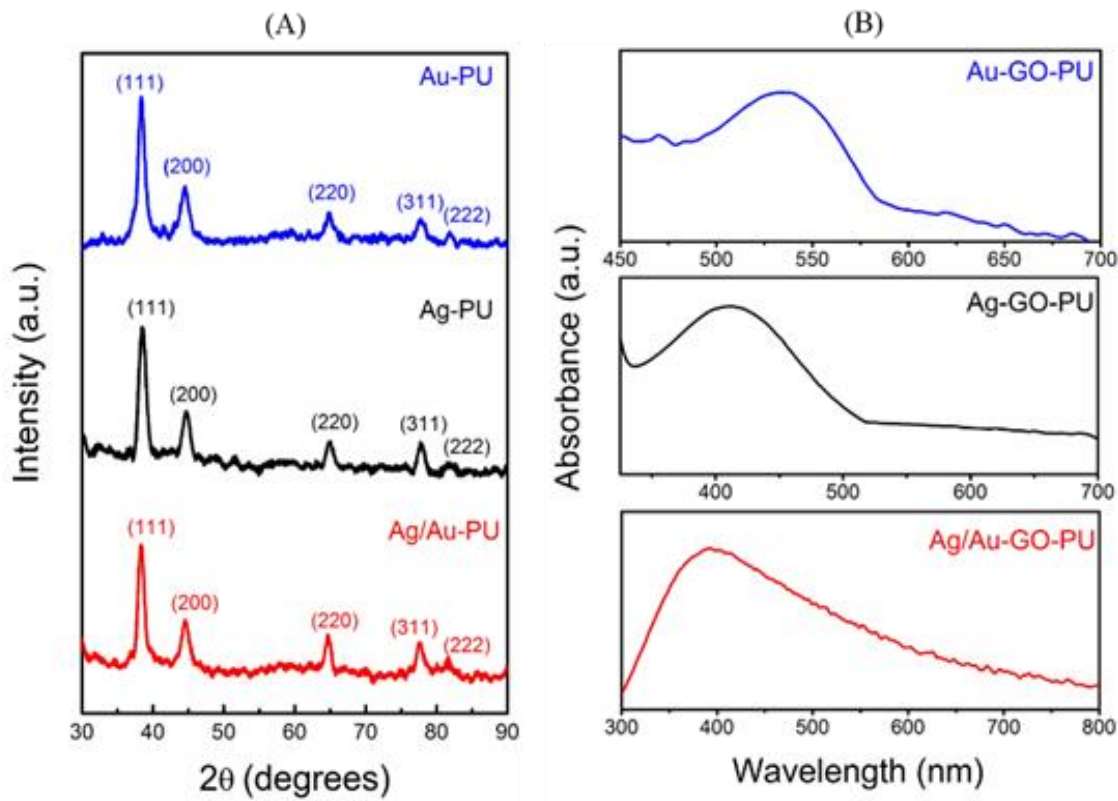


Figure 3.4. (A) XRD patterns and (B) UV-Vis absorption spectra of Au-GO-PU, Ag-GO-PU and Ag/Au-GO-PU composites.

The high porosities of the PU matrix and the GO-PU composite are clearly evident in the SEM images displayed in Figure 3.5. It is important to note that the highly porous structure of PU is retained after the covalent attachment of GO to the PU foam. The attachment of the GO nanosheets to the PU foam is clearly evident in the SEM images of the GO-PU composite shown in Figure 3.5. The open porous morphology and the hydrophilic nature of the PU matrix are critical in providing a continuous water supply for efficient solar evaporation from the porous surface with minimum heat loss to bulk water.¹⁰⁸

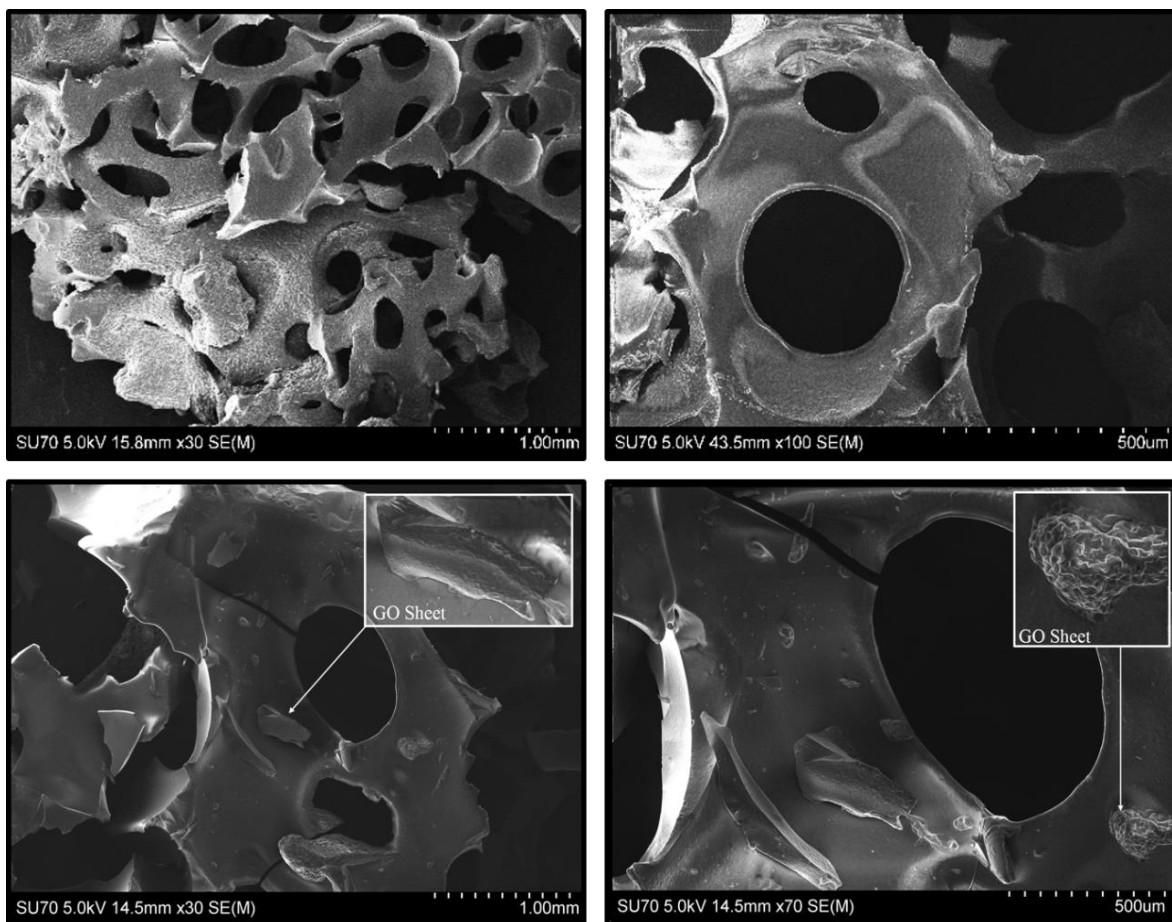


Figure 3.5. SEM images of the Au-PU foam (top) and Au-GO-PU (bottom).

Figure 3.6 displays TEM images of the Au-PU nanocomposite confirming the dispersion and uniform distribution of the Au NPs on the porous surface of the PU foam. The Au NPs exhibit a relatively narrow size distribution ranging from 3 to 10 nm with no evidence for agglomeration or significantly larger particles. In addition, it can be seen from the low magnification TEM image in Figure 3.6 that the open porous morphology of the PU matrix is not affected by the incorporation of the Au NPs within the PU foam.

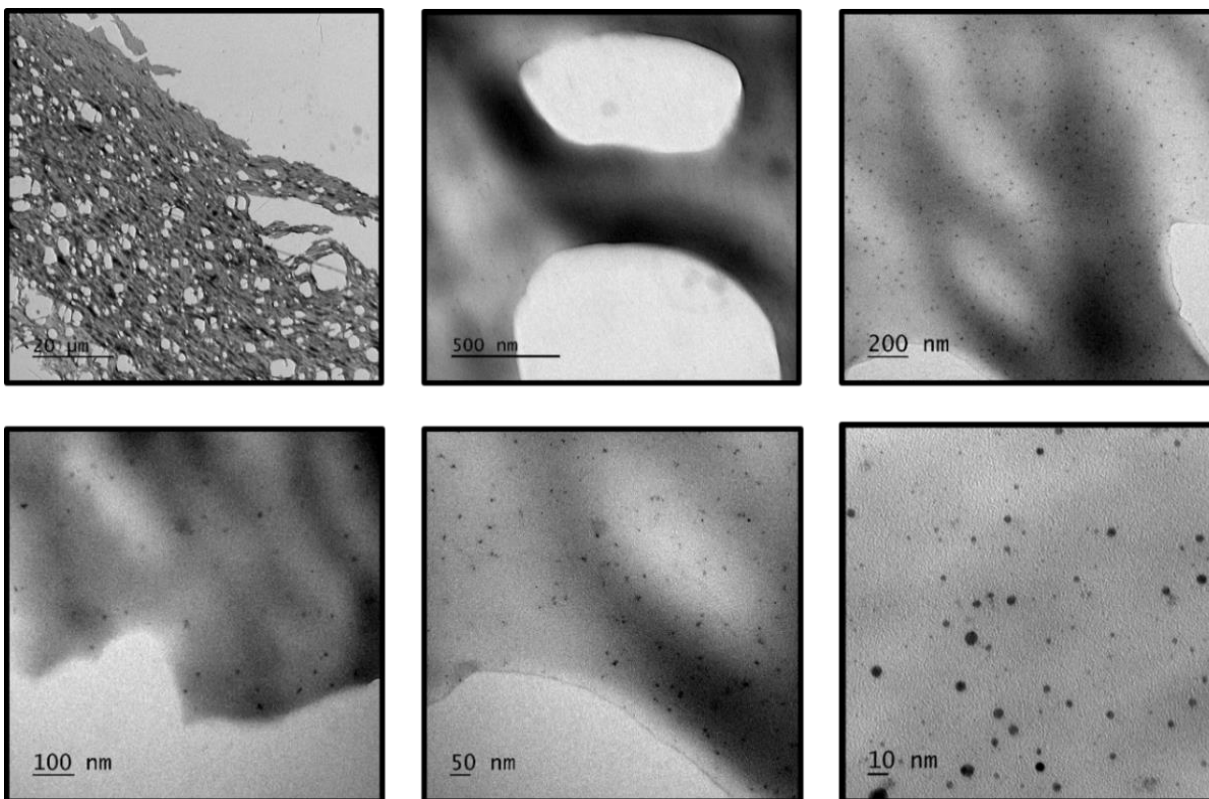


Figure 3.6. TEM images of the Au-PU nanocomposite.

To evaluate the solar steam generation efficiency for different PGPU solar thermal converters, eight circular foam composites each with a diameter of 6 cm and a thickness of 1.5 cm were prepared with the compositions of: (1) pure polyurethane (PU), (2) 0.2 wt% Ag in PU (Ag-PU), (3) 0.2 wt% Au in PU (Au-PU), (4) 0.1 wt% Ag and 0.1 wt% Au in PU (Ag/Au-PU), (5) 0.5 wt% GO in PU (GO-PU), (6) 0.2 wt% Ag, 0.5 wt% GO in PU (Ag-GO-PU), (7) 0.2 wt% Au, 0.5 wt% GO in PU (Au-GO-PU), and (8) 0.1 wt% Ag, 0.1 wt% Au, 0.5 wt% GO in PU (Ag/Au-GO-PU). The solar absorber samples display different colors according to their compositions as shown in optical images displayed in Figure 3.7. All the samples were tested for steam generation and compared with pure DI water in the absence of any solar absorber under three different solar illuminations of 1, 5 and 8 kW/m² over 30 min using the 450 W, Newport Sol2A, Class ABA solar

simulator. Each sample was floated on top of the water surface in a 50 mL Petri dish with 7 cm inner diameter and was placed on a calibrated electronic balance. Water was transported from the bulk water to the sample surface by capillary action. The temperature of the steam (evaporation layers) and bulk water (water around the sample) was recorded by an IR thermometer and a thermocouple placed below the foam sample in water, respectively. The evaporation rate was calculated as the change in the recorded mass of water normalized by the area of the irradiated sample and the corresponding time interval. The weight changes were recorded at the corresponding time interval (5 min) and then used to calculate the evaporation rate and efficiencies of solar vapor generation. All the experiments were carried out at room temperature, 20 ± 1 °C and humidity of ~40%. The experimental set up is shown in Figure 3.1.

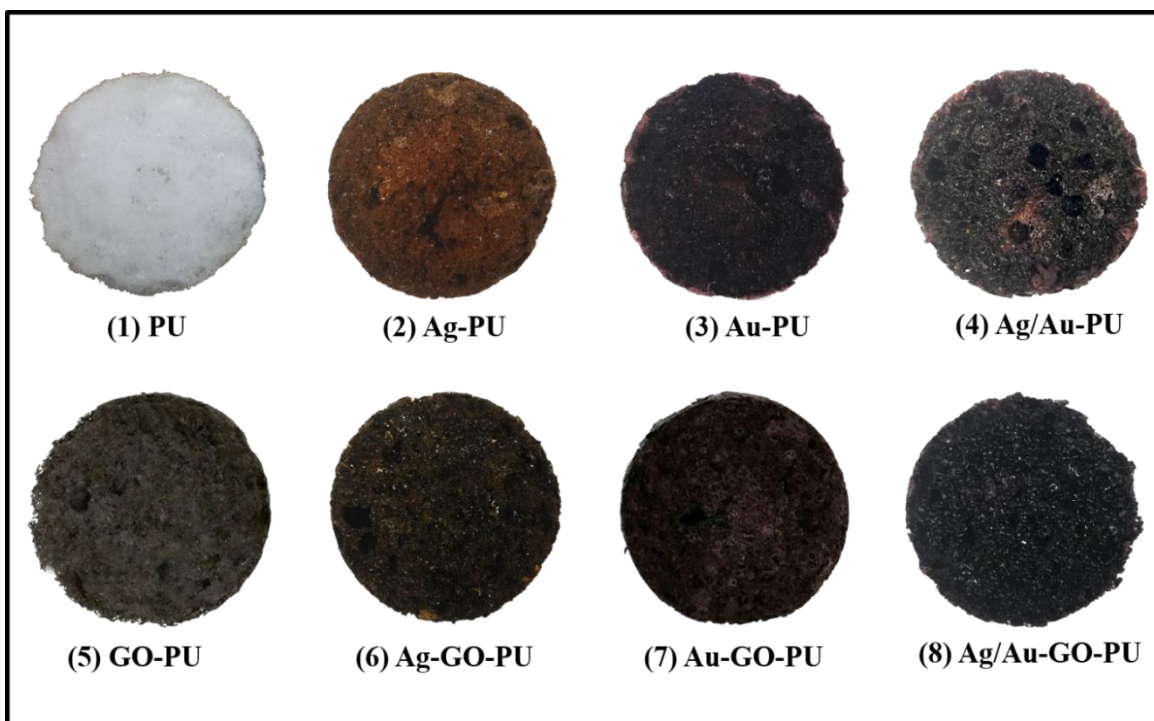


Figure 3.7. Optical images of the solar absorber foams: (1) PU (polyurethane), (2) Ag-PU (0.2 wt% Ag in PU), (3) Au-PU (0.2 wt% Au in PU), (4) Ag/Au-PU (0.1 wt% Ag and 0.1 wt% Au in PU), (5) GO-PU (0.5 wt% GO in PU), (6) Ag-GO-PU (0.2 wt% Ag, 0.5 wt% GO in PU), (7) Au-GO-PU (0.2 wt% Au, 0.5 wt% GO in PU), and (8) Ag/Au-GO-PU (0.1 wt% Ag, 0.1 wt% Au, 0.5 wt% GO in PU). Each sample is 6 cm in diameter and 1.5 cm in thickness.

Figure 3.8 displays photographs showing steam generation from the water surface using the GO-PU, Au-PU, Ag-AU and the Ag/Au-PU solar absorbers. The porous and cellular structure of the polyurethane foam (Figure 3.5) not only makes the material float on water (Figure 3.8) but also enhances the light absorption by the gold and silver NPs dispersed on the surface of the PU foam. Additionally, the cellular structure of the foam enables rapid replenishment of surface water after evaporation through a capillary effect. Moreover, the hydroxyl and carboxylic functional groups of GO enhance the hydrophilicity of the pore structure of the PU foam. At higher solar illumination, the water evaporation rate is high and therefore, it is vital to replenish the surface water layer on the PGPU composite by channeling water through the pores of the PU matrix by

capillary action. When the pore structure of PU is reinforced by the hydrophilic GO nanosheets, the capillary action becomes more efficient in replenishing the evaporating water. Since GO, according to our design and synthesis strategy, is covalently bonded to the PU matrix, leaching of GO is avoided thus allowing the material to be recycled without losing the strong solar absorber GO as it will be demonstrated below.

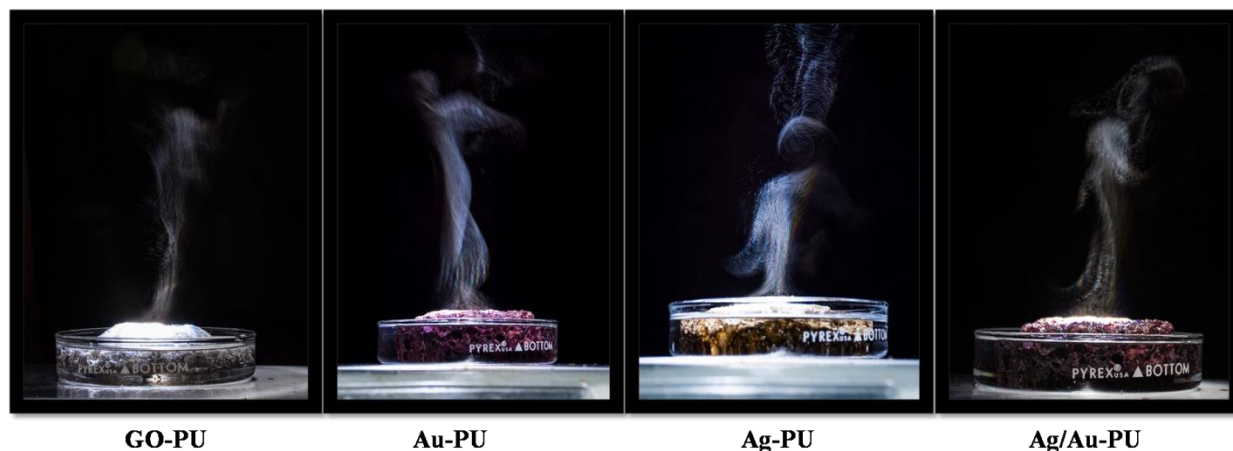


Figure 3.8. Steam generation from water surface using different solar absorbers and photothermal converters under one sun illumination.

The results from the solar steam generation experiments of the eight photothermal converter foams are presented in Figure 3.9. Figure 3.9A-C display the normalized steam generation rates at solar illumination of 1 kW m^{-2} (1 sun), 5 kW m^{-2} (5 sun) and 8 kW m^{-2} (8 sun), respectively. At all solar illumination intensities, the pure PU foam exhibits the lowest evaporation rate ($0.48 \text{ kg m}^{-2} \text{ h}^{-1}$ at 1 sun) among the eight foam samples. This is due to the lack of solar absorption by the PU foam and therefore, the small enhancement effect in the evaporation rate over pure water (1.4 times at 1 sun) is attributed to surface evaporation through the porous structure of the PU foam which results in minimizing the heat loss by bulk water. Both the incorporation of the plasmonic NPs within the PU foam and the covalent attachment of GO to the PU show significant enhancements of the

evaporation rates due to the broad light absorption band by the plasmonic NPs and GO. The incorporation of the plasmonic NPs within the PU foam appears to be more effective in enhancing the water evaporation rates compared to GO-PU at low illumination intensity such as 1 sun. However, at 8 sun, the plasmonic PU foam shows a decrease in performance as compared to the GO-PU foam. For example, at 1 sun, the steam generation rates were in the order: Ag/Au-GO-PU > Au-GO-PU > Ag-GO-PU > Ag/Au-PU > Au-PU > Ag-PU > GO-PU > PU > DI H₂O. However, at 8 sun, the steam generation rates were in the order: Ag/Au-GO-PU > Ag-GO-PU > Au-GO-PU > GO-PU > Ag/Au-PU > Au-PU > Ag-PU > PU > pure H₂O (blank). Steam generation rates for all the PGPU samples and blank samples (pure PUF and DI water) are mentioned in Table 3.1. At 5 sun, the trend is almost similar to the trend at 8 sun except for the steam generation rate of Ag/Au-PU is slightly higher than the Ag/Au-GO-PU sample. PUF is a thermoplastic polymer and also can illumination, the localization of the plasmonic heat at the evaporation surface by the PU foam may not be very effective and this could explain the decrease in the steam generation performance of act as an insulator which can help to localize the plasmonic heat at the evaporation surface for effective steam generation and decrease the heat loss to bulk water.³⁰ However, at high solar the plasmonic PU foam compared to the GO-PU foam at high illumination intensities. Another explanation could be the possibility of agglomeration of the plasmonic NPs in the PU foam at high solar illumination which could result in decreasing the photothermal effect of the plasmonic PU foam. It is interesting that this effect is not observed in the plasmonic-GO-PU foams which exhibit the highest evaporation rates among the eight photothermal converters at both low and high illumination intensities. This result is consistent with the recent finding that the GO interface enhances the photochemical stability of the plasmonic gold NPs.¹¹⁴ It appears that the high localization of the plasmonic heat at the evaporation surface by the GO-PU composite plays the

major role in achieving the superior performance of the PGPU foams in solar water desalination.

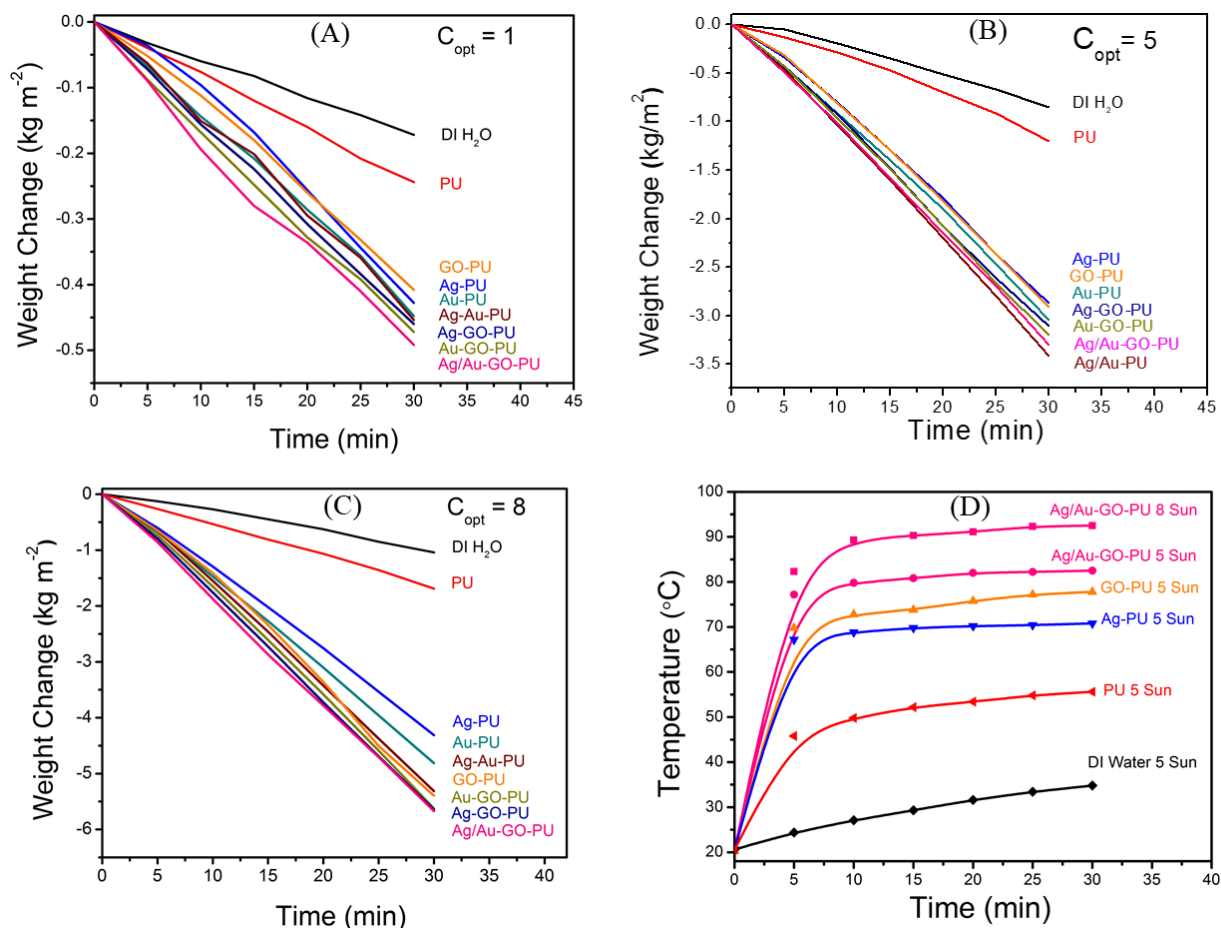


Figure 3.9. Solar evaporation of different foam samples using solar simulator with light densities of (A) 1 kW m^{-2} (optical concentration $C_{opt} = 1$), and (B) 5 kW m^{-2} (optical concentration $C_{opt} = 5$). (C) 8 kW m^{-2} (optical concentration $C_{opt} = 8$) (D) Temperature change at the surface of different foam absorbers and DI water after solar illumination for 30 min under optical concentrations of $C_{opt} = 5$ and 8.

Table 3.1. Steam generation rates of DI water, pure PUF and all the PGPU samples at different solar intensities.

Sample	Steam Generation Rate (kg m ⁻² h ⁻¹)		
	1 Sun (1 kW m ⁻²)	5 Sun (5 kW m ⁻²)	8 Sun (8 kW m ⁻²)
DI Water	0.34	1.70	2.08
PUF	0.48	2.40	3.36
Ag-PU	0.86	5.74	8.62
Au-PU	0.90	6.08	9.62
Ag/Au-PU	0.91	6.82	10.62
GO-PU	0.82	5.83	10.78
Ag-GO-PU	0.92	6.21	11.30
Au-GO-PU	0.94	6.41	11.26
Ag/Au-GO-PU	1.00	6.60	11.34

Figure 3.9D displays a comparison of the temperature change at the surface of different solar absorbers relative to pure water after solar illumination for 30 min under optical concentrations of 5 and 8 sun. The PGPU foams exhibit the highest temperature increase at any solar illumination. For example, at 5 sun, the surface temperature of the Ag/Au-GO-PU foam can increase from 20.0 °C to 82.5 °C in 30 minutes, while the blank water can only reach 34.8 °C. This is also reflected in the high rates of water evaporation by the Ag/Au-GO-PU foam which are 2.8, 4.0, and 5.4 times higher than pure water evaporation at 1, 5 and 8 sun, respectively.^{17, 118} Figure 3.10A compares the solar-to-vapor efficiencies of the PGPU foams at three solar intensities (1, 5 and 8 sun). The thermal efficiency η_{TH} is defined as,

$$\eta_{\text{TH}} = \frac{\dot{m}h_{\text{LV}}}{C_{\text{opt}}q_i} \quad 3.1$$

where \dot{m} represents the mass flux in $\text{g m}^{-2} \text{s}^{-1}$, h_{LV} is the total enthalpy for the liquid to vapor phase change of water in J. C_{opt} is the optical concentration (number of suns) and q_i the nominal direct solar intensity (generally considered as $1 \text{ sun} = 1 \text{ kW m}^{-2}$).^{92, 99, 104, 110} The results reveal that the Ag/Au-GO-PU foam has calculated thermal efficiencies for solar-enabled steam generation under 1, 5 and 8 sun of 63.0, 87.7 and 96.3 %, respectively. The calculated efficiency at 8 sun is considered one of the highest values reported for photothermal energy conversion materials used for solar water desalination as demonstrated by the date displayed in Figure 3.10B.^{37, 93, 99-100, 108-110, 118-120}

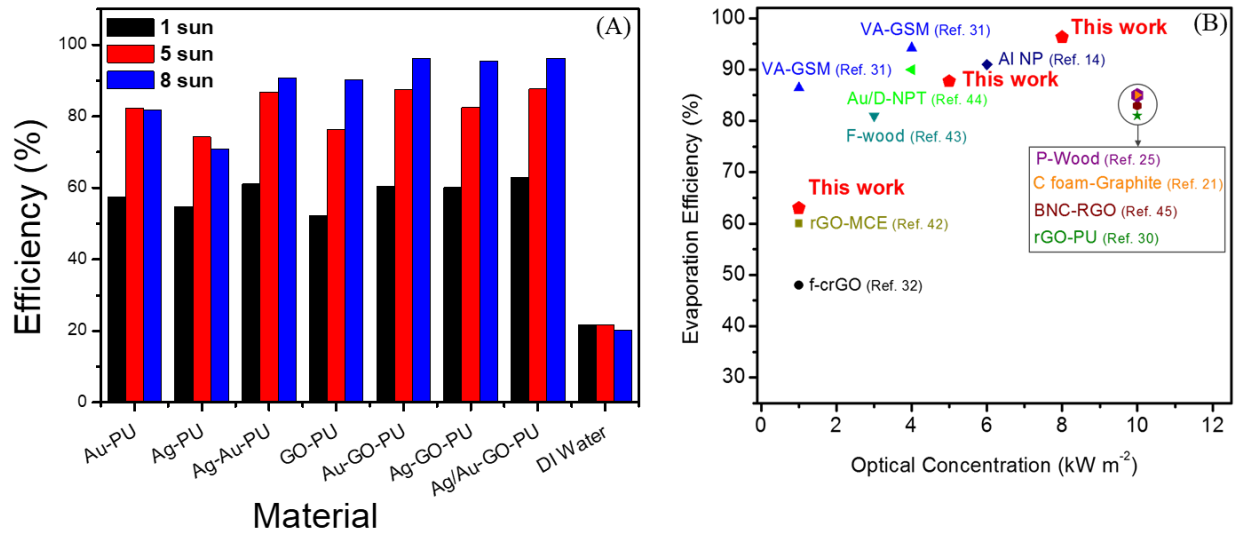


Figure 3.10. Solar-to-vapor efficiency of (A) different PGPU samples at solar intensities of 1, 5 and 8 sun and (B) of the Ag/Au-GO-PU foam in comparison with other reported photothermal conversion materials.

To further evaluate the utility of the PGPU foam in solar SWD, the concentrations of the three primary ions Na^+ , Ca^{2+} and Mg^{2+} naturally present in seawater were determined in the condensed water obtained from the desalination system using ICP-OES. Figure 3.11A shows that the

concentrations of the representative ions are significantly reduced after the solar water desalination using the Ag/Au-GO-PU foam. After the desalination test, the concentrations of the Na^+ , Ca^{2+} and Mg^{2+} ions decreased significantly from the original values of 1000, 1250 and 1500 mg/L to 0.04, 0.04 and 0.001 mg/L, respectively. The ion concentration values after the desalination test by the PGPU foam are well below the standard values reported by the US Environmental Protection Agency and the World Health Organization, and also below the values obtained by common SWD techniques such as membrane (10–500 ppm) and distillation (1–50 ppm).^{86, 118} Additionally, the solar water desalination experiments indicate that $11.34 \text{ kg m}^{-2} \text{ h}^{-1}$ of clean water can be obtained from the PGPU desalination system using Ag/Au-GO-PU foam under 8 sun illumination.

To evaluate the reusability and stability of Ag/Au-GO-PU foam in SWD, 10 evaporation cycles were conducted under 5 sun illumination (30 min illumination for each cycle) as shown Figure 3.11B. The results reveal that the Ag/Au-GO-PU foam displays excellent stability over 10 evaporation cycles without any evidence for performance decay. The high evaporation efficiency, excellent stability and long-time durability make the Ag/Au-GO-PU foam an ideal candidate for a variety of applications in solar-steam-generation and SWD.

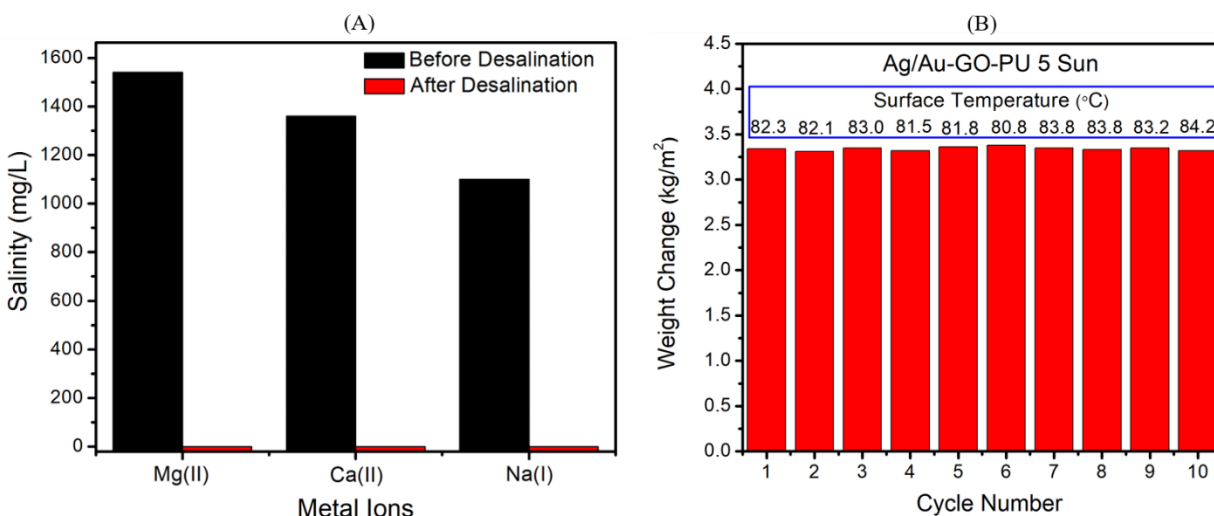


Figure 3.11. (A) Concentrations of three primary ions in the synthesized seawater sample determined by ICP-OES before and after SWD using the Ag/Au-GO-PU foam. (B) The evaporation cycle performance of the Ag/Au-GO-PU foam under constant illumination of 5 sun for 30 min for each cycle.

3.4. Conclusions

In this chapter, the development of a new class of PGPU nanocomposite foam for efficient solar water desalination is described. With the characteristics of high optical absorption, low thermal conductivity, effective water transmission, and the capacity of self-floating, the PGPU foam can be an attractive material for efficient solar steam generation. Moreover, the functional foam exhibited excellent stability due to the covalent bonds formed between GO and PU matrix. Since the materials developed were synthesized and tested on a laboratory scale, it is very difficult to make a reliable estimate of the cost of clean water produced. However, the small amount of plasmonic metal NPs needed (0.2 wt%) and the low cost of the organic materials such as polyurethane and GO are expected to lead to economically feasible materials as compared to the membrane-based water desalination technology. The current contribution offers the opportunity for improved solar photothermal energy conversion for many applications including domestic

water heating, solar-driven desalination, solar steam for industrial purposes, solar crop drying technologies, and basic solar stills to purify water in remote regions.

Chapter 04: Plasmonic Chemically Modified Cotton Nanocomposite Fibers for Efficient Solar Water Desalination and Wastewater Treatment

4.1. Introduction

The quest to find a cost-effective, durable and eco-friendly solar absorption material with flexible, porous, low weight and efficient photothermal properties is still an active area of research.^{85-88, 121} Metal NPs have been proposed to take advantage of the high efficiency of the photothermal energy conversion associated with SPR absorption.^{90, 92-94, 122} Numerous examples of noble-metal and carbon-based nanofluids are available in the literature for solar steam generation.^{17, 97, 123-124} Nanostructured carbon-based materials such as carbon nanotubes, GO and RGO have recently been applied in photothermal energy conversion as they can absorb light over the visible and NIR parts of the electromagnetic spectrum and convert the absorbed radiation into heat through nonradiative decay processes with excellent photothermal transduction properties.^{86, 107-110, 125} In the previous chapter, the utility of plasmonic-graphene polyurethane nanocomposite foams for the efficient solar steam generation was demonstrated.¹¹²

Complicated synthesis methods and high material cost are considered as the major drawbacks of using synthetic polymer materials for anchoring the solar absorbers. However, the cellulose fibers obtained from cotton biomass waste can be a cost-effective host material for anchoring plasmonic NPs. Even so, cotton fibers are inherently highly hydrophilic due to the hydroxyl functional groups on the surface of the fibers.¹²⁶⁻¹²⁷ Thus, upon contact, cotton absorbs water very rapidly and tends to sink in water.¹²⁶ In this chapter, the successful development of a new highly efficient, flexible, low weight and cost-effective PFC nanocomposite fibers for solar water desalination and for wastewater treatment. In this work, partially hydrophobic cotton is introduced as a host material for metal NPs to fabricate the PFC nanocomposite fibers as a new class of novel photothermal

materials. The developed PFC fibers float on the surface of seawater and, at the same time, allow water to be transported by capillary forces through the fibers to the external surface for solar thermal evaporation. Here, we demonstrate that these materials can significantly enhance the absorption of solar energy and the high conversion efficiency of sunlight into heat. PFC composites also offer advantages over the polymeric materials which have the limitation in performing at high temperatures, stability, and durability. This chapter is adapted from the article published in the journal RSC Nanoscale.¹³⁸

4.2. Materials and Methods

4.2.1. Materials

Commercial cotton, 2,4-toluene diisocyanate (95.0%), anhydrous dimethylformamide (99.8%), gold (III) chloride solution (99.99%), silver nitrate (99.0%), hydrazine hydrate (80%), magnesium sulfate (99.99%), calcium chloride (99.9%), sodium chloride (>99.0%). All reagents were purchased from Sigma-Aldrich and used without further purification. DI water was used in all the experiments.

4.2.2. Material Preparation

4.2.2.1. Synthesis of TDI-Cotton

In a typical synthesis, commercial cotton fibers were cut into squares (5×5×1 cm) and washed with anhydrous DMF to remove impurities and traces of water. Then the cotton squares were immersed in 25 mL of anhydrous DMF containing excess TDI for 24 hours. Modified cotton samples then washed with DMF and dried under ambient conditions.

4.2.2.2. Synthesis of Plasmonic TDI-Cotton

To synthesize 5% Au-f-C or 5% Ag-f-C samples, a TDI-cotton sample was first weighed and then immersed in a 25 mL solution containing appropriate amounts of HAuCl_4 or AgNO_3 for 6 hours. Then the samples were mildly washed with DI water and re-immersed in 25 mL of fresh DI water. To reduce the metal ions, 25 μL of hydrazine hydrate was added and the solution was microwaved using a 700 W microwave oven for 60 s (in 10 s intervals). Afterward, the samples were washed several times with cold water then dried overnight at room temperature.

4.2.3. Characterization

The TDI-Cotton fibers were characterized using the FT-IR spectroscopy using the Nicolet-Nexus 670 FTIR spectrometer (4 cm^{-1} resolution and 32 scans) diamond attenuated total reflectance. The morphology of the cotton fibers with and without plasmonic NPs was characterized by SEM (Hitachi SU-70 FE-SEM). The optical characterization of the plasmonic cotton fibers was determined using a superior micro spectrophotometer (Olis 14 CD), with reflectance power supply (CRAIC Technology, 75 W Xenon). A Newport Sol2A solar simulator with a power of 450 W was used as the source of natural sunlight for all the steam generation experiments. The concentration of metal ions in solution before and after desalination was determined by ICP-OES

4.2.4. Solar Steam Generation Experiments

The same experimental set up using the solar simulator 450 W, Newport Sol2A, Class ABA was used as shown in Figure 3.1 in chapter 3. The solar steam generation rates of three samples, Au-f-C, Ag-f-C, and Ag/Au-f-C were measured and compared with pure DI water under three solar

irradiation intensities of 1, 5 and 8 kW/m² over 30 mins. The different solar intensities were obtained using a focusing lens (208.2 mm focal length and 279.4 mm diameter). The sample was floated on top of the water surface in a 50 mL Petri dish filled with pure DI water placed on a calibrated electronic balance. The temperatures of the irradiation surface and bulk water (water below the sample) were recorded using an IR thermometer and a thermocouple, respectively. The evaporation rate was calculated as the change in the recorded mass of water normalized by the area of the irradiated sample and the corresponding time interval. The weight changes were recorded every 5 minutes over a period of 30 minutes. Then, the obtained data were used to calculate the evaporation rate and solar-to-vapor efficiencies. All the experiments were carried out at room temperature of 20 ± 1 °C and humidity of ~40%.

4.2.5. Solar Water Desalination Experiments

To evaluate the potential of the plasmonic cotton in SWD, a sample of artificial seawater containing 1500 ppm Mg²⁺, 1250 ppm Ca²⁺, and 1000 ppm Na⁺ was used for the steam generation experiment. Another Petri dish was used to condense the generated steam which was later collected by a clean pipette. The condensed steam sample then analyzed by ICP-OES to determine the concentration of the primary ions (Na⁺, Mg²⁺, and Ca²⁺) naturally existing in the seawater.

4.2.6. Wastewater Treatment

To evaluate the utility of PFC in wastewater treatment, samples were tested in two methods. In the first experiment, steam generation was carried out using water at extreme pH values of 2 and 10 using aqueous solutions of HCl and NaOH, respectively. In the second experiment, an organic dye, methylene blue with a concentration of 10 ppm was used as a

model of a polluted water sample. Steam generation experiment was carried out using the dye solution instead of DI water at 5 kW m^{-2} solar intensity and the absorption spectra of the dye solution and the steam were compared to evaluate the purification.

4.2.7. Solar Steam Generation Recycling Experiments

Ten solar steam generation cycles were carried out to evaluate the recyclability and durability of the Ag/Au-f-C sample. In each cycle, the cotton sample was illuminated under solar light supplied by the solar simulator with a light density of 5 kW m^{-2} for 30 minutes and the weight changes of water and the temperature of the steam were determined. After each cycle, the sample was cooled down under ambient conditions for the next cycle.

4.3. Results and Discussion

A summary of the synthesis of the PFC fibers is illustrated in Figure 4.1. The objective of the modification is to covalently attach the TDI molecules to the cellulose fibers through the formation of a stable urethane linkage between TDI and the hydroxyl groups in the cellulose fibers. The TDI molecules contain phenyl hydrophobic groups which replace some of the hydroxyl groups on the surface of the cotton fibers. Therefore, the TDI functionalization changes the intrinsic hydrophilicity of the cotton fibers making it partially hydrophobic. Due to this modification, functionalized cotton samples can float on the surface of the water allowing the spontaneous flow of water through the fibers driven by a capillary force. To provide a strong solar absorber to enable efficient photothermal energy conversion, plasmonic Au and Ag NPs are anchored to the surface of the TDI-modified cotton fibers through strong electrostatic adsorption of the Au and Ag ions by the amino and amide functional groups of the functionalized cotton fibers. The next step involves the rapid reduction of the metal ions on the surface of the TDI-

modified cotton fibers by hydrazine hydrate under fast microwave heating (50 s). The rapid reduction of the adsorbed metal ions is expected to lead to pulsed nucleation under limited growth conditions due to the low concentration of the metal ions thus resulting in the formation of well-dispersed plasmonic NPs within the PFC fiber.¹¹⁴

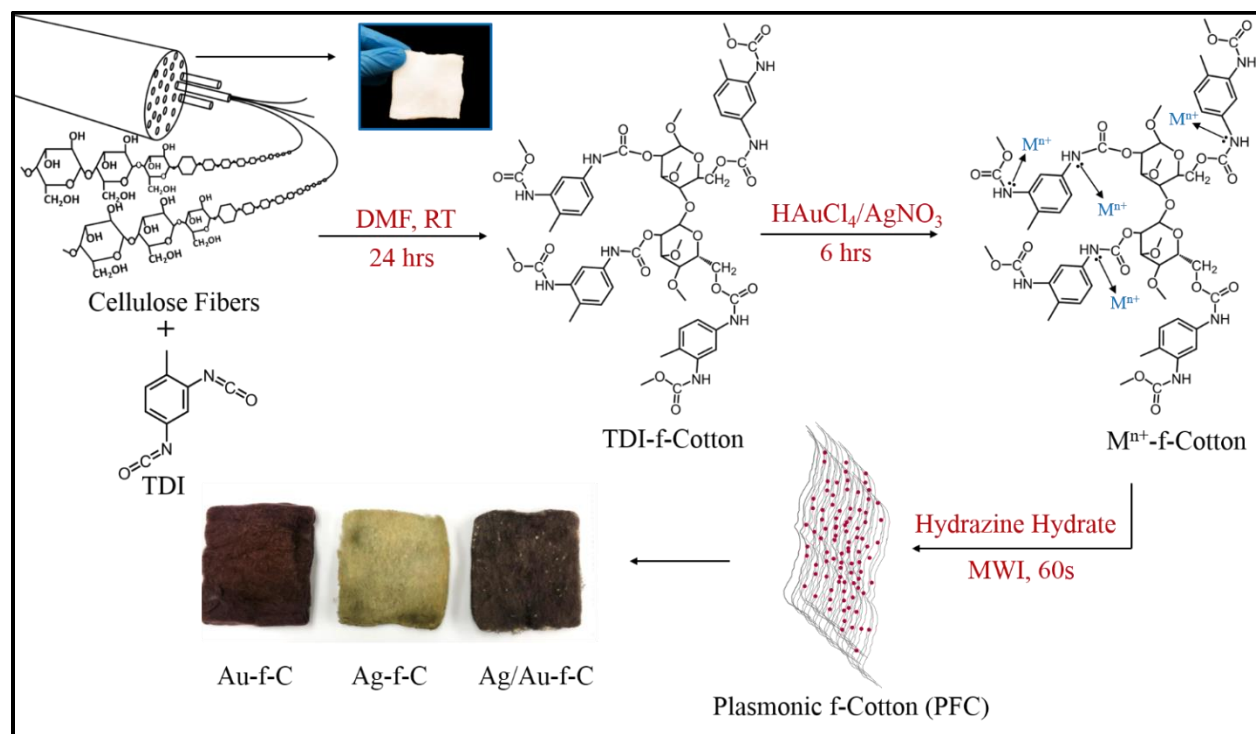


Figure 4.1. Design strategy and general steps involved in the synthesis of PFC samples.

The outcome of the modification is shown in Figure 4.2 which shows the difference of buoyancy of pure cotton and TDI functionalized cotton fibers. It is clear that the TDI-functionalized cotton takes up much less water than the un-functionalized pure cotton. The process of water transport in the un-modified pure cotton is described by a sequence of capillary-driven convection over the external surface, radial flow between the fibers along the length, and diffusion into the individual fibers leading to extensive uptake of water which results in the sinking of the wet cotton in water.

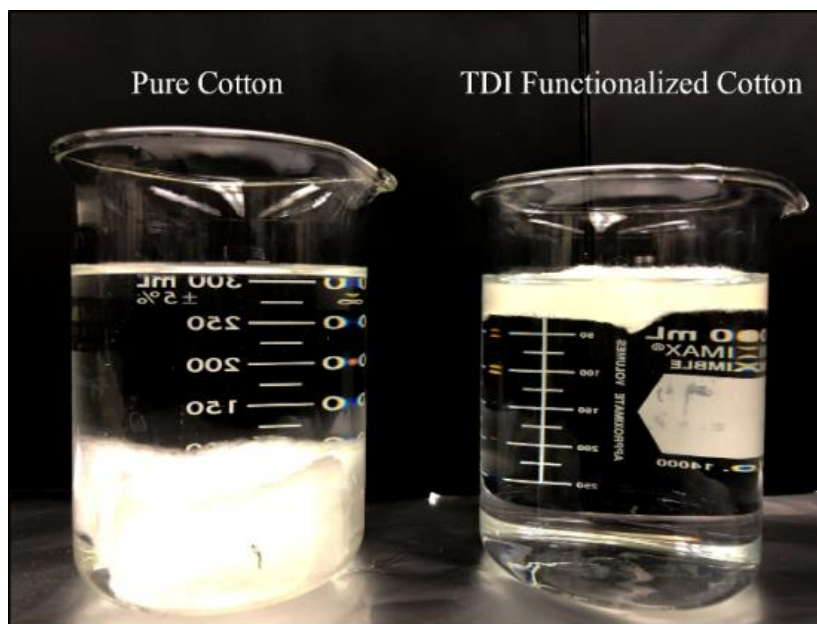


Figure 4.2. The difference of the hydrophilicity of the pure cotton and TDI functionalized cotton.

The FT-IR spectra of pure cotton and TDI functionalized cotton fibers are shown in Figure 4.3. The broad peak from $3100\text{--}3500\text{ cm}^{-1}$ and the strong shoulder peak around 1050 cm^{-1} correspond to the O-H and C-O stretching vibrations of hydroxyl functional groups of cellulose fibers, respectively. The TDI functionalized cotton fiber also shows a less prominent peak in the same range as of the O-H stretching vibrations indicating that the material still has some hydroxyl groups left to maintain hydrophilicity to channel water to the evaporation surface. The introduction of the urethane linkage between cotton fibers and TDI molecules is evident by the peaks around 1710 and 1535 cm^{-1} which are attributed to the C=O stretching vibrations and N-H bending respectively as shown in the magnified spectrum presented in Figure 4.3B.¹²⁸⁻¹²⁹ Therefore, the presence of the C=O and N-H bending peaks proves the successful functionalization of the cotton fibers

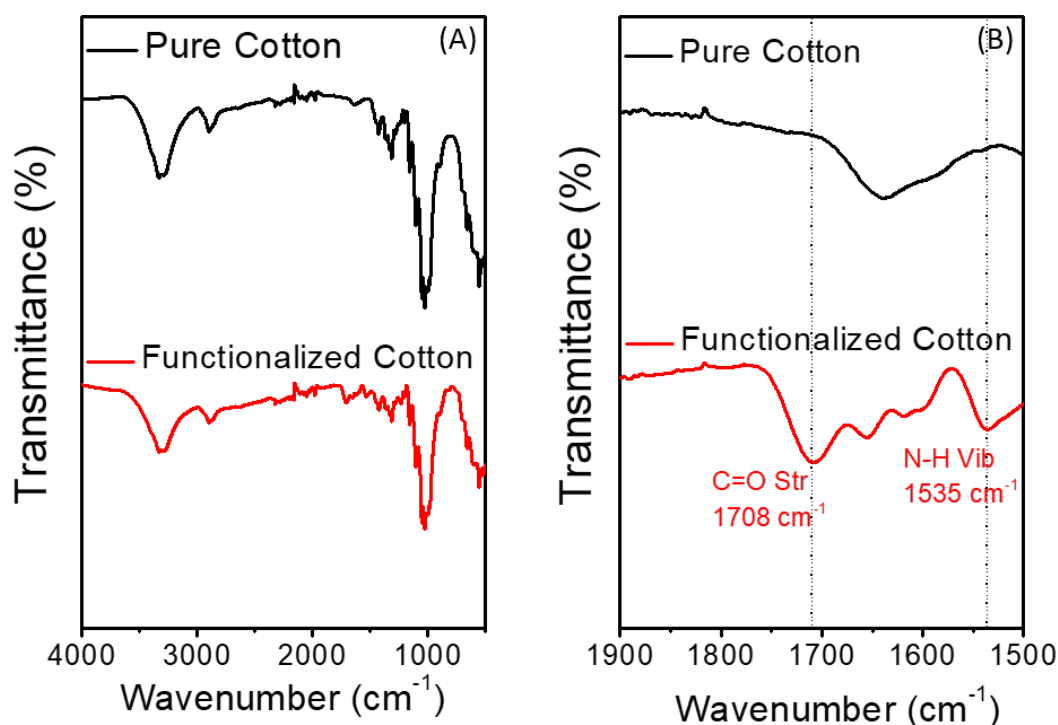


Figure 4.3. FT-IR spectra of pure cotton and TDI functionalized cotton. (A) Full scale, (B) Expanded region between 1500 cm^{-1} and 1900 cm^{-1} .

Figure 4.4A and B display the UV-vis absorption spectra of the Au-f-C and Ag-f-C nanocomposite fibers. Both the Au-f-C and Ag-f-C fibers exhibit broad SPR bands with peak maxima around 538 and 437 nm respectively.^{15, 111} The absence of a capping agent during the synthesis of the NPs results in wide size distributions and broad SPR absorption bands. However, broad SPR absorption bands can be beneficial for applications that harness solar energy since the material can utilize a significant portion of the solar spectrum and effectively convert the photon energy into thermal energy, thus the solar to steam conversion efficiency can be significantly increased.

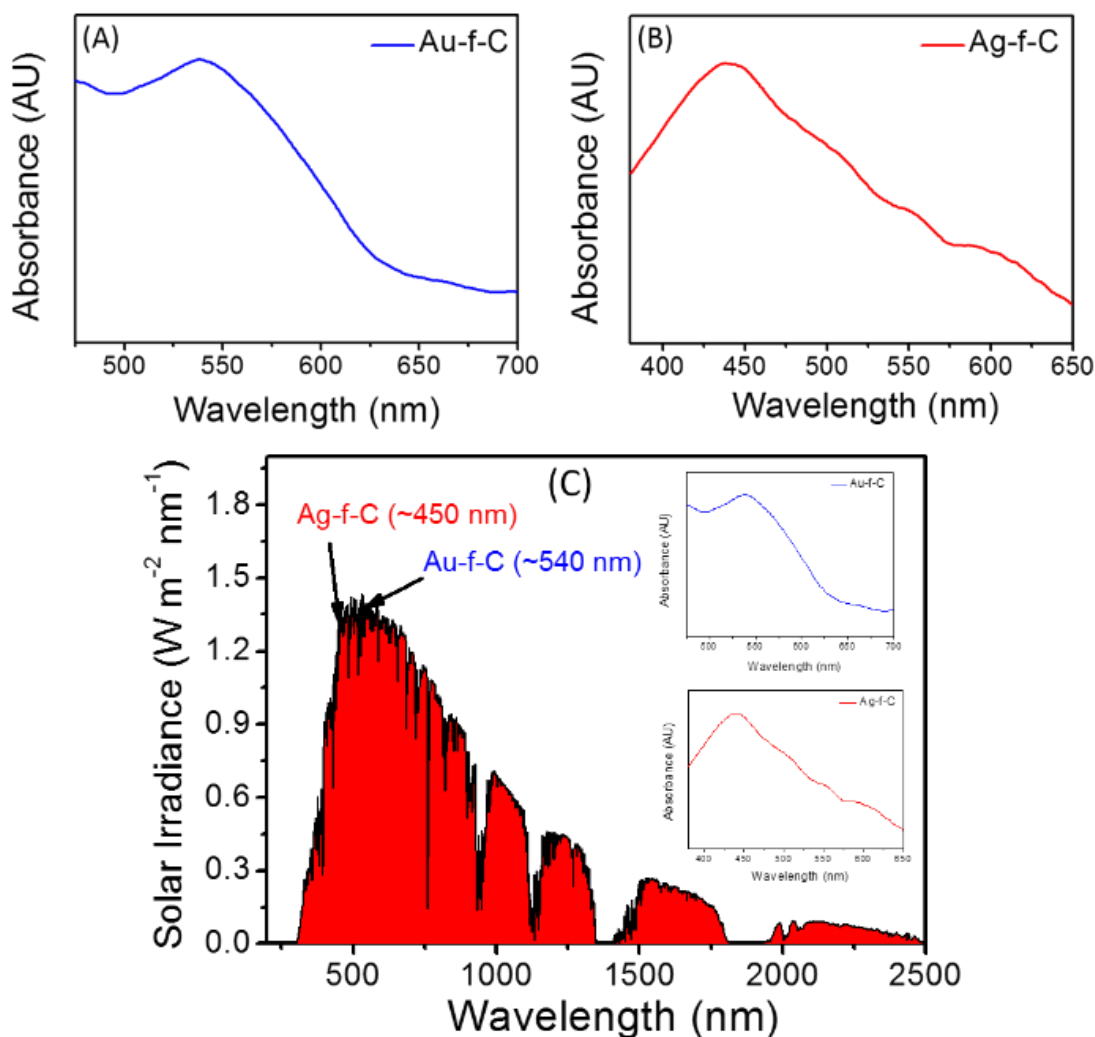


Figure 4.4. UV-Vis absorption spectra of (A) Au-f-C, (B) Ag-f-C nanocomposite fibers and (C) Solar spectral irradiance (AM 1.5 G) with the UV-Vis absorption spectra of the Au-f-C and Ag-f-C fibers (inset).

Moreover, having both gold and silver NPs in the same composite can effectively increase the harnessed range of the solar spectrum.¹¹² Figure 4.4C displays the reference solar irradiance spectrum (under AM 1.5 G) with the UV-visible absorbance spectra of the Au-f-C and Ag-f-C fibers shown in the inset.¹⁰ It is clear that the maximum absorbance of the Au-f-C and Ag-f-C samples lies in the spectral region with the highest solar irradiance which is beneficial for the effective photo-thermal energy conversion.

The surface compositions of the Au-f-C and Ag-f-C nanocomposites are further analyzed using XPS. The Au 4f spectrum displayed in Figure 4.5A clearly shows the presence of Au⁰ NPs within the Au-f-C composite. The strong doublet at 84.5 eV and 88.1 eV corresponds to the Au 4f_{7/2} and Au 4f_{5/2} states of metallic Au. The less prominent doublet (89.5/86.2 eV) is ascribed to the surface oxidized Au³⁺ ions. The broadness of the Au³⁺ peaks relative to those of Au⁰ could be explained by the chelation of Au³⁺ ions by the amine groups present in the functionalized cotton.¹³⁰⁻¹³¹ The Ag 3d spectrum of the Ag NPs, displayed in Figure 4.5B, consists of two main peaks at 368.1 eV and 374.1 eV which are assigned to the Ag 3d_{5/2} and 3d_{3/2} states of metallic Ag respectively.¹³² The two small peaks at 375.5 eV and 370.2 eV are most probably due to the presence of a small fraction of silver oxide species on the surface of the NPs. Since the samples are stored under ambient conditions, the formation of an oxide layer over the surface of the Ag NPs is inevitable.¹³³ However, it is also possible that these peaks represent the strong association of silver ions with the amine groups of the urethane bond.¹³⁴

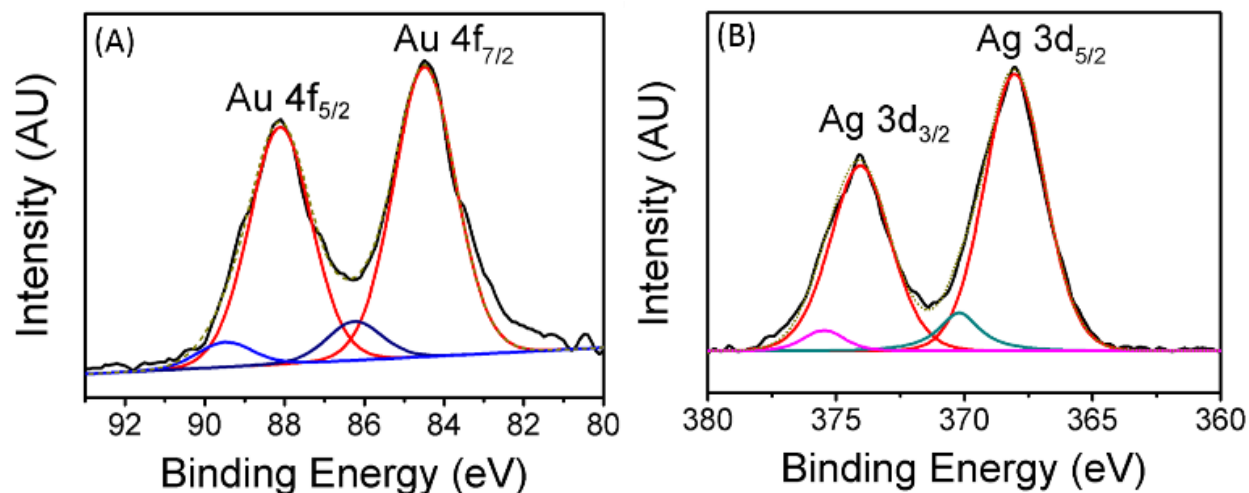


Figure 4.5. XPS spectra of the Au 4f electron (A) and the Ag 3d electron (B) in the Au-f-C and Ag-f-C fibers, respectively.

SEM images of the TDI-functionalized cotton fibers and the Au-f-C and Ag-f-C nanocomposite fibers are shown in Figure 4.6. According to the SEM images, the size distributions of the Au and Ag NPs are in the range of 70 to 100 nm with no evidence of agglomeration. Also, it is evident that the NPs are uniformly distributed on the surface of the functionalized cotton fibers. Compared to support materials with a planar morphology, materials with fibrous morphology provide a higher surface area support for the dispersion of the NPs.¹¹² Also, the introduction of the amine and amide functionality to the cotton fibers facilitates the chelation of the plasmonic metal ions on the surface of the cotton fibers uniformly.

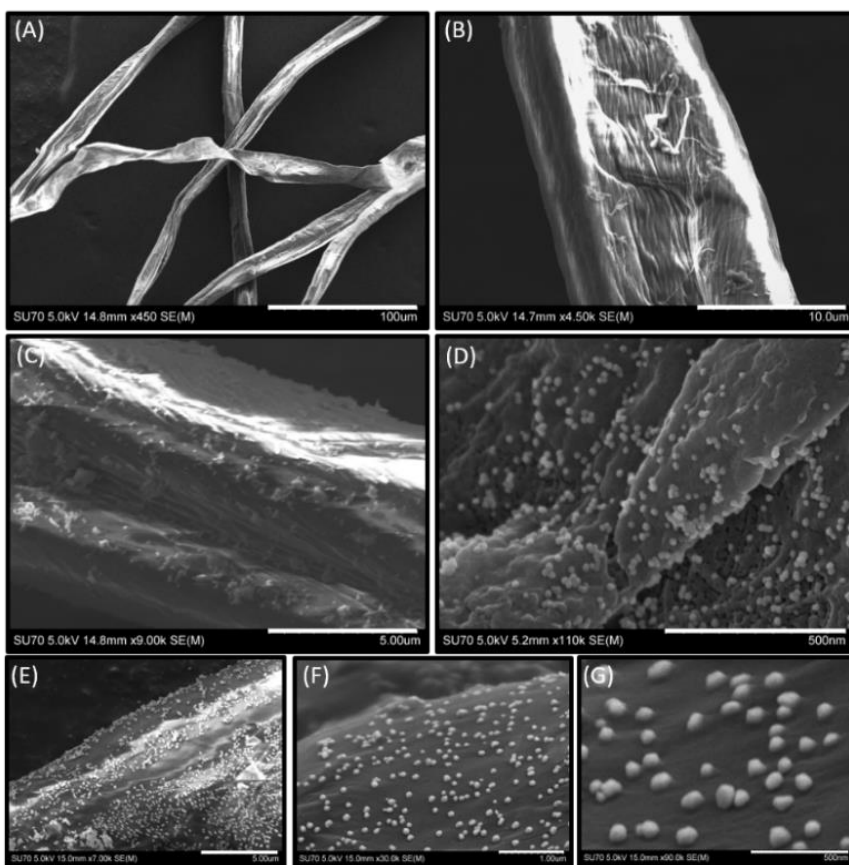


Figure 4.6. SEM images of NP free functionalized cotton fibers (A and B), Au-f-C nanocomposites (C and D) and Ag-f-C nanocomposites (E-G). The scale bars of the images A to G are 100, 10, 5, 0.5, 5, 1 and 0.5 μm, respectively.

To evaluate the solar steam generation efficiency for different PFC solar thermal converters, four samples of nanoparticle-free functionalized cotton (TDI-cotton), Au-functionalized cotton (Au-f-C), Ag-functionalized cotton (Ag-f-C), and Ag/Au-functionalized cotton (Ag/Au-f-C) nanocomposites were tested. All the samples were tested for steam generation and compared with pure DI water in the absence of any solar absorber under three different solar illuminations of 1 kW/m², 5 kW/m² and 8 kW/m² over 30 min using the solar simulator 450 W, Newport Sol2A, Class ABA. Figure 4.7 displays digital images of the steam generating PFC samples.

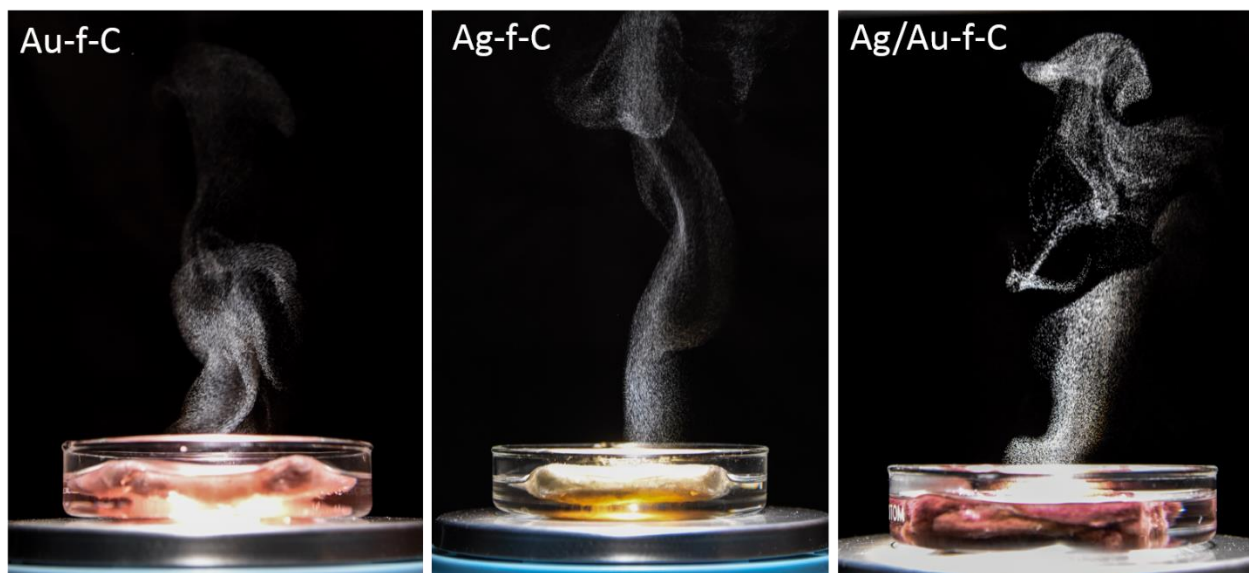


Figure 4.7. Visual images of the PFC samples during the steam generation experiment

The results presented in Figure 4.8A and B display the normalized steam generation rates at solar illumination of 1, 5 and 8 kW m⁻². At all solar illumination intensities, the plasmonic free functionalized cotton exhibits the lowest evaporation rate (0.82, 1.70 and 4.16 kg m⁻² h⁻¹ at 1, 5 and 8 sun, respectively) due to the absence of any solar absorbers. The small enhancement effect in the evaporation rate over pure water (2 times at 1 sun) is attributed to surface evaporation through the porous structure of the fibers which results in minimizing the heat loss by bulk water.

Introduction of plasmonic NPs on the functionalized cotton surface significantly enhances the rates of solar steam generation compared to the control sample. At one sun, the Ag/Au-f-C sample could evaporate water at a rate of $1.4 \text{ kg m}^{-2} \text{ h}^{-1}$ whereas plasmonic free functionalized cotton could only evaporate about $0.8 \text{ kg m}^{-2} \text{ h}^{-1}$. At 8 sun, the difference is even higher showing an evaporation rate 2.8 times higher than the plasmonic free sample. Under all the solar intensities, Ag/Au-f-C sample demonstrated the highest steam generation rates (1.4 , 6.7 and $11.3 \text{ kg m}^{-2} \text{ h}^{-1}$ under 1 , 5 and 8 sun, respectively). The enhanced efficiency of the Ag/Au-f-C sample is due to the presence of both Au and Ag NPs as

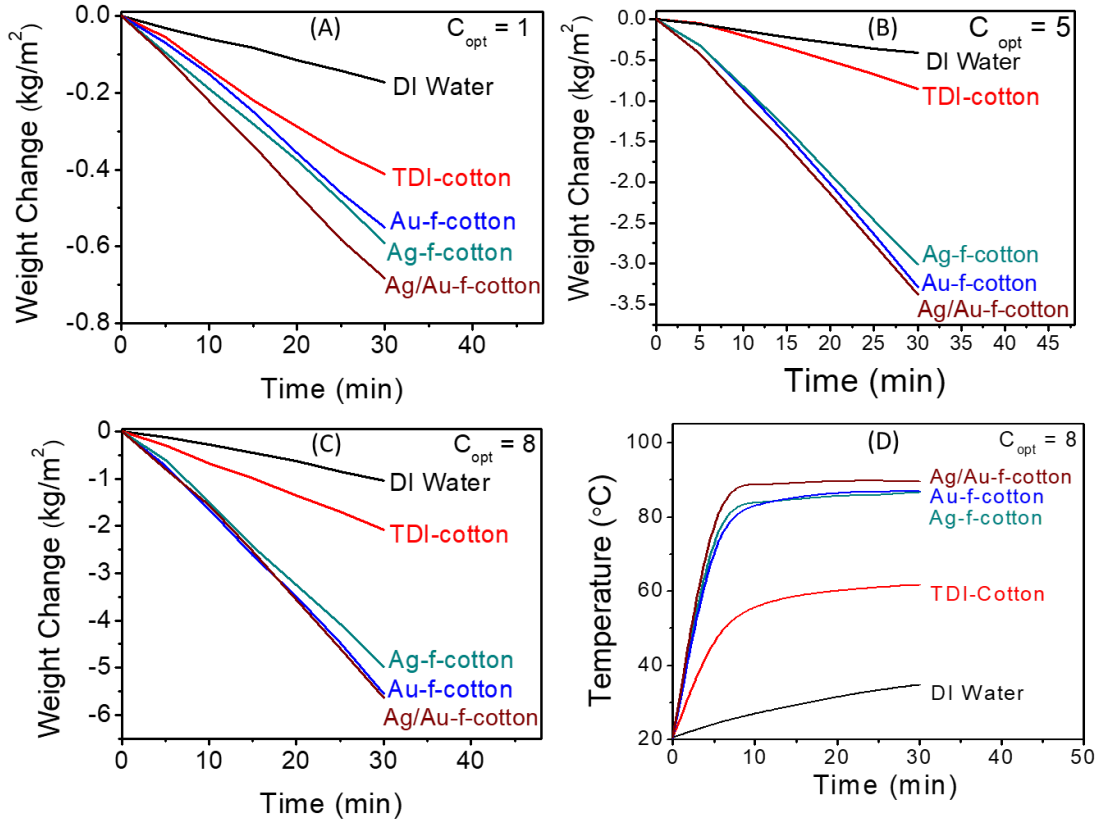


Figure 4.8. Solar steam generation data for different PFC samples under different solar intensities (A) 1 kW m^{-2} (optical concentration $C_{\text{opt}} = 1$), and (B) 5 kW m^{-2} (optical concentration $C_{\text{opt}} = 5$). (C) 5 kW m^{-2} (optical concentration $C_{\text{opt}} = 5$) and (D) Temperature change at the surface of different PFC samples and DI water after solar illumination for 30 min under optical concentrations of $C_{\text{opt}} = 8$.

plasmonic absorbers within the cotton nanocomposite fibers. As shown in Figure 4.4, Au and Ag NPs possess different absorption maxima in the visible spectra. Therefore, Ag/Au-f-C fibers which contain 1:1 mixture of Au and Ag NPs can harness a much larger portion of the solar spectrum compared to the PFC samples containing only one type of plasmonic NPs. The low thermal conductivity of the cotton fibers (0.065 W/mK) also helps the PFC samples to isolate the heat and minimize the heat loss to bulk water.

Figure 4.8D displays the temperature profiles of the different samples on the irradiation surface at the solar intensity of 8 kW m^{-2} . The trend observed in the surface temperature profile correlates with the general trends of the steam generation rates shown in Figure 4.8A, B and C. The Ag/Au-f-C sample exhibits the largest increase in the surface temperature at 8 sun illumination. After 5 minutes of exposure, the surface temperature of the Ag/Au-f-C sample increased from 20.6 to 88.8 °C while the blank water sample only changes from 20.5 to 24.4 °C after the same period of illumination time. Under 1 sun intensity, the maximum surface temperatures of the Au-f-C, Ag/Au-f-C, Ag-f-C samples after 30 min of illumination time reach 31.8, 30.5 and 30.0 °C, respectively. These low temperatures indicate the high evaporation efficiency of the PFC fibers under 1 sun.

Figure 4.9 compares the solar-to-vapor efficiencies of the PFC fibers at three solar intensities (1, 5 and 8 sun). The thermal efficiency is calculated based on the equation 3.1.^{107, 124-125} The results reveal that the Ag/Au-f-C sample exhibits the highest thermal efficiencies of 86.3, 82.9 and 94.3 % for a solar-enabled steam generation under 1, 5 and 8 sun, respectively. The calculated efficiency at 8 sun is considered one of the highest values reported for photothermal energy conversion materials used for solar water desalination.^{93, 107-110, 112, 120, 124-125, 135}

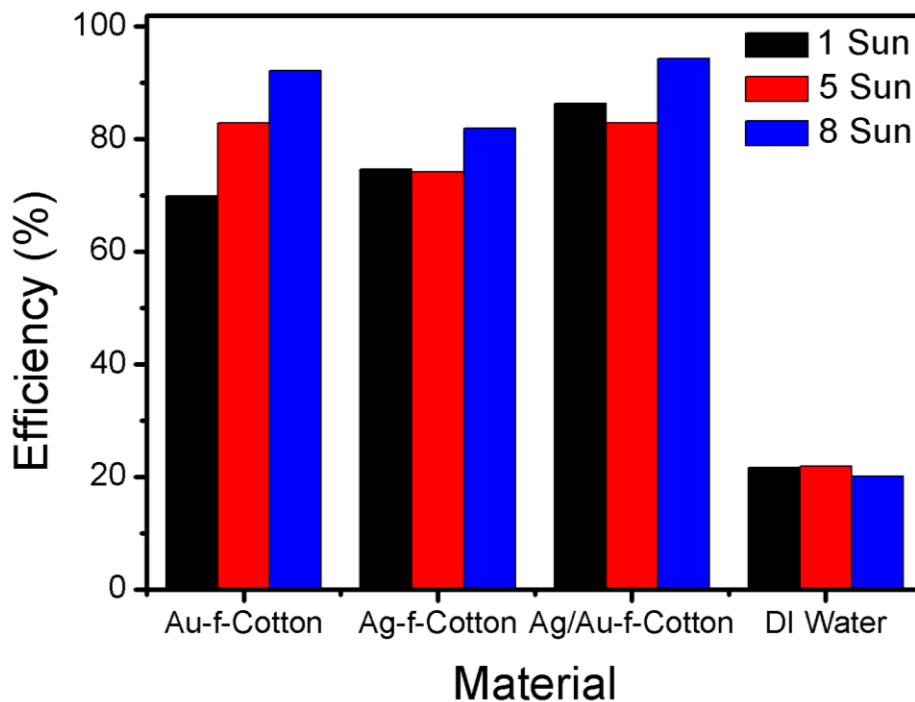


Figure 4.9. The evaporation efficiency of different PFC samples under 1, 5, and 8 kW m⁻² solar illumination.

Under the solar intensity of one sun, the Ag/Au-f-C sample exhibits a solar-to-vapor efficiency of 86.3% with only about 14% loss of energy due to the reflection of the incident light, conduction, and convection.¹²¹ Reflection measurements of the Ag/Au-f-C sample indicated an average percentage reflection of around 20% in the spectral regions where they exhibit the maximum absorbance. The maximum surface temperature of the Ag/Au-f-C sample after 30 min irradiation is measured as 30.5 °C while the average bulk temperature of the water is 22.2 °C. Using the average length of the conductive path of the PFC samples as 1 cm and assuming the PFC sample possess a similar thermal conductivity as of pure cotton (0.026 W/m K),¹³⁴ the conductive heat flux for the Ag/Au-f-C sample can be calculated as 21.6 W m⁻². Considering the input solar intensity at 1 sun (1 kW m⁻²), the calculated conductive heat loss is only ~ 2.2%. The temperature difference between the bulk water and the irradiation surface is a critical factor for the magnitude

of heat loss by convection and irradiation. However, since after 30 minutes of irradiation under 1 sun the temperature difference between the sample surface and bulk water is found to be only ~8 °C, the convection and radiation heat loss can be estimated as 8% comparable to carbonized mushrooms materials.¹²¹

To further evaluate the utility of the PFC fibers in solar SWD and wastewater treatment, the concentrations of the three primary ions Na^+ , Ca^{2+} and Mg^{2+} naturally present in seawater were determined in the condensed water obtained from the desalination system using ICP-OES. Figure 4.10A shows that the concentrations of the representative ions are significantly reduced after the SWD using the Ag/Au-f-C fiber. After the experiment, the concentrations of the Na^+ , Ca^{2+} and Mg^{2+} ions decreased significantly from the original values of 1000, 1250 and 1500 mg/L to 0.05, 0 and 0.1 mg/L, respectively. The ion concentration values after the SWD by the PFC are well below the standard values reported by the US Environmental Protection Agency and the World Health Organization, as well as below the values obtained by common SWD techniques such as membrane (10–500 ppm) and distillation (1–50 ppm).^{37, 86, 93} Figure 4.10B represents the reusability test done for the Ag/Au-f-C sample in SWD. According to the results, the Ag/Au-f-C sample retains its stability over ten desalination cycles without any performance change. This excellent stability and reusability demonstrate that the PFC fibers are highly suitable for various applications in solar SWD and steam generation

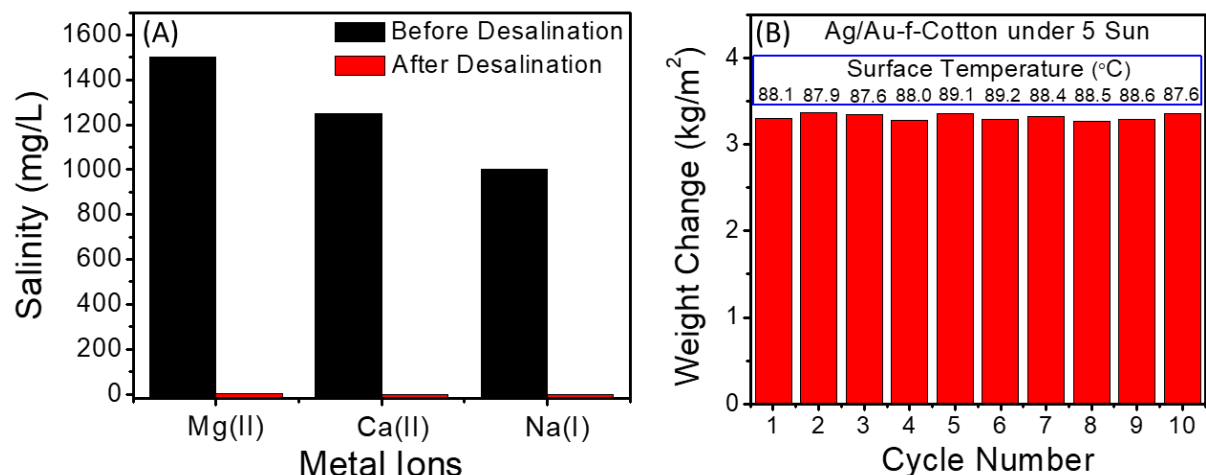


Figure 4.10. (A) The concentrations of three primary metal ions in an artificial seawater sample before and after desalination and (B) Recyclability test of the Ag/Au-f-C sample during 10 cycles under constant illumination of 5 kW m⁻² for 30 minutes.

Finally, the utility of the Ag/Au-f-C sample was also tested for SWD under acidic and basic environments and for the purification of wastewater containing an industrial dye. As shown in Figure 4.11A, the Ag/Au-f-C sample could function in an acidic solution at pH 2 or in a basic solution at pH 10 under a solar intensity of 5 kW m⁻² for 30 minutes without any significant decrease in the performance. Steam generation rates at pH 2, 7 and 10 were 6.72, 6.70 and 6.84 kg m⁻² h⁻¹, respectively. Au and Ag metal NPs are well known for their inherent resistance to acidic and basic environments.^{19, 136} Therefore, the PFC fibers can be ideal candidates for solar driven steam generation techniques that can be used for wastewater treatment. Figure 4.11B demonstrates the successful application of the Ag/Au-f-C sample in solar wastewater treatment. Methylene blue dye was used as a model pollutant. The absorption spectra of the polluted water containing 10 ppm methylene blue dye and the condensed steam sample after the solar illumination clearly confirms the complete removal of the dye from the condensed steam sample.

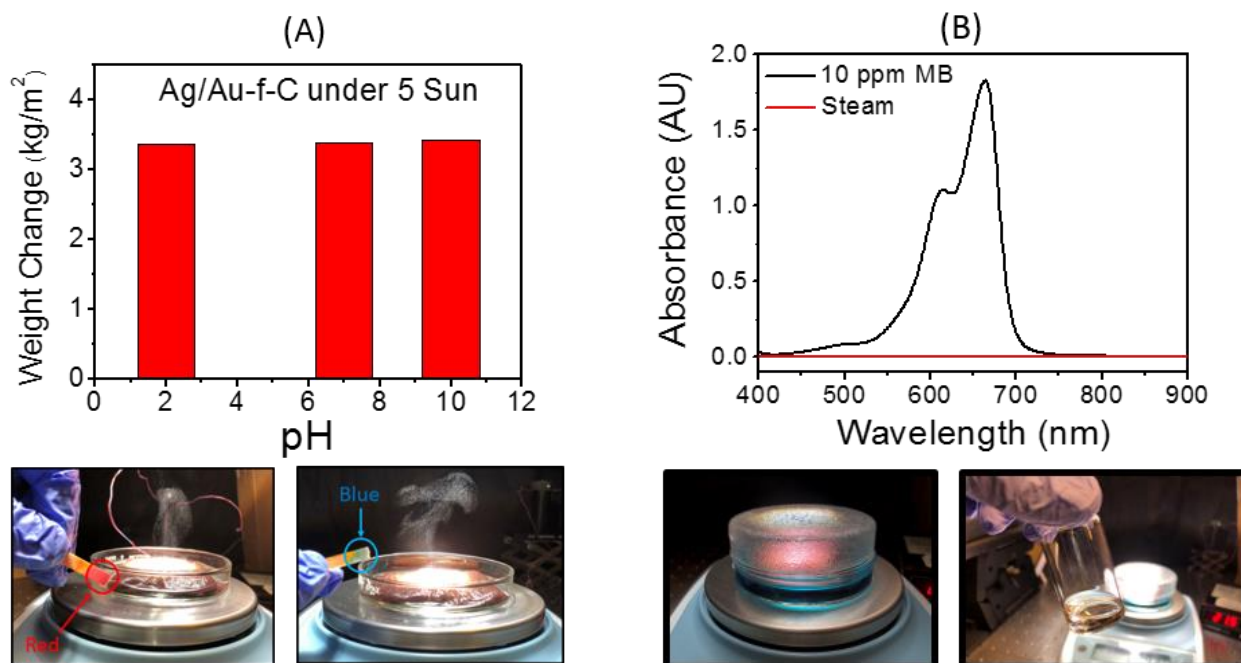


Figure 4.11. Applications of the PFC materials (Ag/Au-f-C as the representative sample) in wastewater treatment. (A) Stability of the Ag/Au-f-C sample in extreme pH values (pH 2 and 10) and (B) UV-vis spectra of the model pollutant methylene blue, before the steam generation experiment and after condensation of the steam.

4.4. Conclusions

In conclusion, a new class of PFC nanocomposite fibers was fabricated for efficient solar water desalination. With the unique features such as high optical absorption, low thermal conductivity, effective water transmission, and the capacity of self-floating, the PFC foam can be an attractive material for efficient solar steam generation and wastewater treatment. Moreover, the material exhibits excellent stability over multiple cycles indicating its reusability in practical applications. Utilization of low-cost materials such as cotton and low plasmonic metal loading leads to fabricate an economically feasible material compared to other desalination techniques such as reverse osmosis and membrane-based filters.

Chapter 05: Low-Cost Functionalized Carbonized Cotton Device for Efficient Solar Steam Generation

5.1. Introduction

In recent years, solar steam generation gained significant attention due to its interesting applications in SWD,⁸³ wastewater treatment,¹³⁷⁻¹³⁸ domestic water heating and even autoclave-based disinfection.¹³⁹ Due to the increasing energy demand and the environmental impact of fossil fuel consumption, it is palpable to utilize abundant and clean renewable energy sources like solar energy in energy-yielding applications such as SWD. However, conventional technologies like solar stills directly heat the bulk water and experience significant optical and systematic energy losses.¹⁴⁰ Therefore, modern solar steam generation devices are more lenient towards heat localization through efficient photothermal energy conversion materials. Thus far, various materials have been utilized in fabricating steam generation devices such as noble metal NPs,^{112, 138, 141-143} metal oxides,^{22, 144-145} metal sulfides,^{144, 146} carbon-based nanofluids¹⁶ and carbon-based composites.^{99, 147} However, the utility of plasmonic metal NPs can be economically disadvantageous. Also, the usage of bulk metals and metal oxides can lead to low solar absorption and significant heat loss through heat dissipation to bulk water. On the contrary, carbon-based materials can be cheap, eco-friendly, energy efficient due to the low heat conductivity and most importantly they can absorb light in a wide wavelength range expanded over visible and NIR regions of solar spectrum.^{24, 30, 106, 109, 125, 148-149} Nevertheless, carbonized materials also possess several drawbacks including material shedding, hydrophobicity, and limited durability.

Generally, solar steam generation materials are designed to float on water in order to efficiently absorb solar energy. Often, the floating capability is an inherent property of the material which is resulting from porosity or hydrophobicity^{138, 150} of the material itself. However, it is not rare to

find photothermal materials which are mounted on low-density polymer foams like polyethylene, polystyrene, polyurethane, etc. to facilitate the buoyancy.^{108, 125} Other than the buoyancy, the low thermal conductivity of these polymer foams helps to effectively localize the heat and minimize the conductive heat loss. However, during the long-term steam generation procedures, solar absorbers or the foam supports eventually start dissipating heat into the bulk water due to the heat buildup. One way to address this issue is to reduce the contact surface area between bulk water and solar absorber. One of the design strategies involves elevating the irradiation surface above the water surface and providing a continuous flow of water to the solar absorber. For instance, Zhu et al. have used a natural design of mushrooms to minimize conductive heat loss.¹⁵¹

This chapter presents a novel design to mitigate the issues associated with the conductive heat loss by utilizing materials that are economically viable. Inspired by natural designs like mushrooms, carbonized cotton solar steam generation device is consisted of an irradiation surface which is a bilayer of functionalized carbonized cotton and pristine cotton and a frame of low-density polyethylene foam. To feed water to the irradiation surface a stem made of pristine cotton was utilized. The unique design helped to solve some of the critical issues associated with the applicability of carbonized materials in solar steam generation such as material shedding, conductive heat loss, and durability.

5.2. Materials and Methods

5.2.1. Materials

Commercial cotton, nitric acid (70% (w/w), low-density polyethylene foam, methylene blue.

5.2.2. Material Preparation

5.2.2.1. Synthesis of Carbonized Cotton

First, commercial cotton was washed with DI water to remove impurities and dried at 80 °C overnight. Then, the dried cotton was carbonized at 600 °C for one hour under nitrogen to obtain CC. To introduce hydrophilicity to the CC material, it was immersed in a 50% HNO₃ solution and refluxed at 80 °C for one hour. Then, the resultant hydrophilic CC material was washed several times with DI water until the washings are neutral in pH. Finally, the material was dried at 80 °C overnight.

5.2.2.2. Solar Steam Generation Device Preparation

To improve the durability, and minimize the conductive heat loss to bulk water, the carbonized carbon material was mounted in a polyethylene foam block on a layer of a pristine unmodified cotton layer. A cotton wool stalk was included to provide a continuous water supply to the evaporation surface. A schematic representation of the general setup of the solar steam generation device is illustrated in Figure 5.1.

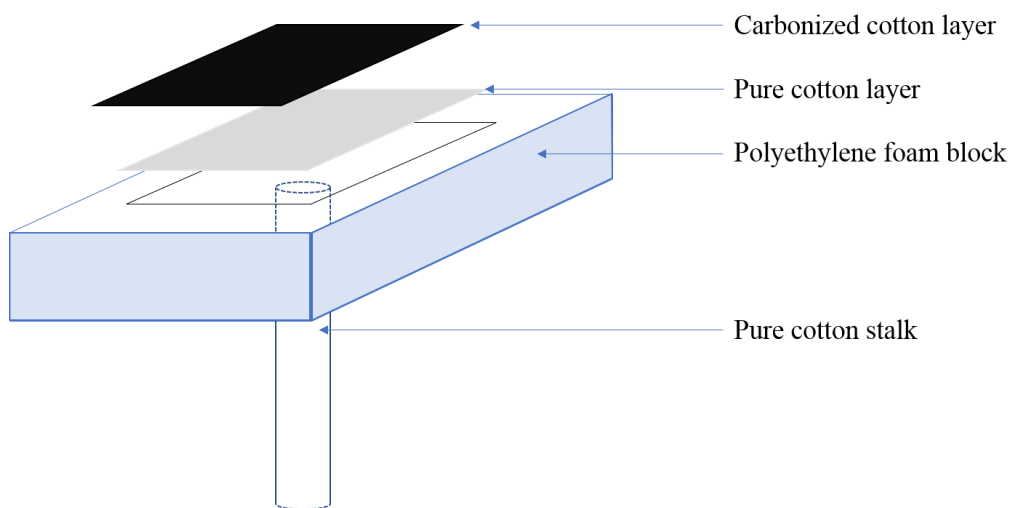


Figure 5.1. Schematic representation of the solar evaporation setup.

5.2.3. Characterization

Pure cotton fibers and CC fibers were characterized using Nexus 670 FTIR spectrometer, (4 cm^{-1} resolution and 32 scans) using diamond attenuated total reflectance. Raman spectrum for the CC fibers was obtained from Thermo Scientific DXR SmartRaman (532 nm). Surface structure and morphology of the pure and CC samples were characterized using Hitachi SU-70 FE-SEM. The optical characterization of the CC fibers was determined using a diffuse reflectance accessory attached to a Cary 6000i UV-vis-NIR spectrophotometer (Agilent Technologies). The XPS characterization of the CC was done using PHI VersaProbe III Scanning XPS Microprobe.

5.2.4. Solar Steam Generation Experiments

A class ABA, Newport Sol2A, 450 W solar simulator was used to conduct the solar steam generation experiments. The solar steam generation rate of the CC device was measured under solar intensities of 1, 5 and 8 kW m^{-2} . Also, a similar device was prepared to contain a sheet of pure cotton instead of the CC sheet as a control. Solar steam generation rates were compared with respect to the pure cotton device and DI water under the same solar intensities. Solar intensities 5 and 8 kW m^{-2} were obtained using a Fresnel lens (208.2 mm focal length and 279.4 mm diameter). In a typical steam generation experiment, the solar steam generation device was contained in a 100 mL beaker containing around 75 mL of water. The beaker was placed on a calibrated electronic balance. The temperature of the evaporation surface and the bulk water was measured using an IR heat sensor and a thermocouple respectively. Normalized solar steam generation rates were calculated based on the weight loss of the water body per unit area of irradiation at a corresponding time interval (5 min). Normalized steam generation data were used to calculate the solar-to-vapor efficiency of the CC solar steam generation device. All the steam generation experiments were carried out at room temperature of $20 \pm 1\text{ }^{\circ}\text{C}$ and humidity of ~60%.

5.2.5. Wastewater Treatment

To evaluate the applications of the CC steam generation device in wastewater treatment, a 10 ppm methylene blue solution was used as a model pollutant. Steam generation experiment was carried out for the dye solution instead of DI water under a solar intensity of 5 kW m^{-2} and the resultant steam was condensed and analyzed using HP-8453 UV-visible spectrophotometer.

5.2.6. Recycling Study of the CC Solar Steam Generation Device

To evaluate the recyclability of the CC solar steam generation device, solar steam generation experiments were carried out for 10 cycles at a light density of 5 kW m^{-2} . Each cycle was carried out for 30 minutes and the device was cooled down to room temperature after each cycle by flushing cold DI water through the device.

5.3. Results and Discussion

Figure 5.2 shows the comparative FT-IR spectra of the pure cotton fibers and CC fibers. The peak around 3325 cm^{-1} is attributed to the hydroxyl functional groups which are present in abundance in pristine cotton fibers. Peaks at 2900 , 1426 and 1054 cm^{-1} are ascribed to C-H stretching, CH_2 asymmetric bending and C-O stretching respectively.¹⁵² After pure cotton is carbonized at 600°C , most of the hydroxyl functional groups are removed and black carbonaceous structure is left which is hydrophobic due to the absence of polar functional groups. Since the hydrophobic CC cannot transport water to the evaporation surface, an acid treatment was done to introduce oxygen functional groups such as hydroxy groups to make the material slightly hydrophilic. The peak for O-H stretching frequency of the acid-treated CC is not prominent and most likely overlapped with the C-H stretching peak. However, a broad peak ranging from 1000 - 1500 cm^{-1} is clearly visible which can be ascribed to overlapped peaks of C-H bending and C-O stretching frequencies.

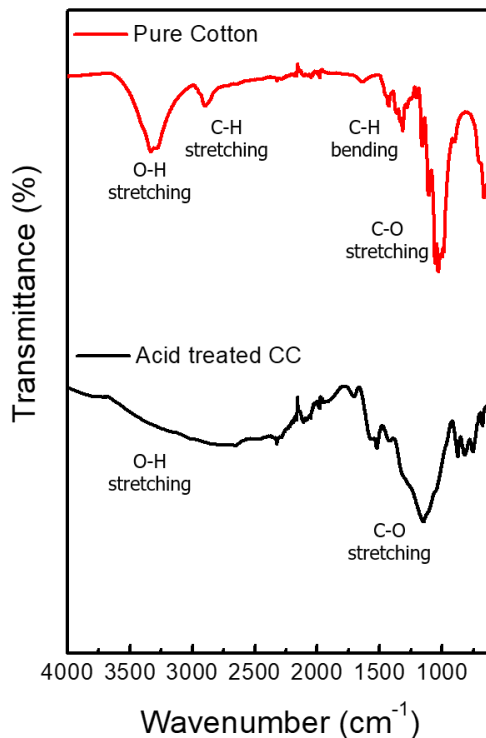


Figure 5.2. FT-IR spectra of pure cotton and acid treated CC

XPS characterization was performed to evaluate the extent of oxidation in the CC after acid treatment. Figure 5.3 displays the XPS data of the CC before and after the acid treatment. After the acid treatment, an increase in the atomic percentage of oxygen can be observed due to the addition of hydroxyl and carboxylic functional groups. Figure 5.3A represents the XPS survey spectra of CC before and after acid treatment. The two peaks at 285.0 and 532.0 eV correspond to the C 1s and O 1s respectively. An Auger peak is visible around 970 eV which is responsible for the transition from L to K shell of oxygen and it is denoted as O KLL in the survey spectra. The atomic percentage of oxygen before and after the acid treatment was calculated based on the peak areas of C and O 1s peaks. Oxygen atomic percentage was increased from 6.3% to 24.8% after refluxing in 50% HNO₃ for one hour. High-resolution spectra of C 1s before and after the oxidation is shown in Figure 5.3A and B respectively. The dominant peak at 284.8 eV corresponds to C-C

bond (diamond and graphitic type). A small amount of etheral carbon (C-O and O-C-O) was also observed even before the acid treatment which is probably coming from adventitious carbon deposited on the surface. After the acid treatment, a significant increase can be seen in C=O and O-C=O bonds (~287 and ~289 eV respectively) due to the addition of carbonyl and carboxylic functional groups.¹⁵³⁻¹⁵⁴ Addition of the above discussed polar functional groups effectively enhanced the hydrophilicity of the material which is vital in designing an efficient solar steam generation device.

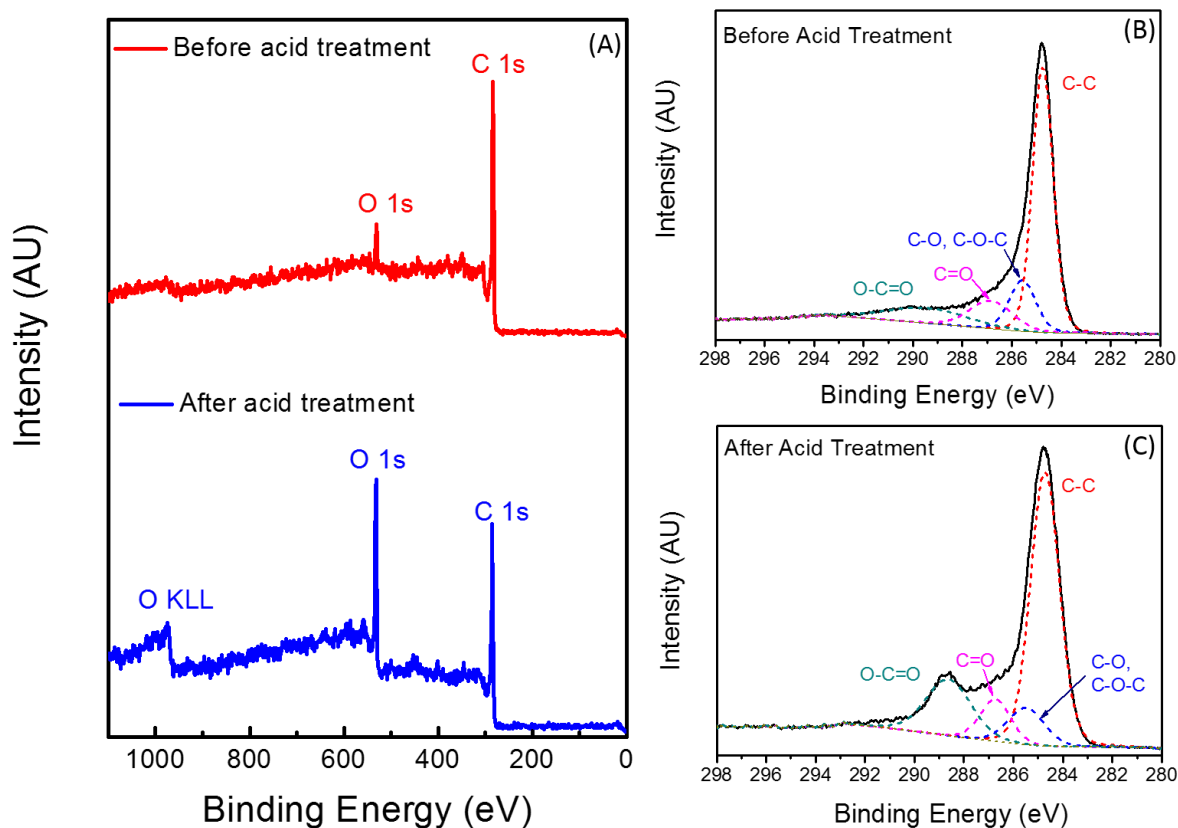


Figure 5.3. XPS survey spectra of CC before and after acid treatment (A), C 1s spectra of CC before (B) and after (C) acid treatment.

SEM images of the pure cotton fibers and CC is shown in Figure 5.4. As shown in Figure 5.4A and B the average diameter of pristine cotton fibers can range from 15 to 20 μm . However, after

carbonization at 600 °C for 1 hour, the average diameter was decreased by around 50%. Due to the release of H₂O, CO₂ and CO during the carbonization, the weight of the cotton was also decreased by ~70% after one hour.¹⁵⁵ Also, during the heat treatment, most of the fibers were cracked and opened probably due to the pressure build up from the evolved gases (Figure 5.4D).

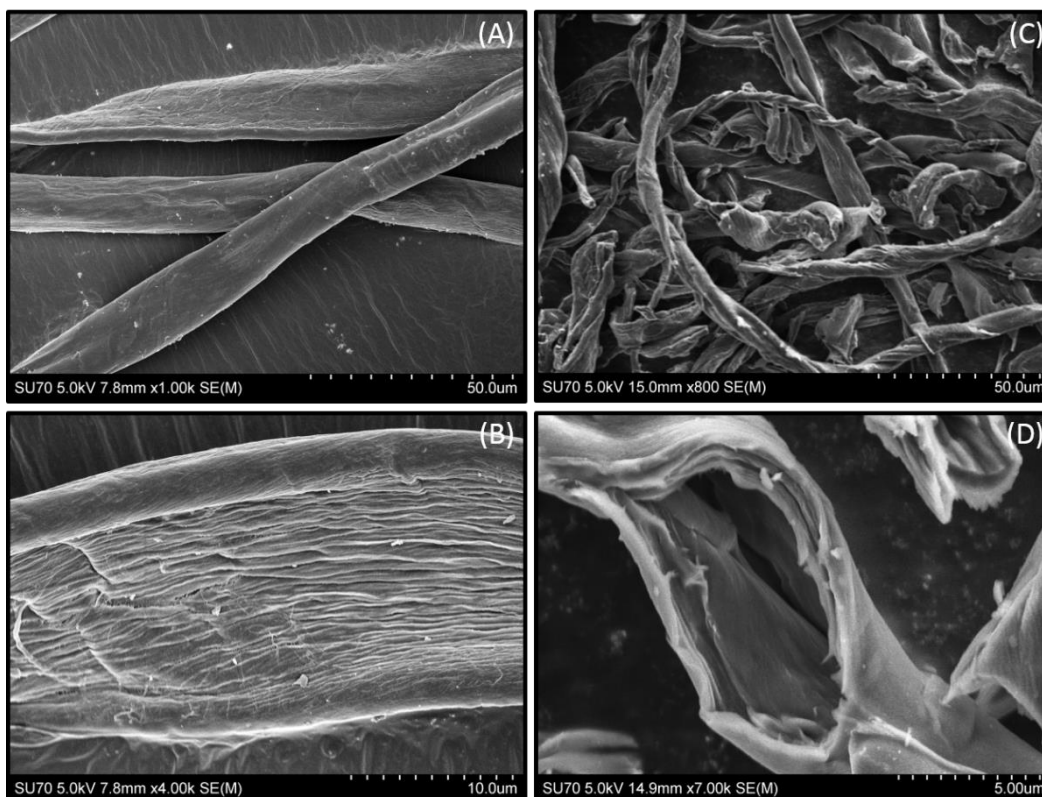


Figure 5.4. SEM images of PC fibers (A), (B) and CC (C), (D)

Raman spectrum of the CC is displayed in Figure 5.5. The two peaks in the spectrum can be ascribed to the D and G bands which are located around 1350 and 1590 cm⁻¹ respectively. The prominent G band ascertains that after carbonization at a higher temperature in an inert atmosphere (N₂), the cellulose fibers convert into sp² hybridized graphitic carbon.

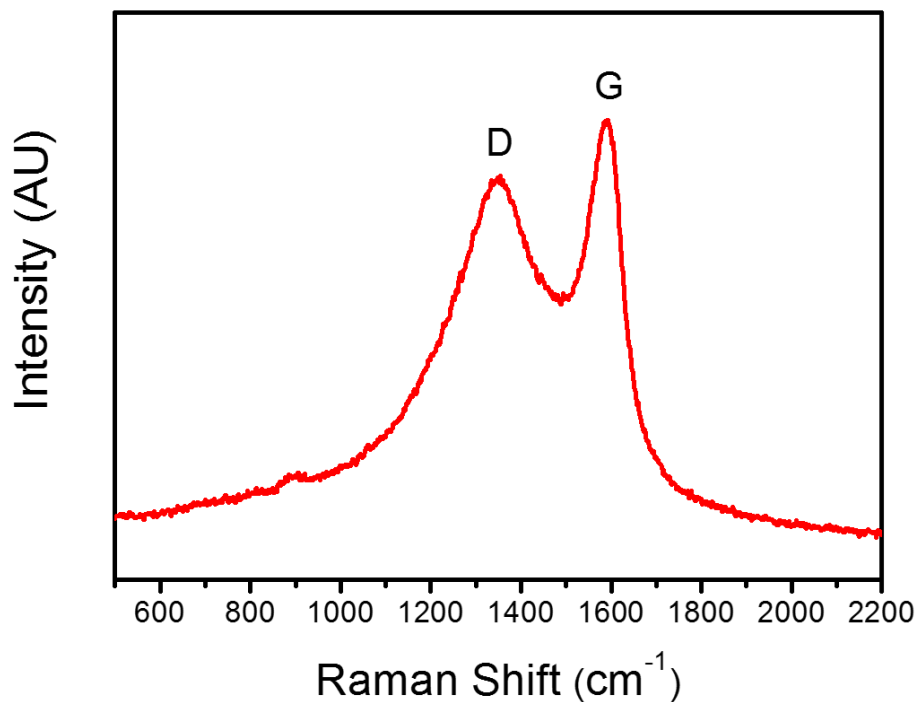


Figure 5.5. Raman spectrum of CC

Optical properties of the CC material are shown in Figure 5.6. CC exhibits low percentage of reflectance ascribed to its black color (Figure 5.6A). Moreover, the CC device possesses a strong absorption band covering the whole spectrum which is shown in Figure 5.6B. The percentage absorbance of the CC was above 70% in the entire visible range which is one of the key reasons to use carbonized materials as photothermal devices.^{37, 151, 156} However, the percentage absorbance drops by ~15% in the infra-red region which is not a significant impact since the solar irradiance in the region after 800 nm is below $\sim 0.6 \text{ Wm}^{-2} \text{ nm}^{-1}$.

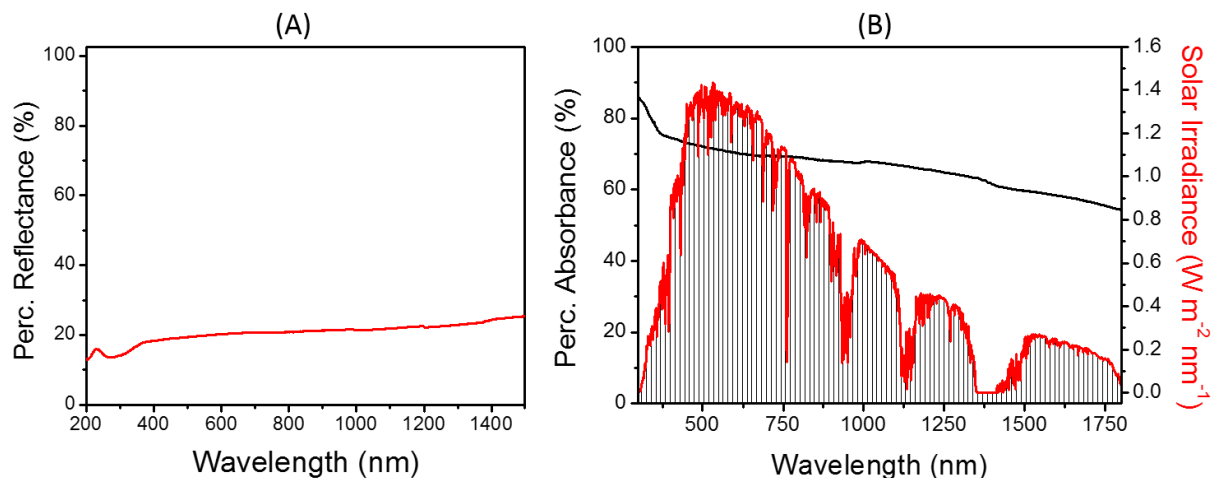


Figure 5.6. Optical properties of the CC material. (A), the reflectance spectrum of CC and (B), percentage absorbance of CC in comparison with.

To evaluate the performance of the CC solar steam generation device, the steam generation rates were measured at different solar intensities of 1 kW m⁻² (1 sun), 5 kW m⁻² (5 sun) and 8 kW m⁻² (8 sun). The solar steam generation rate of the CC device was compared with DI water and a similar device made of PC. The irradiation source used for this project is a Newport Sol2A, Class ABA solar simulator with a power of 450 W. Figure 5.7 represents the solar steam generation rates, solar-to-vapor efficiencies and surface temperature profiles of the CC, PC and DI water samples. Evidently, CC device exhibits high evaporation rates compared to PC device at all the solar intensities which are 0.93, 6.42 and 10.9 kg m⁻² h⁻¹ at solar intensities of 1, 5 and 8 sun respectively. Comparatively, the solar evaporation rate of PC device was as low as 0.44, 1.68 and 2.39 kg m⁻² h⁻¹ at the same solar intensities. The solar evaporation rate of the CC device at 8 sun is almost 5 times higher than the PC device mainly due to the high solar absorption of the CC compared to the PC device which reflects solar energy due to its inherent light-reflecting white color. However, the solar steam generation rate of PC is higher than that of DI water since the hydrophilic fibrous structure enhances the surface evaporation.

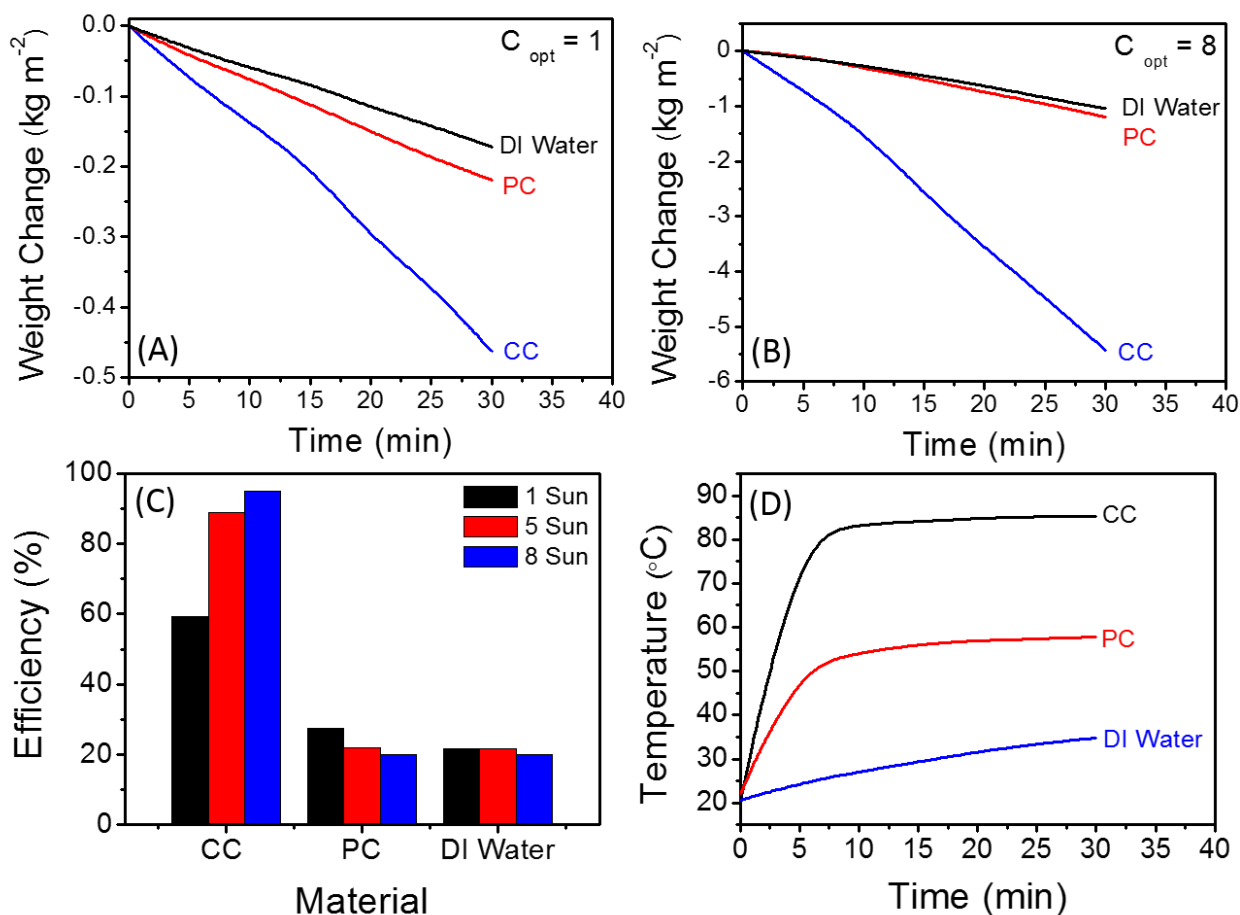


Figure 5.7. Solar steam generation data for CC, PC and DI water at solar intensities of (A), 1 kW m^{-2} (1 sun) and (B), 8 kW m^{-2} (8 sun). (C), The solar-to-vapor evaporation efficiency of CC, PC and DI water. (D), the Surface temperature profile of CC, PC and DI water at 8 sun.

The solar-to-vapor efficiency was calculated based on the equation 3.1 mentioned in chapter 3.^{30, 100, 125} As shown in Figure 5.7C, the CC device exhibits very high solar-to-vapor efficiency at 8 sun compared to other devices reported in the literature. At solar intensities of 1, 5 and 8 sun the calculated solar-to-vapor efficiencies of CC device are 59.2, 88.7 and 94.9% respectively.

The surface temperature profile of the CC device during the operation at 8 sun of solar intensity is plotted in Figure 5.7D. The temperature was increased from room temperature to 80 $^{\circ}\text{C}$ within 5 minutes and after 15 minutes it reached a steady state temperature of $\sim 85^{\circ}\text{C}$. However, the surface

temperature of the PC device only reached 51.1 °C after 5 minutes and its equilibrium temperature was only ~57 °C. Due to the special design of the CC device the heat loss to the bulk water is greatly minimized. At all the solar intensities the temperature increment in the bulk water was less than 1 °C. Conduction heat loss is considered one of the main contributors to energy loss in solar steam generation devices. Conduction heat loss can be quantified using Fourier's law where the conductive heat flux j is given by:

$$j = \kappa \frac{\Delta T}{L} \quad 5.1$$

where κ is the thermal conductivity of the cotton stalk ($0.026 \text{ W m}^{-1} \text{ K}^{-1}$)¹³⁵ and $\Delta T/L$ is the temperature gradient across the cotton stalk. In our CC device, the pure cotton stalk was about 5 cm in length and 0.8 cm in diameter. So the calculated conductive heat flux is around 6.3 W m^{-2} which is about 0.6% heat loss at 1 sun and even lower at 8 sun (~0.4%).¹⁵¹ Moreover, the frame of the CC solar steam generation device is made of polyethylene foam which has a low thermal conductivity ($\sim 0.04 \text{ W m}^{-1} \text{ K}^{-1}$)¹⁵⁷ and it helps to confine the heat within the irradiation area. In a previous study conducted by our group, in a case where the irradiation area is in direct contact with the bulk water the percentage conductive heat loss was as high as 2.2%¹³⁸ compared to 0.6% in the CC device. Thus, it is clear that the novel low-cost design of the CC solar steam generation device effectively reduces the heat loss to bulk water.

One of the applications of the CC device is to extract pure water from wastewater. Figure 5.8A displays the UV-Visible spectra of 10 ppm MB dye solution and the condensed water of the steam extracted from the dye solution under the solar intensity of 5 sun. This concept can also be used to desalinate seawater.^{112, 138} Figure 5.8B displays the recyclability data of the CC device during 10 steam generation cycles under the solar intensity of 5 sun. The average normalized steam

generation after 10 cycles was 3.24 kg m^{-2} and the standard deviation was 0.03 kg m^{-2} . Therefore, it is safe to mention that the CC material is highly stable and suitable for long term applications in solar steam generation and wastewater treatment applications.

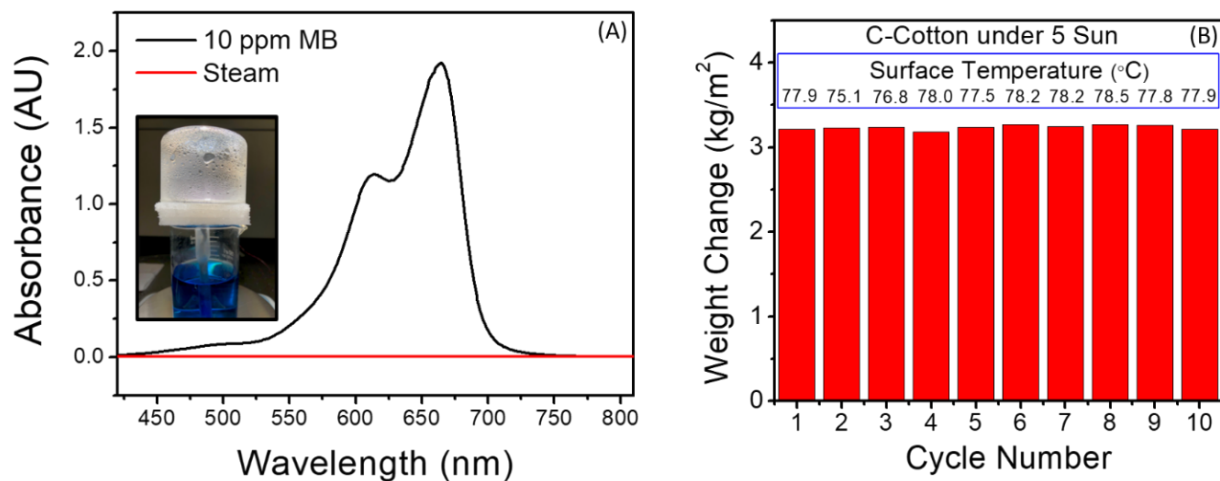


Figure 5.8. (A), UV visible spectra of 10 ppm MB dye solution and condensed steam sample, a photograph of the setup is shown in the inset and (B), Recyclability test of the CC device during 10 cycles of constant solar irradiation under the solar intensity of 5 sun.

5.4. Conclusions

In conclusion, our group has designed a novel device using carbonized cotton, pristine cotton and low-density polyethylene foam for efficient solar steam generation and wastewater treatment. The special design of this device minimized the area that contact with bulk water which efficiently minimized the conductive heat loss. The characteristic features such as durability, minimized conductive heat loss, and self-floating capability make CC device a perfect candidate for efficient solar steam generation and wastewater treatment. Moreover, the use of low-cost materials such as cotton makes it an economically viable device for energy-yielding applications such as SWD.

Chapter 06: Growth Mechanism of “Sea Urchin” ZnO Nanostructures and their Photocatalytic Activity for the Degradation of Organic Dyes

6.1. Introduction

In the world of binary semiconductors, ZnO has gained a substantial research interest due to its unique properties such as high exciton binding energy (60 meV), wide direct bandgap (3.37 eV) and high intrinsic electron mobility ($\sim 300 \text{ cm}^2 \text{ V}^{-1} \text{ s}^{-1}$). ZnO is naturally an n-type semiconductor mainly under Zn rich conditions due to the creation of shallow donor levels by interstitial Zn atoms.¹⁵⁸ It is also possible to obtain p-type ZnO by doping elements such as Al, Na and N.¹⁵⁹⁻¹⁶¹ It is one of the most widely studied semiconductors in the field due to its wide range of applications such as catalysis, sensors, optoelectronics, photovoltaics, batteries, room temperature UV lasers etc.¹⁶²⁻¹⁶⁷ Also properties of ZnO like biocompatibility, biosafety, low cost and stability under harsh conditions increased the range of its applications.¹⁶⁸⁻¹⁶⁹

In the past few decades, there has been a plethora of research efforts focused on the size and shape control of inorganic nanostructures mainly due to its significant effect on the physical properties of the material. Compared to 1D or 2D nanostructures such as rods, wires or disks, 3D nanostructures exhibit unique features such as low aggregation, high surface area and superior carrier mobility which can serve well in photocatalysis and sensing applications. However, it has been a challenge to obtain well defined 3D nanostructures with a proper understanding of the growth mechanism. Nevertheless, the recent advancements in techniques of nanomaterial synthesis, opened doors to successfully synthesize 3D nanostructures and unveil the mechanistic details of the crystal growth. Some of the examples that can be found in the literature include tetrapods,¹⁷⁰⁻¹⁷¹ hollow,¹⁷²⁻¹⁷³ non-hollow spheres,¹⁷⁴ corn-like,¹⁷⁵ nanopropellers,¹⁷⁶ branched^{177,}

and flower-like structures^{166, 178-181} which were synthesized using hydrothermal, template-assisted aging and chemical/solid vapor deposition techniques.

General approaches to obtain 3D architectures include the utilization of template directional growth¹⁸² or selective manipulation of growth rates of specific crystal facets using organic surfactants^{178, 183-184}. However, the utilization of templates and organic surfactants can cause complications due to the contaminations and can cause adverse effects on the properties of the material. However, surfactant and template-free synthetic routes to obtain hierarchical 3D structure can also be found in the literature. For example, Hu et al. developed a hydrothermal route where a zinc amino complex is autoclaved at 180 °C for 12 hours to obtain sea urchin-like 3D architecture for gas sensing applications.¹⁸⁵ In another work, Zhu et al. utilized a mixture of concentrated KOH and $\text{Zn}(\text{NO}_3)_2 \cdot 6\text{H}_2\text{O}$ solutions and a room temperature autoclave technique to obtain a similar shape which was then loaded with Au NPs for photodegradation of rhodamine b.¹⁶⁶ However, a detailed mechanistic understanding of the growth of these nanostructures can be limited by the growth technique. For instance, it can be problematic to track the sequential growth of a nanostructure during hydrothermal synthesis.

With the rapid development in the fields like agriculture and production industry, wastewater has become a major environmental concern in the modern world. According to a World Bank estimation, 17-20% of the contributors to water pollution are related to the textile industry. Annual production of textile dyes is close to a million tons and about 15% of it is generally released to the environment with minimal or no treatments.¹⁸⁶ Therefore, the photodegradation of organic dyes is one of the most important and widely studied branches of photocatalysis. Moreover, it has the advantages of utilizing costless, inexhaustible and clean solar energy.³⁰ ZnO is a proven candidate which can be utilized as a cost-effective tool for pollution control due to the unique chemical and

physical properties mentioned earlier. In this chapter, a simple two-step aqueous phase synthetic route to obtain sea SU shaped ZnO 3D nanostructures is explained along with a proposed mechanism for the sequential development of the SU shape. Moreover, the photocatalytic performance of the SU ZnO in comparison with ZnO rods is discussed.

6.2. Materials and Methods

6.2.1. Materials

Zinc acetate (Alfa Aesar), zinc nitrate hexahydrate (Sigma-Aldrich) potassium hydroxide (Sigma), ethanol (Alfa), hexamethylenetetramine (Sigma), methylene blue (Sigma), rhodamine b (Alfa), indigo carmine (Sigma)

6.2.2. Preparation of ‘Sea Urchin’ Shaped ZnO Nanorod Clusters

As the first step of the sequential growth of SU shaped ZnO nanorod clusters, ZnO seeds were prepared as a colloidal suspension in ethanol according to a method found in the literature.¹⁸⁷ Initially, a solution of 2 mM Zn(Ac)₂ solution in ethanol was heat-treated at 70 °C for 30 minutes in a water bath. Then, a solution of 4 mM KOH solution in ethanol was added dropwise. The molar ratio between Zn(Ac)₂ and KOH was maintained at 1:1. Afterward, the temperature of the solution was reduced to 60 °C and continued heating for one hour with constant stirring. The formation of the ZnO seeds can be confirmed visually by observing the cloudiness of the reaction solution

To synthesize SU shaped ZnO nanorod clusters, a conventional aqueous phase growth process was utilized. First, an equimolar aqueous solution of 20 mM Zn(NO₃)₂·6H₂O and HTA was used as the growth solution. First, 25.0 mL of the pre-synthesized ZnO seed solution and 100.0 mL of the growth solution were mixed together and sonicated for 15 minutes to homogeneously disperse the seeds in the growth solution. Then, the mixture was incubated in a water bath at 90 °C for 1 hour

without stirring. Finally, the nanorod clusters were formed and separated from the growth solution and washed several times with DI water and ethanol to get rid of the unreacted components. The resultant white powder was then oven dried at 70 °C overnight.

6.2.3. Characterization of Materials

Prepared SU ZnO nanorod clusters were characterized using the following techniques. TEM and SEM images were obtained using Jeol JEM-1230 TEM with the Gatan Orius SC1000 side mount CCD camera at 120 kV and Hitachi SU-70 FE-SEM respectively. UV-visible spectra were obtained using an HP-8453 spectrophotometer. PXRD patterns were acquired with the PANalytical MPD X'Pert Pro with a copper filter ($\text{Cu } \alpha, \lambda = 1.5405 \text{ \AA}$) at 45 kV and 40 mA with a scan speed of $0.5^\circ \text{ } 2\theta/\text{min}$. Raman spectra were obtained from Thermo Scientific DXR SmartRaman (532 nm). Micromeritics 3Flex™ surface and catalyst characterization analyzer was used for the surface area measurements. Samples were activated overnight at 100 °C to degas. Then, nitrogen adsorption-desorption isotherms were obtained at 77 K to determine the BET surface area.

6.2.4. Photocatalytic Experiments

Photocatalytic activities of the SU ZnO samples were evaluated based on the photodegradation efficiency of three common organic dyes, MB, Rh B and IC. The photodegradation experiment is briefly introduced as follows. A 4 W, 365 nm UV lamp was used as the source of irradiation, and a Petri dish (diameter of 3.5 inches) was used as the reaction container. The UV lamp was placed about 10 cm above the Petri dish. Before the experiment, 50 mL of aqueous solutions were prepared to contain dispersed ZnO (0.25 mg/mL) and the desired dye (10 ppm) and then added into the container. Afterward, the solutions were kept in dark for one hour to achieve adsorption-desorption equilibrium. Finally, the lamp was turned on and samples were withdrawn at different

intervals to analyze the concentration variation of the dyes. The photodegradation efficiencies were calculated based on the UV-visible absorption of each aliquot.

6.3. Results and Discussion

6.3.1. Material Characterization

Electron microscopic images of the ZnO seeds are shown in Figure 6.1. By the appearance of the ZnO seeds under the TEM (Figure 6.1A and B), it is clear that they are clusters of small seeds. These small seeds in the size range of 4-6 nm were then aggregated to form spherical seed clusters which are around 80 nm in size as shown in the SEM images in Figure 6.1C to D.

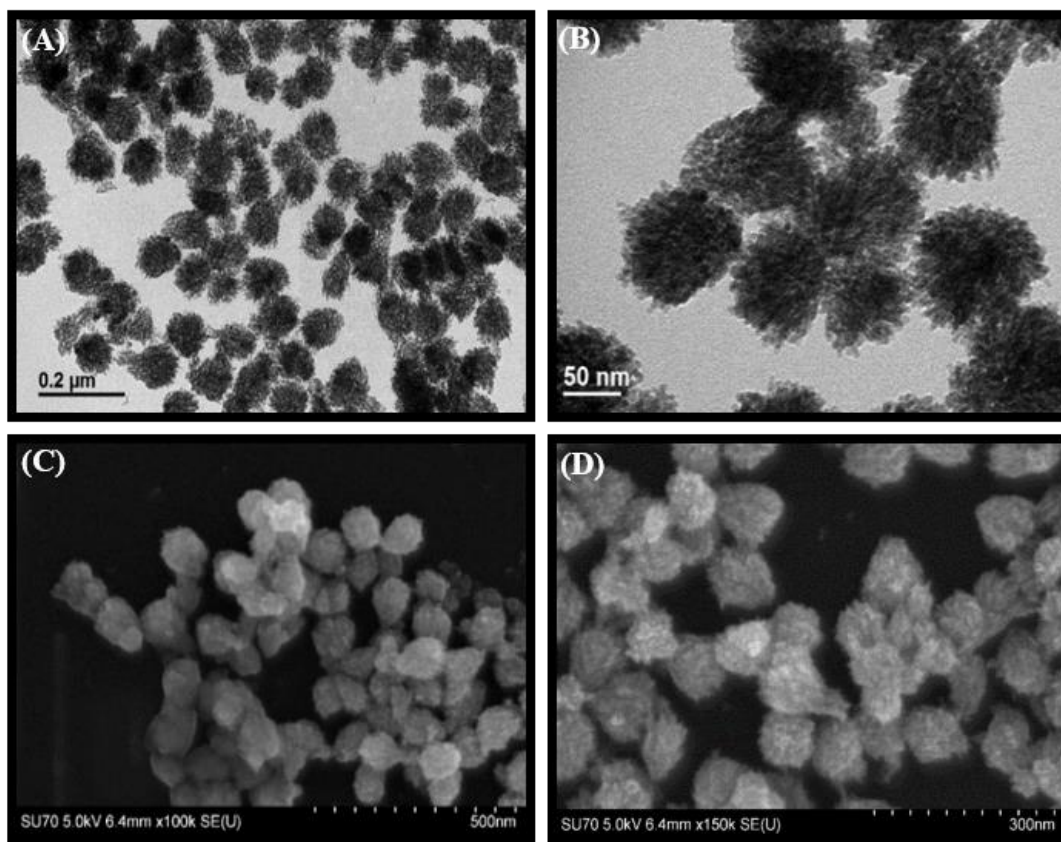


Figure 6.1. TEM and SEM images of ZnO seeds (a, b and c, d respectively)

To understand the formation mechanism of ZnO seeds, a mechanistic study was done by obtaining TEM images at different stages of the reaction. For that, samples were carefully withdrawn from the solution at different time intervals (5, 15, 30, 60 mins). The TEM images of those samples are shown in Figure 6.2A-D. Upon adding the base, cloudiness was observed after about 5 minutes indicating the formation of ZnO seeds (Figure 6.2A). Due to the absence of a capping agent in the solution, seeds were started to aggregate under constant heating at 60 °C (Seen in Figure 6.2B, and C), forming the seed aggregates in the size range of 80-100 nm (Figure 6.2D). Also, the UV-visible spectra shown in Figure 6.2E indicates a red shift in the absorption edge from 334 nm (3.71 eV) to 350 nm (3.54 eV) indicating the decrease in bandgap due to the increasing particle size. These seed clusters are stable as a suspension in ethanol as confirmed by TEM images taken after being suspended in ethanol up to a week. Aggregation of the seeds into seed clusters can be explained using Ostwald ripening where individual ZnO seeds aggregate together to reduce the surface to volume ratio. The main hypothesis of this project is that ZnO seed clusters are the key reason for the unique ‘sea urchin’ shape.

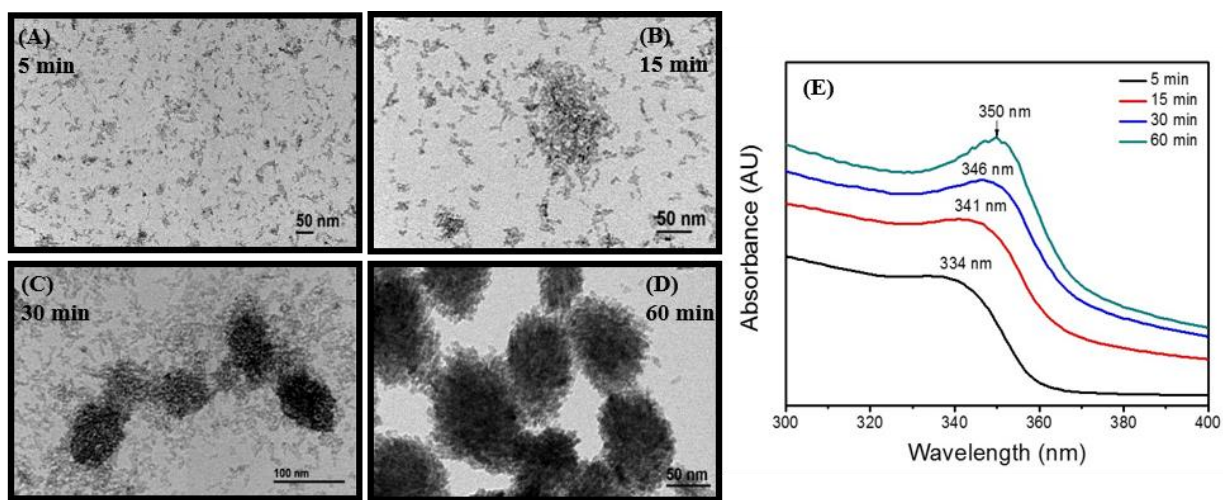


Figure 6.2. TEM images of ZnO seeds obtained at different time intervals, 5 minutes (A), 15 minutes (B), 30 minutes (C), 60 minutes (D) and respective UV-Vis spectra (E).

To test this hypothesis, CTAB was added as a capping agent to prevent the seeds from aggregating. As expected, seeds were remained separated after one hour of heat treatment at 60 °C (Figure 6.3). Without CTAB, the absorption edge of the ZnO seeds was increased up to 350 nm after an hour of heating. However, in the presence of CTAB, the absorption edge of the seeds was increased only up to 336 nm (Figure 6.3E) indicating minimal aggregation and small particle size of the seeds.

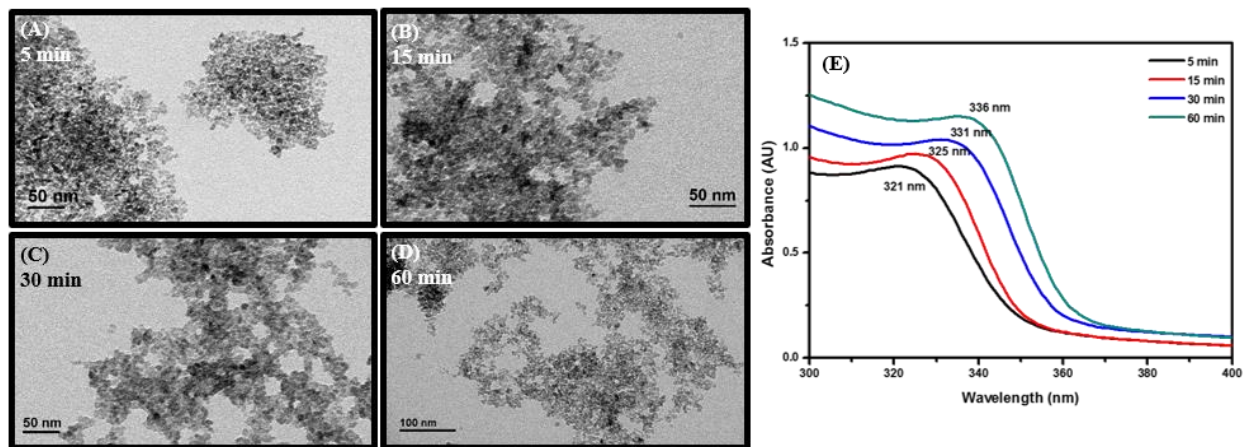


Figure 6.3. TEM images showing the sequential growth of ZnO seeds in the presence of CTAB at different time intervals, 5 minutes (A), 15 minutes (B), 30 minutes (C), 60 minutes (D) and respective UV-Vis spectra (E).

Both CTAB passivated and naked seeds were incubated at 90 °C in a solution containing $\text{Zn}(\text{NO}_3)_2 \cdot 6\text{H}_2\text{O}$ and HTA. During the thermal hydrolysis of HTA, NH_3 is slowly released to the solution which will then react with water to form $\text{NH}_4(\text{OH})$.¹⁸⁸ As the solution becomes basic, Zn^{2+} ions react with OH^- ions which will yield ZnO (equations 6.1-6.2). These steps are seemingly fast because the solution became cloudy as the temperature reaches $\sim 70^\circ\text{C}$ indicating the formation of $\text{Zn}(\text{OH})_2$. In the case of uncapped ZnO seed clusters, this will result in a growth of ZnO rods along the [0001] direction in a way that all the rods are concentric to the core of the seed cluster yielding the sea urchin-like shape (Figure 6.4A and B). The size distribution of the ZnO clusters is ranging

from 0.5 μm to 1.5 μm most likely due to the stagnant growth in the absence of stirring. However, CTAB capped seeds were individually grown into separate rods supporting our hypothesis. The diameter of the rods about 20 nm in both structures (seen in Figure 6.5).

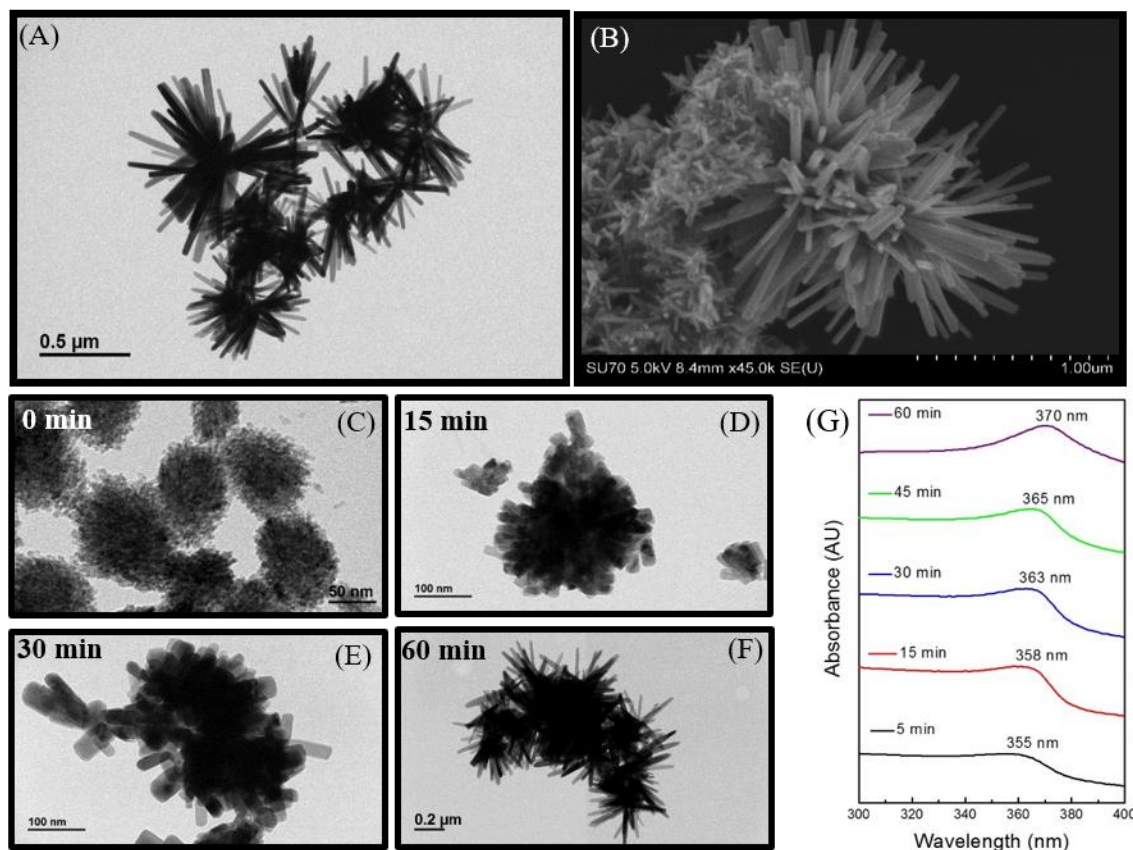


Figure 6.4. TEM image (A) and SEM image (B) of SU ZnO nanorod clusters, TEM images showing the sequential growth of SU ZnO at different stages, 0 min (C), 15 min (D), 30 min (E), 60 min (F) and UV/vis spectra of the SU ZnO at different growth time intervals (G).



Due to the polar nature of the ZnO lattice structure, the surface is either negatively or positively charged. That will depend on the termination of the crystal plane whereas Zn terminated planes

will be positively charged and O terminated planes will be negatively charged. Depending on the charge, the surface will attract counterions in the medium (OH^- or Zn^{2+}) and form a layer of charges on the surface. The new charged layer will attract opposite charges which will consequently react with each other to form ZnO.¹⁸⁸ This sequence will continue to form an ordered ZnO lattice in [0001] direction until the concentration of the precursor ions in the solution depletes. Each seed in the seed clusters has the potential to grow into a rod and Figure 6.4C-F show the sequential growth of the SU ZnO structure at different stages of the synthesis. ZnO seeds have an absorption edge at 350 nm as shown in Figure 6.2E, but after the growth for 1 hour, the absorption edge was red-shifted to 370 nm as shown in Figure 6.4G, indicating a decrease in the bandgap energy. It was proven that the magnitude of the bandgap is inversely proportional to the semiconductor particle size which can also be explained using the band theory. Valence band and conduction band are simply molecular orbitals which are overlapped together forming a continuum. When the particle size is small, a number of molecular orbitals that form the bands get lower hence increasing the bandgap size. In the case of bulk materials, defects create inconsistency near the band edge making the bandgap narrower.¹⁸⁹ However, increased particle size can negatively impact on the photocatalytic performance due to the low surface area.

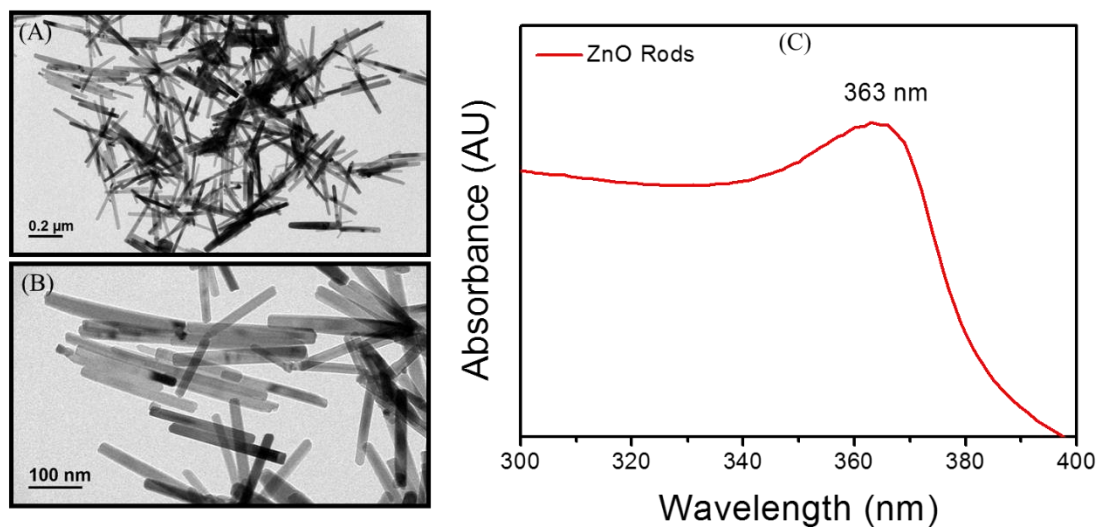


Figure 6.5. TEM images of ZnO rods synthesized with CTAB capped ZnO seeds (A, B) and the UV-Vis spectrum (C).

Figure 6.6A represents the XRD patterns of SU ZnO and seeds of ZnO. According to the XRD pattern, the crystal system of the ZnO clusters belongs to the hexagonal wurtzite structure bearing the space group P63mc. ZnO seeds (Figure 6.6B) show broader XRD peaks compared to the SU ZnO due to the smaller particle size. The peak intensity of the (002) plane is relatively small in the seeds. However, as the seeds are grown to SU ZnO, the relative peak intensity of the (002) plane is increased which proves that the (002) plane has the highest activity during the crystal growth. This observation further confirms the suggested mechanism for crystal growth.

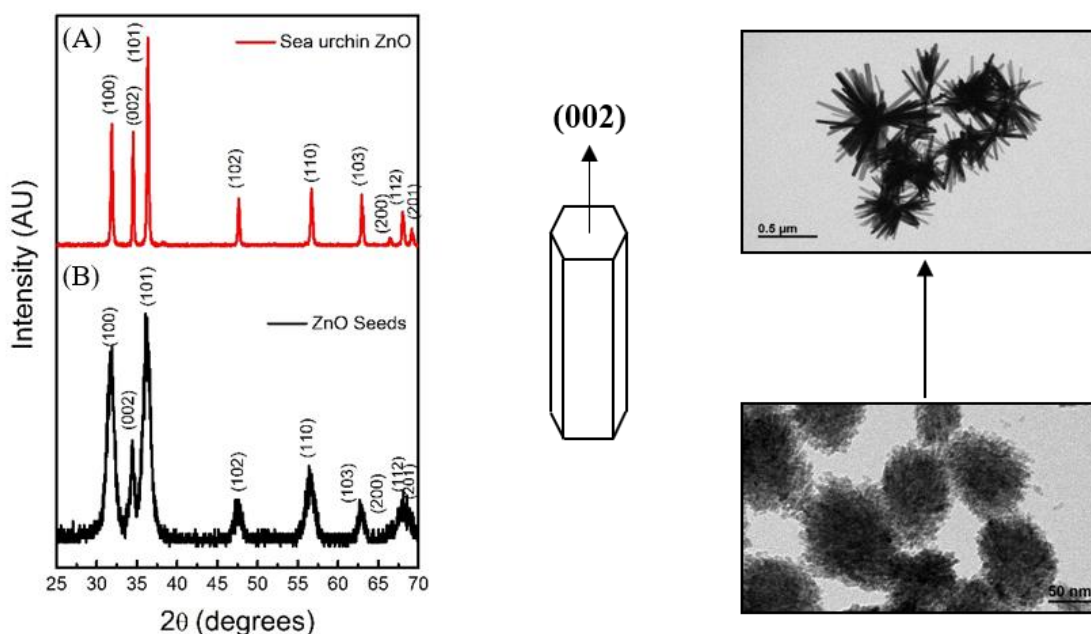


Figure 6.6. XRD patterns of SU ZnO (A), ZnO seeds (B) and TEM images showing how the seeds transformed into SU shaped ZnO.

To confirm the hexagonal wurtzite structure of ZnO clusters, Raman spectra of SU ZnO and ZnO rods were determined and shown in Figure 6.7. It is shown that the Raman spectrum obtained for solid ZnO sample consisted of peaks at 332, 378, 437 and 580 cm^{-1} respectively. The prominent peak at 437 cm^{-1} corresponds to the non-polar E_2 (high) optical phonon mode. Peaks at 378 and 580 cm^{-1} are attributed to the polar transverse optical (TO) A_1 and longitudinal optical (LO) E_1 phonon modes, respectively. The peak at 332 cm^{-1} corresponds to $2E_2$ mode. According to the selection rules, Raman active phonon resonance modes for the ZnO wurtzite structure are $A_1+2E_2+E_2$.¹⁹⁰ Therefore, it further confirms that the SU ZnO clusters have the hexagonal wurtzite crystal structure.

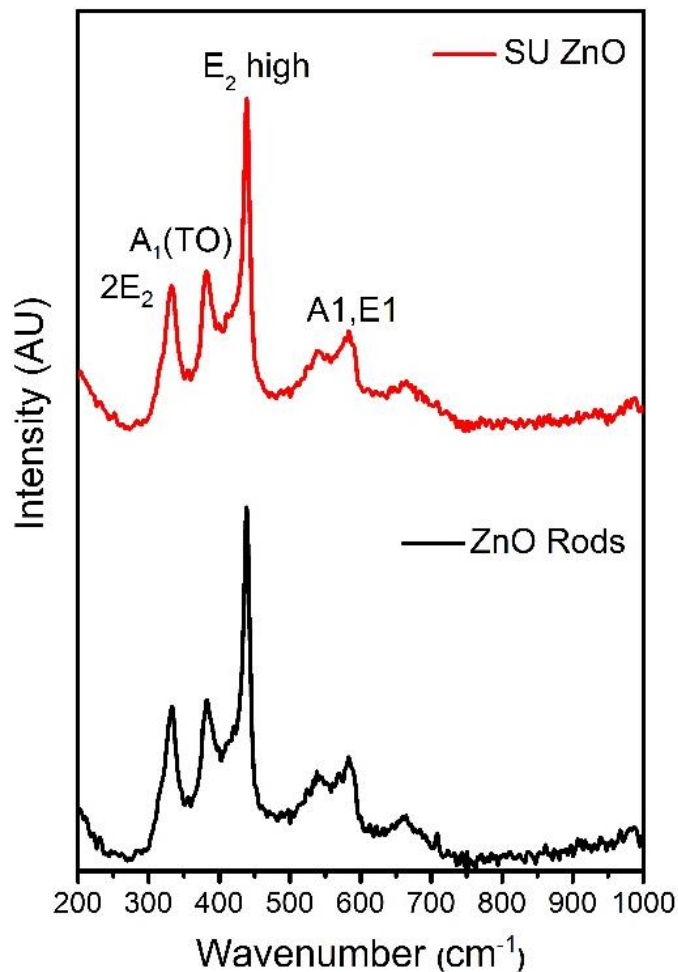


Figure 6.7. Raman spectra for SU ZnO and ZnO rods.

6.3.2. Photocatalytic Activity of ZnO Nanorods and SU ZnO Nanorod Clusters

The photocatalytic performance of SU ZnO was evaluated based on the photodegradation efficiency of organic dyes IC, MB and Rh B under UV irradiation. The results were shown in Figure 6.8. Figure 6.8A-C represent the UV-visible spectra of Rh B, IC and MB during the photodegradation experiment. The removal percentages of Rh B, IC and MB reached 96, 99 and 86% after UV irradiation for one hour, respectively. The photodegradation reactions for all the three dyes follow pseudo-first-order kinetics (Figure 6.8D), and the degradation of IC shows the fastest kinetics among all having a rate constant of 0.076 min^{-1} .

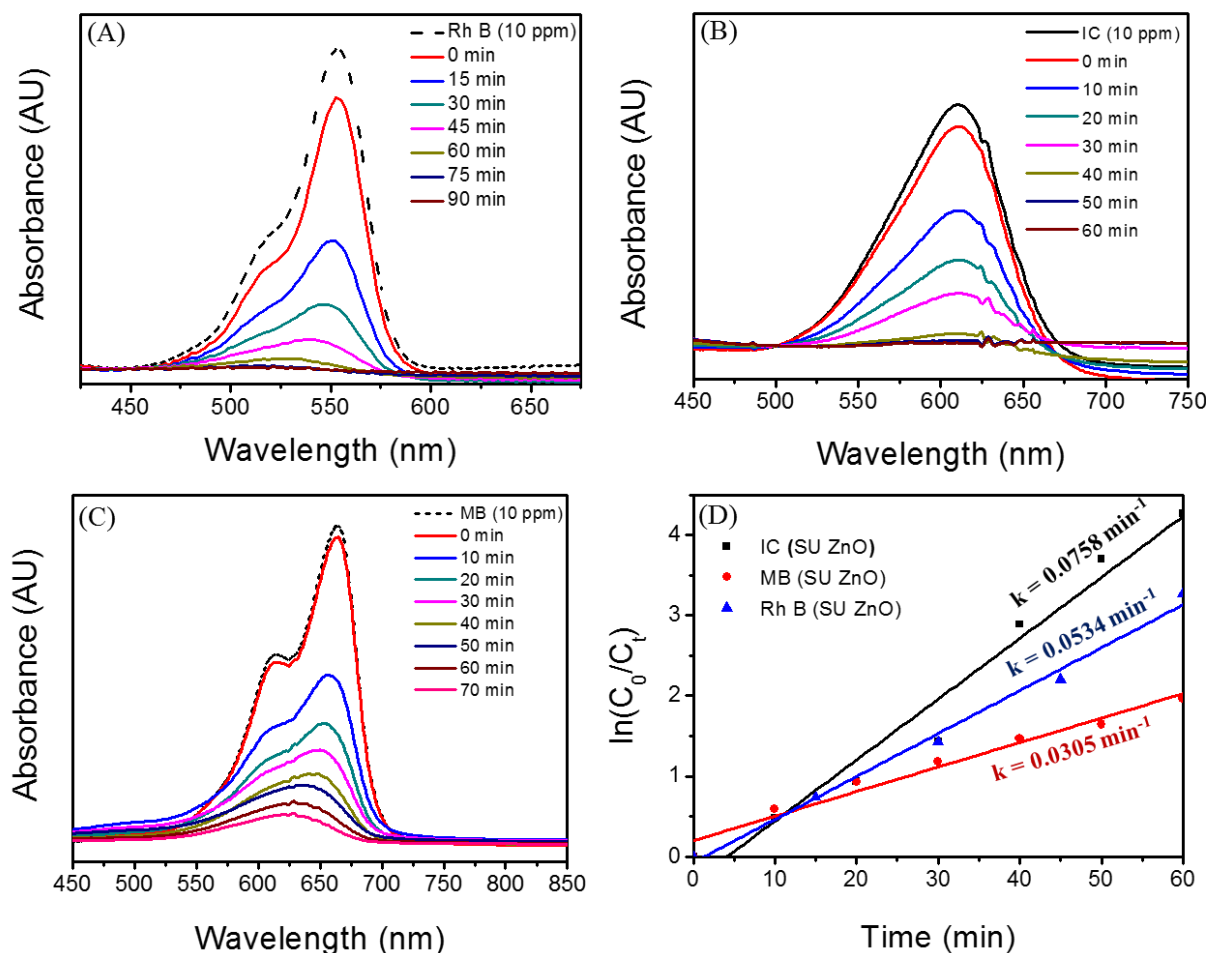


Figure 6.8. Photocatalytic activity of SU ZnO in degrading organic dyes (A) Rh B, (B) IC, (C) MB and (D) the apparent rate constants for the photodegradation of Rh B, IC and MB.

According to data, MB exhibits a slight resistance to photodegradation compared to other two dyes. MB is the only anionic dye among the three dyes and ZnO surfaces can possess a slightly negative charge while submerging in aqueous solutions due to the surface hydrolysis¹⁹¹. On account of the electrostatic repulsion, MB showed a little drop in the absorption edge after the initial adsorption-desorption equilibrium for one hour which is evident at 0 min mark of Figure 6.8C. Weak chemical adsorption of MB could shorten its retention time on the surface of the SU ZnO catalyst that brings a negative effect on its photodegradation. However, a clear drop in the absorption edges was observed for Rh B and IC after the initial dark reaction as shown in Figure

6.8A and B and a rapid photodegradation also happened within one-hour irradiation, which must be related to its strong chemical adsorption on the catalyst surface.

Finally, the photocatalytic activities of SU ZnO and ZnO rods in photodegrading Rh B were compared. As shown in Figure 6.9A and B, the photocatalytic activity of ZnO rods is weak compared to SU ZnO. It is also noticeable that after the initial dark adsorption, SU ZnO exhibited considerable adsorption of the dye compared to the rods. After one hour of UV irradiation, ZnO rods only degraded 34% of the dye (10 ppm) whereas SU ZnO degraded 96%. Figure 6.9D shows the kinetic plot of the degradation reaction. Per BET surface area measurements, SU ZnO catalyst possesses a specific surface area of $26.94 \text{ m}^2/\text{g}$ which is acceptable considering the size and shape of the SU particles.¹⁹²⁻¹⁹³ ZnO rods, on the contrary, possess a surface area of $17.68 \text{ m}^2/\text{g}$. Thus, it is possible that comparatively high surface area of SU ZnO can be a key reason for its significantly high photocatalytic activity.

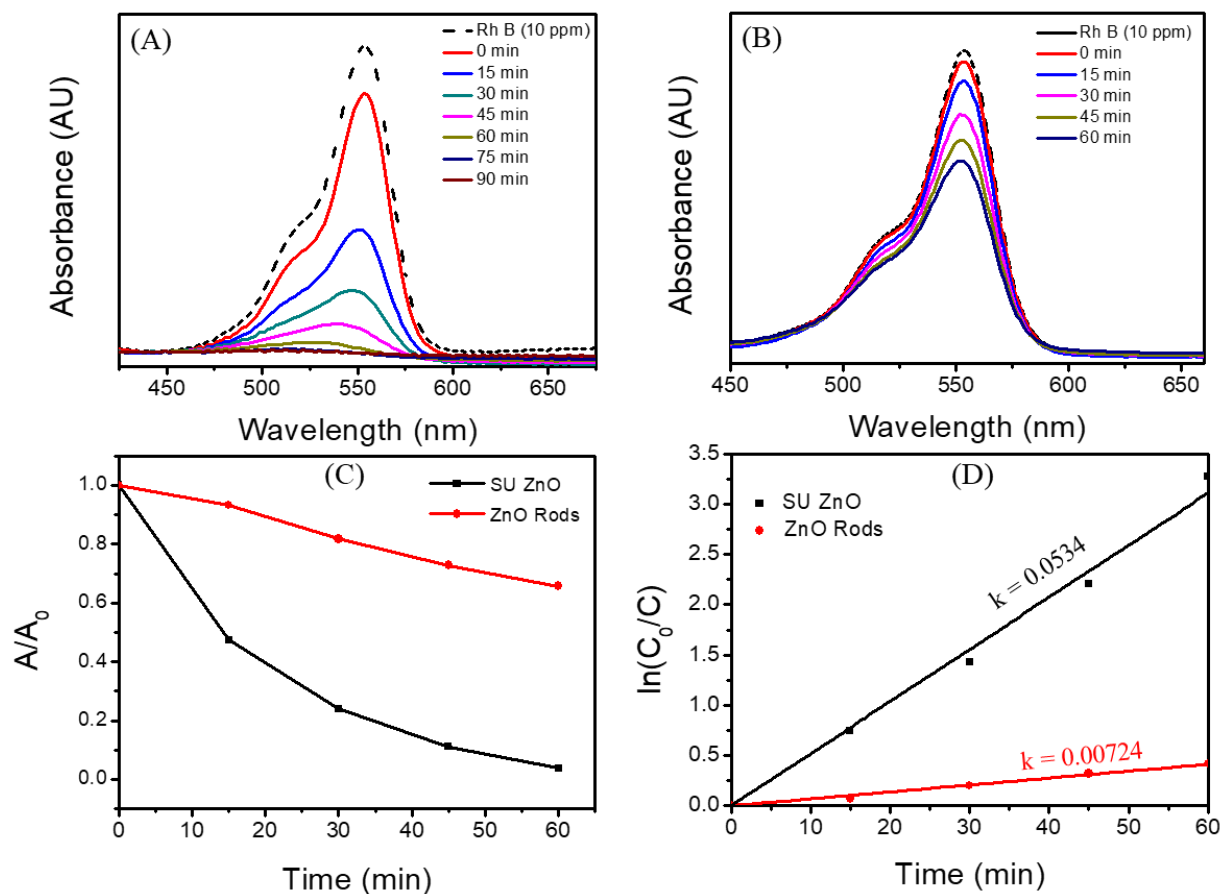


Figure 6.9. Comparison of photocatalytic activities of SU ZnO and ZnO rods prepared using CTAB capped ZnO seeds in photodegrading Rh B. (A and B) UV-visible spectra of Rh B showing photodegradation by SU ZnO and ZnO rods respectively and (C and D) kinetic plots of the photodegradation reaction by SU ZnO and ZnO rods respectively.

6.4. Conclusions

In conclusion, in this study, the preparation and growth mechanism of SU shaped ZnO 3D nanostructures were studied. As evident from the TEM images, the key step behind the SU shape is the aggregation of ZnO seeds into small clusters that subsequently grew into a cluster of rods. When the seeds were kept separated using a surfactant CTAB, 3D structures were not formed. These unique 3D architectures possess a hexagonal wurtzite crystal structure in the size range of 0.5-1.5 μm and a specific surface area of 26.94 m^2/g . The high photocatalytic activity of the

material was assessed by the photodegradation efficiency of three organic dyes, MB, IC and Rh B in aqueous solutions. Weak chemical adsorption of anionic MB on the catalyst surface brought a slightly negative effect on its photodegradation but still achieved 86% of removal efficiency after one hour of UV irradiation. Therefore, SU ZnO shows the potential to be a versatile catalyst in photodegrading industrial wastewater containing organic dyes.

Chapter 07: Iron Carbide and Aminated Graphene Oxide Composite for Chromium Removal in Wastewater

7.1. Introduction

Over the past few decades, magnetic NPs gained significant attention due to their potential for data storage,¹⁹⁴⁻¹⁹⁵ drug delivery,¹⁹⁶⁻¹⁹⁷ biomedical imaging,¹⁹⁶⁻¹⁹⁸ catalysis,¹⁹⁹⁻²⁰² magnetic sensors²⁰³ and spintronics.²⁰⁴ Particularly, iron carbide has extensively been used to cover a wide range of applications such as MRI contrast agent,²⁰⁵⁻²⁰⁸ cancer therapy²⁰⁹⁻²¹¹ and Fischer-Tropsch synthesis.²¹²⁻²¹⁵ Iron carbide materials possess high mechanical strength and chemical stability compared to pure iron due to the presence of carbon atoms in its matrix. Primarily, these carbon atoms reside in the interstices of the closed packed iron atoms giving rise to two main classes of iron carbides depending on the type of interstice where carbon atoms are located. In some types of iron carbides, the carbon atoms are present in trigonal-prismatic interstices (Fe_3C , Fe_5C_2 , and Fe_7C_3) whereas in the other, carbon atoms are located in octahedral interstices ($\text{Fe}_{2.2}\text{C}$ and Fe_2C).²⁰⁰ For this project, Hägg iron carbide (Fe_5C_2) NPs were synthesized using the well-known hot injection technique with the shape control simply by changing the ratio between two capping agents, OAm and OAc.

Rapid industrialization is considered as one of the key reasons for water-related issues. Among these issues, the release of wastewater containing toxic heavy metals (Cr, Hg, Cd, As, and Pb) is considered as one of the biggest concerns. Out of these heavy metals, Cr(VI) is considered as one of the common contaminants in wastewater due to its wide use in industrial operations such as tanning, smelting, electroplating, and mining.²¹⁶ Cr(VI) is known to cause adverse health effects ranging from skin diseases (superficial irritation, subdermal ulceration) to several types of cancers.²¹⁷⁻²¹⁸ Therefore, Cr(VI) removal from wastewater has been a widely studied area in the

past few decades. Current removal techniques involve ion exchange,²¹⁹⁻²²⁰ reverse osmosis,²²¹⁻²²² electrochemical precipitation,²²³⁻²²⁵ adsorption,²²⁶⁻²³¹ etc. However, some of these techniques can be disadvantageous due to the associated cost and poor performance at low concentrations. Adsorption is by far the most economical and simplest technique available for heavy metal removal. However, recycling and regeneration of the adsorbents can sometimes be challenging depending on the nature of the material and the conditions of the wastewater. To overcome the challenges associated with the separation of the material after use, magnetic composite adsorbents can be utilized due to the ease of extraction using a magnet.²³²⁻²³⁴ Iron oxide is commonly used to prepare composites with adsorbents such as activated carbon, GO, biomass-derived materials and certain polymers.²³³⁻²³⁶

In this study, a composite material that consists of amine functionalized GO (adsorbent) and Fe₅C₂ NPs (magnetic material) is prepared for efficient removal of Cr(VI). Among the carbon-based adsorbents, GO has gained significant attention due to its good dispersion in water, biocompatibility, ability to be functionalized and relatively easy preparation.²³⁷⁻²³⁹ GO contains polar functional groups such as hydroxyl, epoxy and carboxylic which are responsible for the hydrophilic nature of the material. Moreover, the oxygen atoms of these functional groups can donate its lone pair electrons to the vacant orbitals of the transition metal ions forming metal complexes which is beneficial for the removal applications.^{238, 240-241} However, according to the theory of hard and soft acids and bases, these functional groups may not be very effective in removing certain heavy metals. Never the less, these oxygen-containing functional groups can be used to introduce strong chelating agents such as amines and thiols through functionalization for enhanced removal of heavy metals.²⁴¹

7.2. Materials and Methods

7.2.1. Materials

Iron pentacarbonyl (99.99%, Sigma-Aldrich), oleylamine (99%, Aldrich), oleic acid (70%, Aldrich), cetyltrimethylammonium bromide (95%, Aldrich), potassium dichromate (Fischer), hexane (Sigma), ethanol (Fischer), graphite powder (99.5%, Alfa), concentrated sulfuric acid (99%, Alfa), phosphoric acid (99%, Alfa), potassium permanganate (Alfa), hydrogen peroxide (30%, Sigma), thionyl chloride (99% Sigma), triethylamine (99.5%, Sigma-Aldrich), ethylenediamine (99%, Sigma), chloroacetic acid (99%, Sigma-Aldrich), potassium dichromate (99%, J.T. Baker), dimethylformamide (>99%, Sigma)

7.2.2. Material Preparation

7.2.2.1. Synthesis of Rod-Shaped and Polygonal Iron Carbide

To synthesize rod and cube shapes of Fe_5C_2 NPs, a well-known hot-injection approach was utilized.²⁰⁰ In a typical procedure, OAm was used as both solvent and surfactant. CTAB was used as inducing agent and $\text{Fe}(\text{CO})_5$ as the precursor. In a four-neck flask, a mixture of 25 mL of OAm (52.7 mmol) and 0.113 g (0.307 mmol) of CTAB was stirred sufficiently and degassed under a flow of N_2 for 30 minutes. The mixture was heated to 120 °C, and then 0.5 mL of $\text{Fe}(\text{CO})_5$ (3.6 mmol) was injected under a blanket of nitrogen gas. Then, the temperature was ramped up to 350 °C and kept at this temperature for 10 minutes. The orange color of $\text{Fe}(\text{CO})_5$ was changed to black, indicating the decomposition of $\text{Fe}(\text{CO})_5$ and the nucleation of Fe nanocrystals. Afterward, the solution was cooled down to room temperature. The product was then washed with ethanol and hexane and collected for further characterization. To synthesize polygons and heart like shapes of Fe_5C_2 NPs, a similar procedure was performed. In which, 1.25 mL (3.6 mmol) of OAc was added

to 25 mL (52.7 mmol) of OAm and. The as-prepared NPs were kept in a vacuum desiccator to avoid exposure to air before further characterization.

7.2.2.2. Synthesis of Iron Carbide-IGO-NH₂ Composite

Preparation of IGO-NH₂ involves three steps: synthesis of GO, the introduction of acyl chloride functionality and then reacting with ethylene diamine. First, improved GO was synthesized according to a method found in the literature.²⁴² A 9:1 mixture of concentrated H₂SO₄/H₃PO₄ (540:60 mL) was added to a mixture of graphite flakes (4.5 g) and KMnO₄ (27.0 g) and maintained below 30°C using an ice bath. The reaction was then heated to 50°C and stirred for 12 hours. The reaction was cooled to room temperature and poured onto ice (600 mL) containing 30% H₂O₂ (4.5 mL). Then, the mixture was centrifuged, and the remaining solid material was washed in succession with 200 mL of DI water, 200 mL of 30% HNO₃, and 200 mL of 2% ethanol. The IGO was then vacuum dried overnight at 60 °C.

To prepare IGO-Cl, 0.5 g of IGO was dispersed well in 10 mL anhydrous DMF by sonication for 1 hour and then treated with SOCl₂ (75mL) at 80°C for 3 days. The product was separated by centrifugation, washed with anhydrous DMF and dried under vacuum. Finally, ethylenediamine functionalized IGO was prepared by dispersing 0.5 g of IGO-Cl in 15 mL of anhydrous DMF. Then, 75 mL of ethylene diamine and 2 mL of triethylamine were added to the dispersion and refluxed at 80 °C for 48 hours. Finally, the reaction mixture was cooled down to room temperature, filtered and washed with a mixture of ethanol and water (1:1) several times. Product was then oven dried at 70 C for 10 hours.

7.2.2.3. Synthesis of Iron Carbide- IGO-NH₂ Composite

To synthesize Fe₅C₂-IGO-NH₂ Composite, 5 mg of IGO-NH₂ and 0.113 g of CTAB was added to 25 mL of OAm and ultrasonicated for 1 hour. Then, the dispersion was included in a three-neck flask and degassed under a continuous N₂ flow for 30 minutes. Then the temperature of the mixture was increased to 120 °C, and then 0.5 mL of Fe(CO)₅ was injected under an N₂ blanket. Then, the temperature was ramped to 350 °C and maintained at 350 °C for 10 min. Later, the mixture was kept there for 10 min before it was cooled to room temperature.

7.2.3. Characterization

Prepared Fe₅C₂ rods, polygons and Fe₅C₂-IGO-NH₂ composite were characterized using the following techniques. TEM and SEM images were obtained using Jeol JEM-1230 TEM with the Gatan Orius SC1000 side mount CCD camera at 120 kV and Hitachi SU-70 FE-SEM respectively. PXRD patterns were acquired with the PANalytical MPD X'Pert Pro with a copper filter (Cu K α , λ = 1.5405 Å) at 45 kV and 40 mA with a scan speed of 0.5° 2 θ /min. Raman spectra were obtained from Thermo Scientific DXR SmartRaman (532 nm). Magnetic properties of the materials were acquired by VersaLab™ 3 Tesla, Cryogen-free Physical Property Measurement System.

7.2.4. Cr (VI) Removal Experiments

7.2.4.1. Preparation of Cr(VI) Stock Solution

A stock solution of Cr(VI) containing 0.1 g of Cr in 1 L was prepared by dissolving 0.2828 g of K₂Cr₂O₇ in DI water and filling up to the mark of 1 L in a volumetric flask. Chromium solutions of lower concentrations were prepared by further dilution with DI water.

7.2.4.2. Batch Equilibrium and Kinetic Studies

Adsorption experiments were carried out by adding a fixed amount of Fe₅C₂, IGO-NH₂ and Fe₅C₂-IGO-NH₂ nanocomposite (5 mg) to a series of 20 mL vials containing 5 mL aqueous solutions of Cr(VI) with different concentrations. The concentration range was 0.5 – 25 ppm for iron carbide NPs and 10 – 250 ppm for IGO-NH₂ and Fe₅C₂-IGO-NH₂ nanocomposite. The initial pH values of the solution were 2 for (Fe₅C₂ NPs and IGO-NH₂) and 3 for (Fe₅C₂-IGO-NH₂ nanocomposite). The vials were then sealed and placed on a magnetic stirrer for desired time periods at 298 K. The vials were then removed from the magnetic stirrer and the adsorbents were separated from the solutions using a magnet and the final concentration of Cr(VI) in the solution was analyzed using ICP-OES. The percentage extraction of Cr(VI), %E and the amount of Cr(VI) adsorbed at equilibrium, q_e (mg/g) were calculated using equations 7.1. and 7.2 respectively.

$$\% \text{ Extraction} = \frac{(C_0 - C_e)}{C_0} \times 100\% \quad 7.1$$

$$q_e = \frac{(C_0 - C_e)V}{m} \quad 7.2$$

where C_0 and C_e are the initial and equilibrium concentrations of Cr (VI) in mg/L respectively, q_e is the adsorption capacity at the equilibrium in mg/g, V is the volume of the solution in L and m is the weight of the adsorbent used in g. Batch kinetic studies were conducted for Fe₅C₂, IGO-NH₂ and Fe₅C₂-IGO-NH₂ with Cr(VI) concentrations of 22, 50 and 100 ppm respectively. The aqueous samples were withdrawn at predetermined time intervals and the concentrations of Cr(VI) were measured using ICP-OES. The amount adsorbed at time t , q_t (mg/g), was calculated using equation 7.2.

7.2.4.3. Effect of pH and Adsorbent Dose

To evaluate the effect of pH on the Cr(VI) adsorption, 5 mg of the adsorbent was dispersed in 5 mL solutions containing 22 ppm of Cr(VI) for Fe₅C₂ and 25 ppm for IGO-NH₂ and Fe₅C₂-IGO-NH₂ nanocomposite. Initial pH values of the solutions were adjusted ranging from 1 to 8 using 0.01 M NaOH and HNO₃.

The effect of adsorbent dose on Cr(VI) removal was tested by adding different doses of adsorbents (0.005 g-0.030 g) to 10 mL of Cr(VI) solutions containing 10, 50, 100 ppm for Fe₅C₂, Fe₅C₂-IGO-NH₂ and IGO-NH₂ respectively. The solutions were stirred for 5 hours at the optimum pH values for each adsorbent (2 for Fe₅C₂ and 3 for Fe₅C₂-IGO-NH₂ and IGO-NH₂).

7.3. Results and Discussion

7.3.1. Material Characterization

The morphology of the synthesized Fe₅C₂ and Fe₅C₂-IGO-NH₂ nanocomposites were observed using TEM. Figure 7.1 shows the TEM images of Fe₅C₂ NPs which were synthesized using OAm as the solvent as well as the surfactant. As shown in the TEM images, the resultant Fe₅C₂ NPs are predominantly rod and cubic shaped when OAm is used as the solvent/surfactant. Despite the broad size distribution, the utility of OAm exclusively may have induced the growth of the Fe₅C₂ NPs in a selective direction. The size range of the Fe₅C₂ NPs is between 40-50 nm and the particle width of the rods is around 16 nm with an aspect ratio up to 10. Cube shaped NPs are also observed in the size range of 20-50 nm.

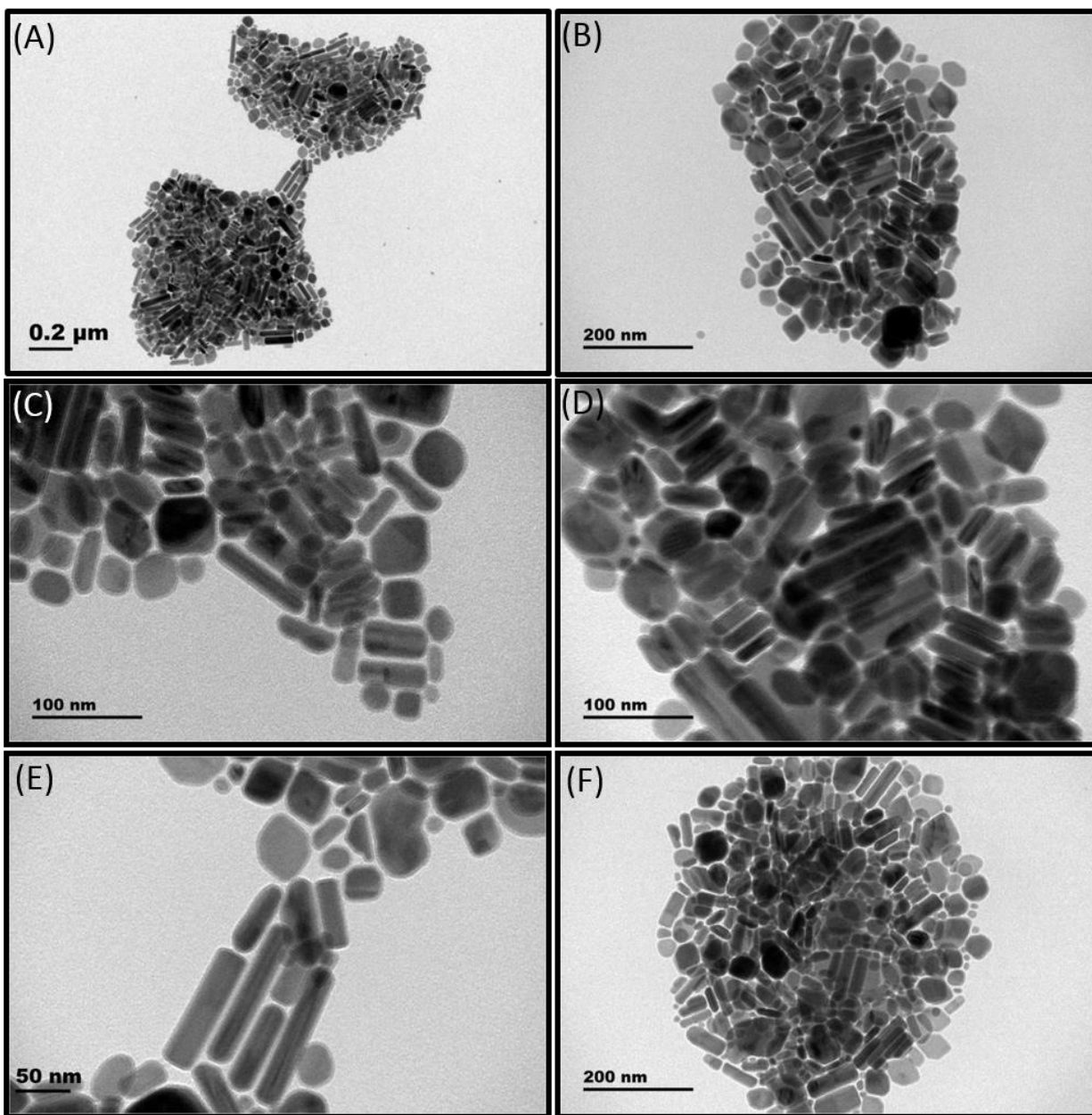


Figure 7.1. TEM images of Fe_5C_2 NPs synthesized using OAm.

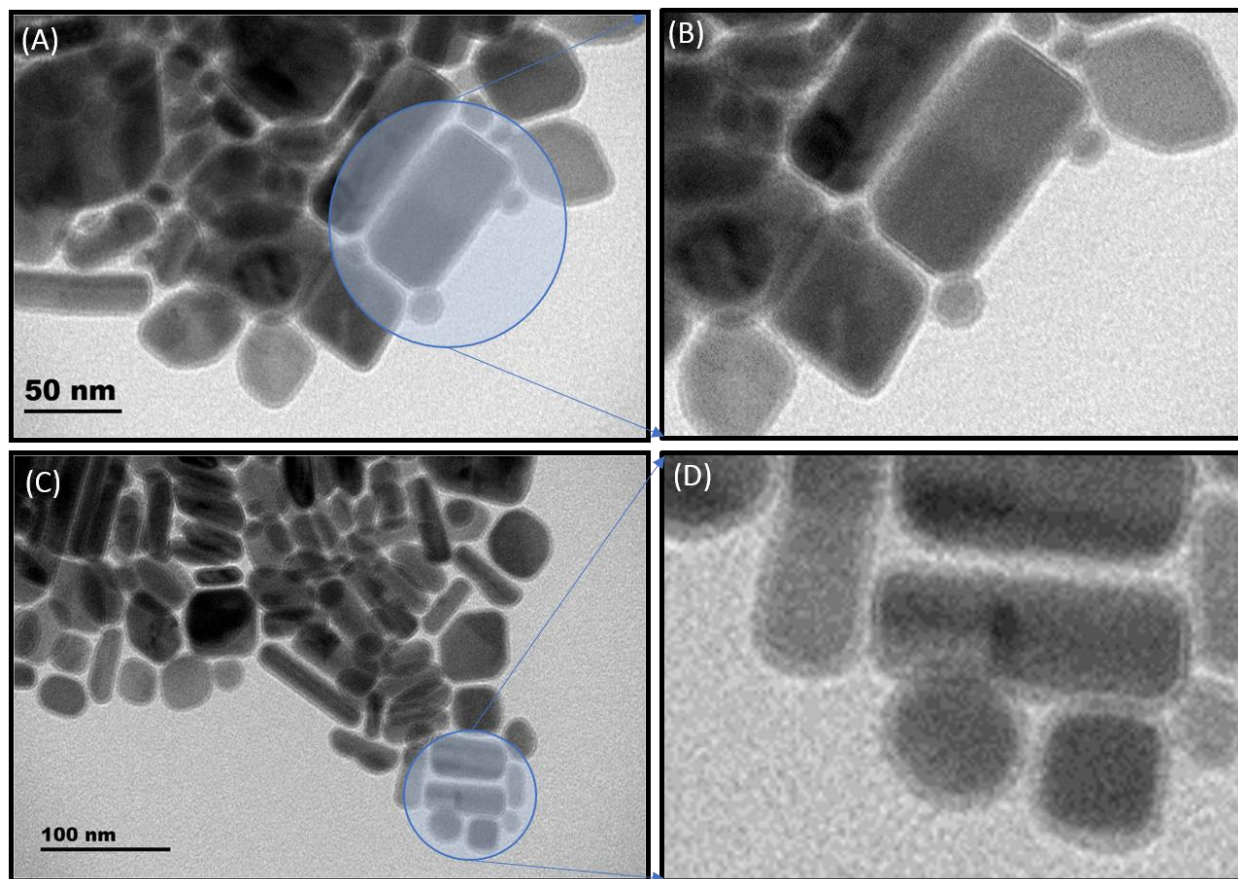


Figure 7.2. Magnified TEM images of the Fe_5C_2 rods indicating the carbon shell

Figure 7.2B and D shows the magnified images of Fe_5C_2 rods. An amorphous thin layer of carbon with a thickness of about 3 nm can be observed around the Fe_5C_2 NPs. To study the growth mechanism of the Fe_5C_2 nanostructures synthesized in the presence of OAm as the surfactant, TEM images of the samples which were withdrawn from the reaction mixture at different stages were obtained. After the hot injection of Fe precursor at 120 °C, the temperature was increased to 180 °C. Figure 7.3A shows a TEM image of the Fe NPs once the temperature of the solution reached 180 °C. The orange color of the $\text{Fe}(\text{CO})_5$ was disappeared and turned into black as the temperature of the solution gradually increased up to 180 °C indicating the formation of Fe NPs in the size range of 2-3 nm. When the temperature is reached up to 350 °C, the particle size was increased to the size range of 10-12 nm (Figure 7.3B and C). A thin carbon shell can also be observed which is

about 2 nm thick. Figure 7.3D represents the TEM image of the sample withdrawn after the solution was maintained at 350 °C. A wide shape and size distribution was observed after the heat treatment yielding rods, cubes, and some spherical shaped Fe₅C₂ NPs. However, the majority of the shapes were observed to be rods. A clear amorphous carbon shell could be observed in all the shape with the same thickness as of NPs shown in Figure 7.3B and C. The presence of small spherical NPs after the heat treatment at 350 °C suggests that the formation of large NPs occurs through Ostwald ripening by diffusion of small NPs through the carbon shell.

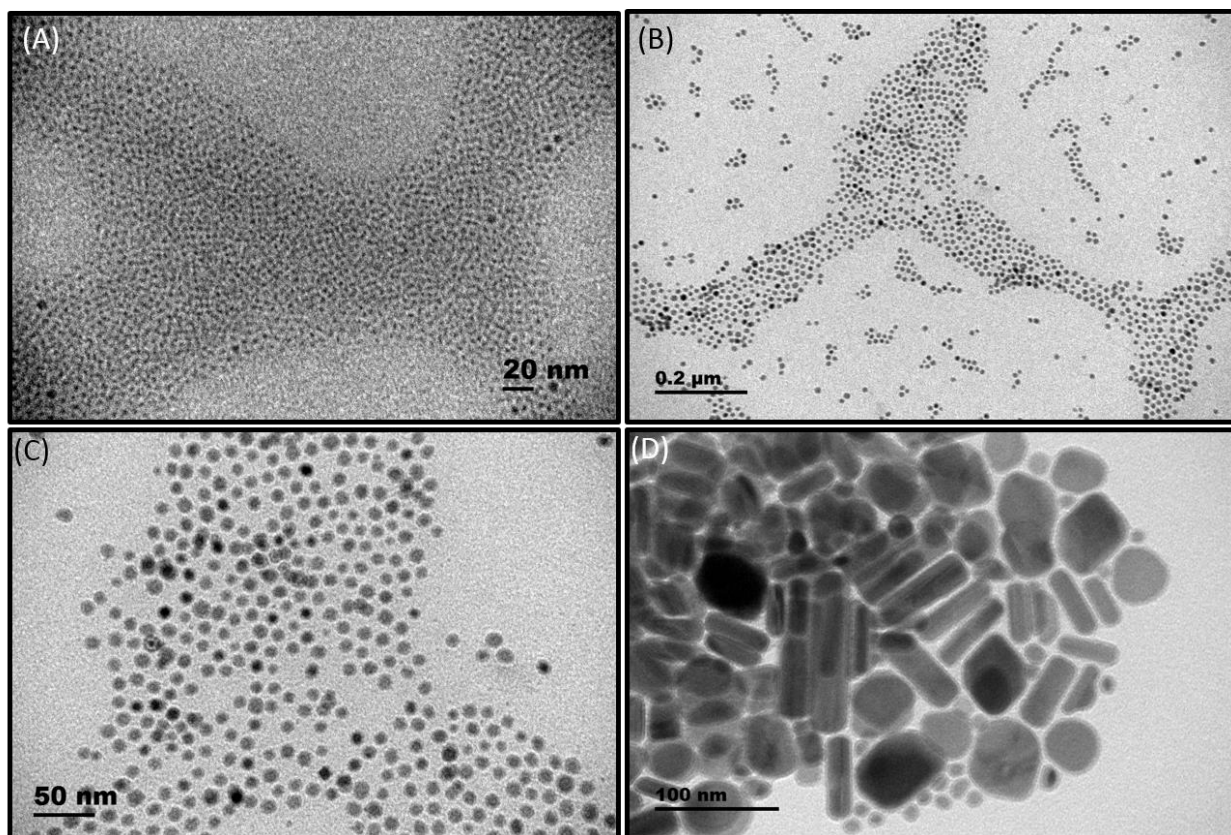


Figure 7.3. TEM images of the Fe₅C₂ NPs obtained at different stages of the reaction. (A), after reaching 180 °C, (B) and (C), After reaching 350 °C and (D), 20 minutes after reaching 350 °C.

To evaluate the effect of the ratio of surfactants on the morphology of the Fe₅C₂, OAc was introduced to OAm in the early stage of the experiment. It is important to mention that Fe₅C₂ was

not formed in the presence of pure OAc. It is known that CTAB induced the formation of Fe NPs which potentially catalyzed a dehydration reaction that converted OAm to nitriles. These nitrile groups then undergo C-C bond cleavage which provides the C source for Fe_5C_2 .²⁰⁰ Therefore, it was not possible to obtain Fe_5C_2 using OAc exclusively.

Figure 7.4 shows the TEM images of Fe_5C_2 NPs synthesized under OAm to OAc molar ratio of 7:2. As expected, OAc has changed the morphology of the Fe_5C_2 NPs significantly probably by passivating certain growth planes over the others. At the molar ratio of 7:2, heart-shaped and rice shaped NPs are observed. When the OAm to OAc molar ratio was changed to 14:1, Polygonal shapes were observed with a relatively uniform size distribution compared to the Fe_5C_2 samples synthesized using pure OAm and OAm to OAc ratio of 7:2. Therefore, it is safe to deduce that by changing the OAm to OAc ratio, the size and shape of the Fe_5C_2 NPs can be manipulated. However, under this molar ratio, the carbon shell which was clearly visible around the Fe_5C_2 rods was not observed under the TEM.

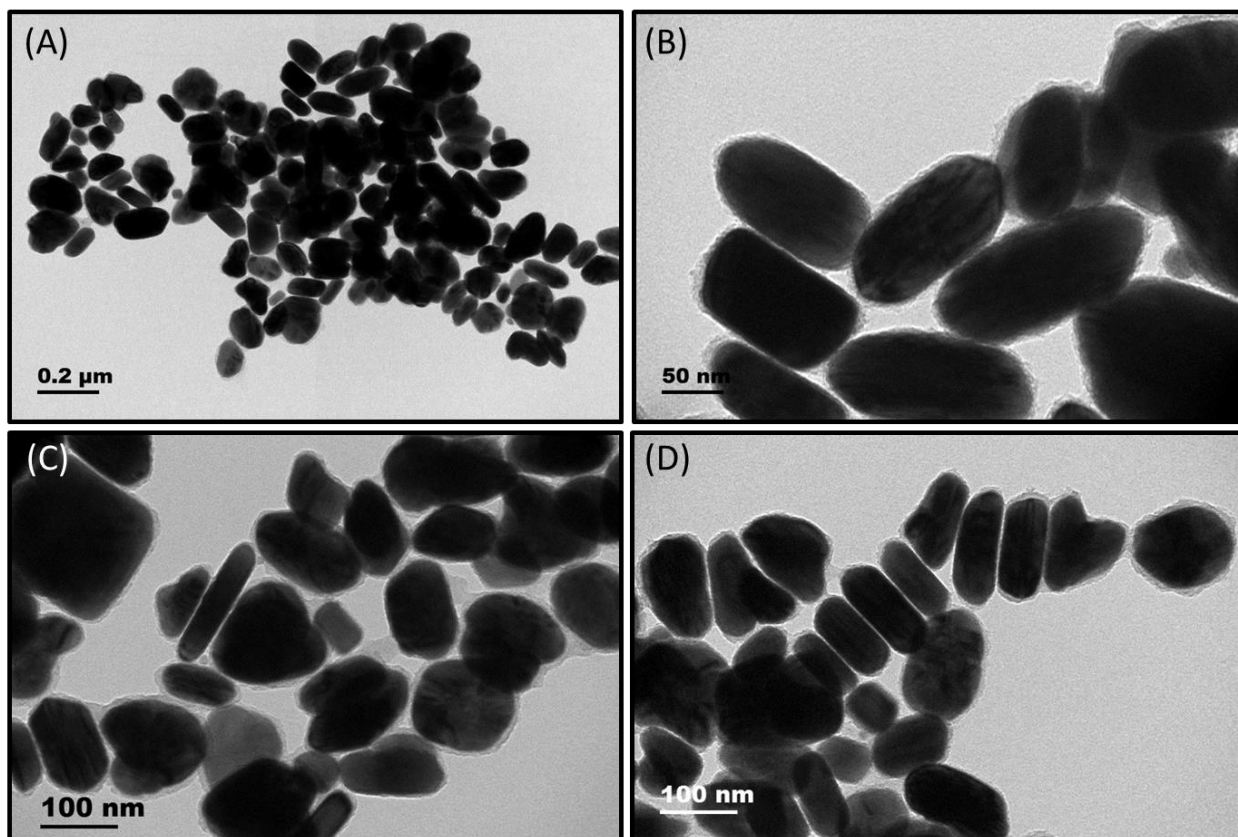


Figure 7.4. TEM images of Fe_5C_2 NPs synthesized using OAm to OAc molar ratio of 7:2

Figure 7.5 represents the TEM images of Fe_5C_2 NPs synthesized under OAm to OAc molar ratio of 14:1. When the ratio between OAm and OAc was increased up to 14 to 1, most of the Fe_5C_2 NPs were polygonal in shape. Also, the NPs were narrow in size distribution compared to the NPs obtained using pure OAm and OAm to OAc ratio of 7:2.

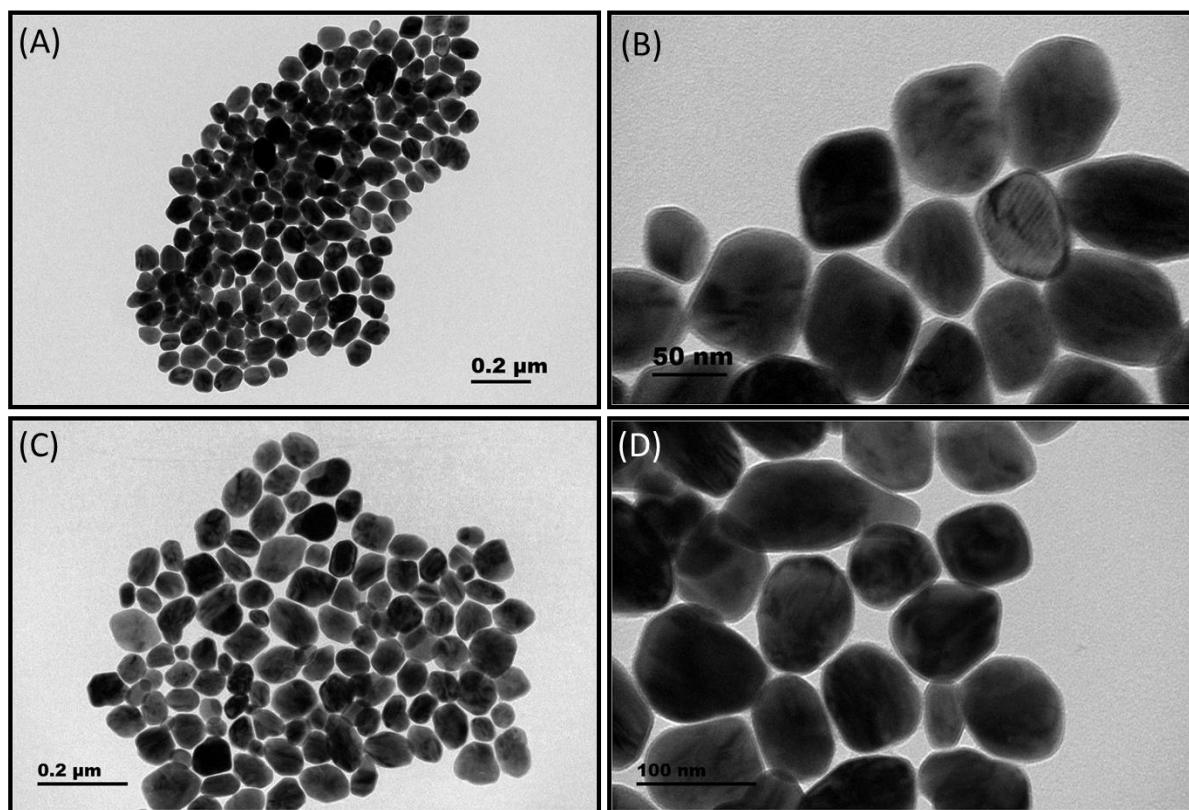


Figure 7.5. TEM images of Fe_5C_2 NPs synthesized using OAm to OAc molar ratio of 14:1

The crystalline structure of the Fe_5C_2 NPs was characterized using XRD analysis. Figure 7.6 represents the XRD patterns of Fe_5C_2 NPs synthesized with pure OAm (Figure 7.6A) and OAm/OAc mixture with a molar ratio of 14:1 (Figure 7.6B) which are consistent with the crystalline Fe_5C_2 (JCPDS no. 36-1248).

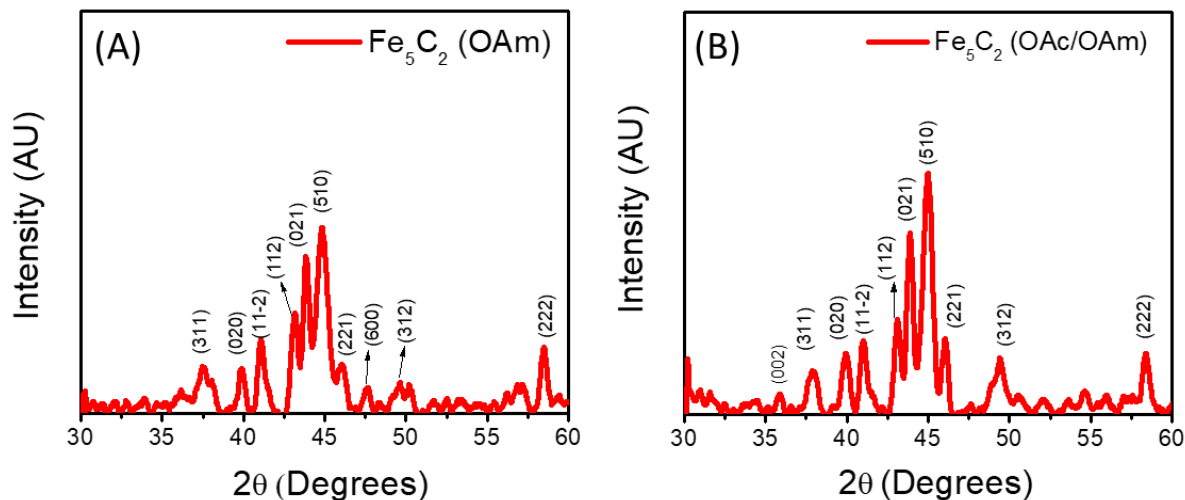


Figure 7.6. XRD of Fe₅C₂ NPs synthesized using (A) OAm and (B) mixture of OAc and OAm (1:14 molar ratio)

As observed under the TEM, an amorphous carbon shell was observed around some of the Fe₅C₂ NPs. Therefore, XPS and Raman data were obtained to understand the nature of the Fe₅C₂ NP surface. Figure 7.7 shows the XPS data for Fe₅C₂ NPs prepared with both OAm and mixture of OAm/OAc (Figure 7.7A, B and C, D respectively). In both samples, the presence of two peaks at 707.0 and 719.9 eV in Figure 7.7B and D indicating the existence of Fe₅C₂ NPs. However, the other two peaks at 724.5 and 710.8 eV are associated with Fe₃O₄, indicating the slight surface oxidation of the Fe₅C₂ NPs. This advocates the coexistence of a magnetite phase and the carbide phase at the surface.²⁴³ The peak at 284.8 eV in the C1s spectra in Figure 7.7A and C prove the existence of amorphous carbon on the NP surface. However, Fe 2p component of the polygonal shaped Fe₅C₂ NPs prepared in the presence of both OAm and OAc has two sharp peaks for Fe₅C₂ whereas in Fe₅C₂ rods they are significantly low intense. This may be due to the surface passivation of the Fe₅C₂ polygons by OAc which probably reduced the surface oxidation. It can be also due to the presence of an amorphous carbon layer around the Fe₅C₂ rods. Since XPS is a surface technique may be the Fe₅C₂ component underneath the surface may not have been detected.

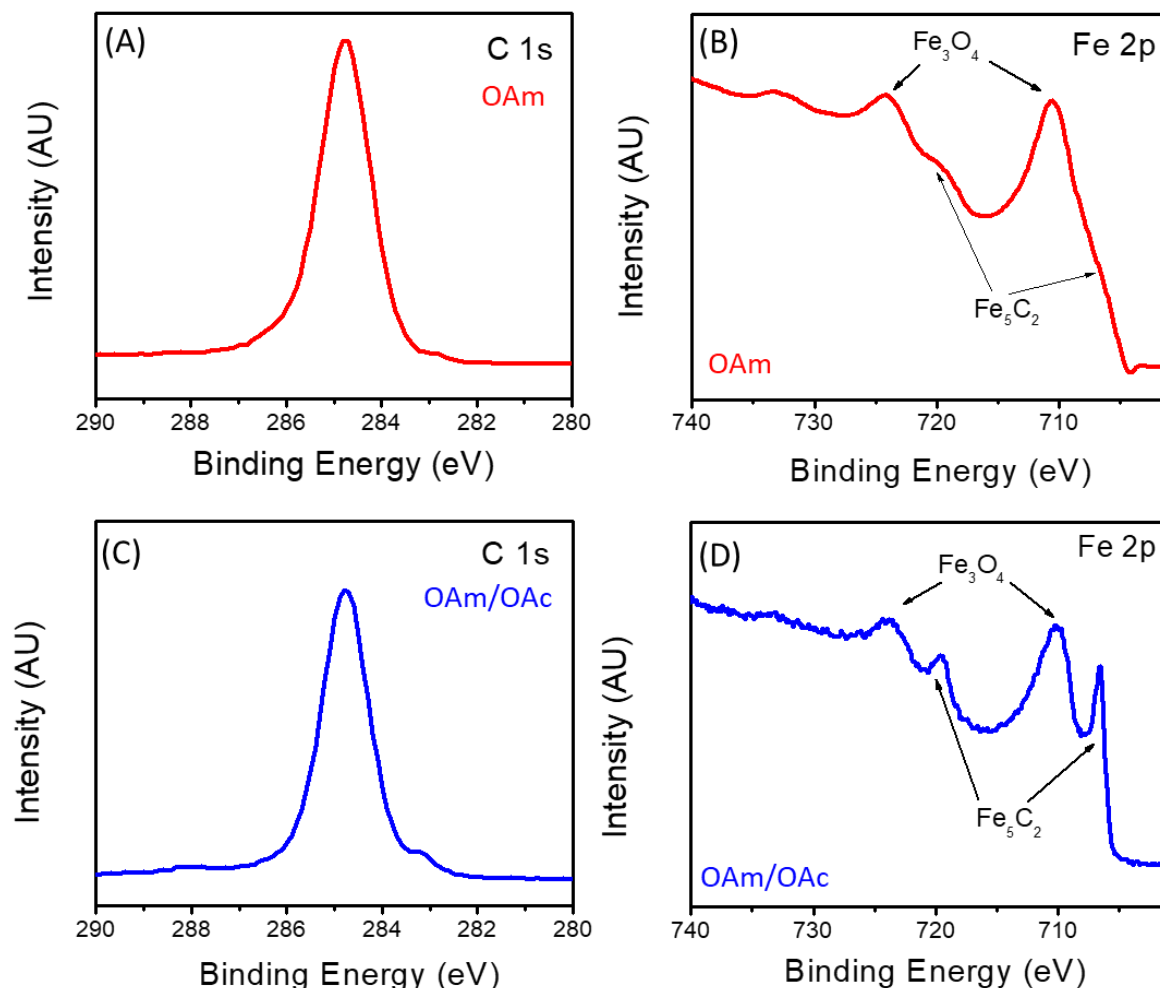


Figure 7.7. XPS data for Fe₅C₂ NPs synthesized using (A and B) OAm and (C and D) OAm/OAc (14:1)

In the Raman spectrum shown in Figure 7.8A and B, the G band at 1595 cm⁻¹ and the D band at 1326 cm⁻¹ proves the existence of graphitic carbon on the surface.²⁴⁴ Fe₅C₂ rods exhibit (Figure 7.8A) prominent and well-defined bands compared to Fe₅C₂ polygons (Figure 7.8B) probably due to the clearly visible amorphous carbon shell.

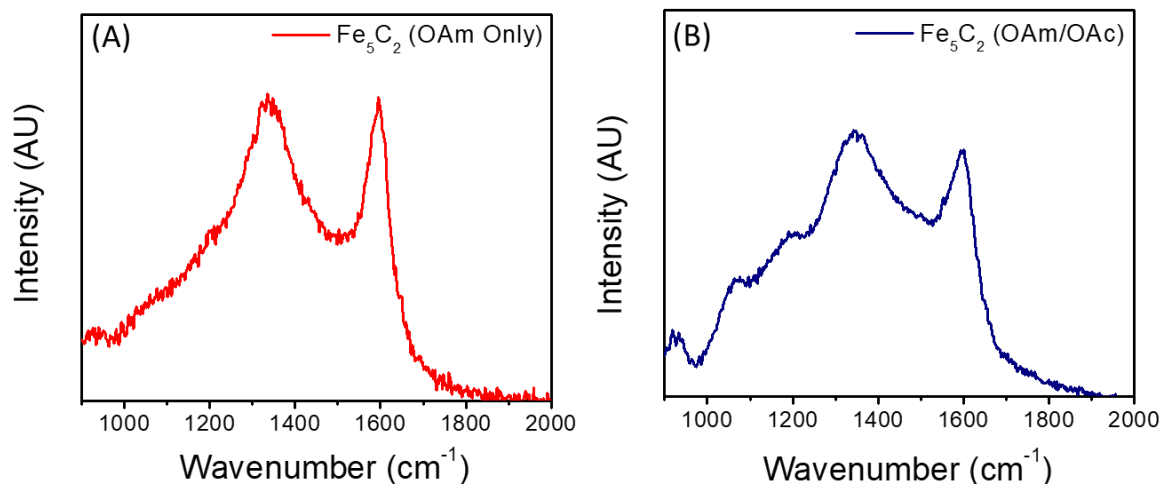


Figure 7.8. Raman spectra of Fe_5C_2 NPs synthesized using (A) OAm and (B) OAm/OAc (14:1)

Figure 7.9 illustrates the magnetic properties of the Fe_5C_2 NPs which were measured by means of VSM at room temperature. The hysteresis loop measurement up to 3 T was performed at 300 K for both Fe_5C_2 samples synthesized using OAm (Fe_5C_2 -OAm) and OAm/OAc mixture (Fe_5C_2 -OAm/OAc) (Figure 7.9). Both samples exhibit ferromagnetic-like behavior with saturation magnetization M_S and coercivity H_C of 103 and 67 emu/g and 290 and 600 Oe for Fe_5C_2 -OAm and Fe_5C_2 -OAm/OAc respectively. Based on the XPS and XRD results, both samples have a small amount of iron oxide (Fe_3O_4). These findings are confirmed by the magnetic measurement which shows slightly smaller M_S for both Fe_5C_2 samples compared to their bulk counterparts. To this regard, Fe_5C_2 -OAm has less amount of Fe_3O_4 than Fe_5C_2 -OAm/OAc and the large H_C value in Fe_5C_2 -OAm/OAc is due to the exchange coupling between the Fe_5C_2 and Fe_3O_4 phases. In addition, the amorphous carbon shell has a contribution of reducing the M_S values too. From the displayed hysteresis in Figure 7.9, the magnetic domain size of the Fe_5C_2 -OAm and Fe_5C_2 -OAm/OAc samples was determined based on the initial magnetic susceptibility²⁴⁵⁻²⁴⁶ to equal 4 and 6 nm respectively.

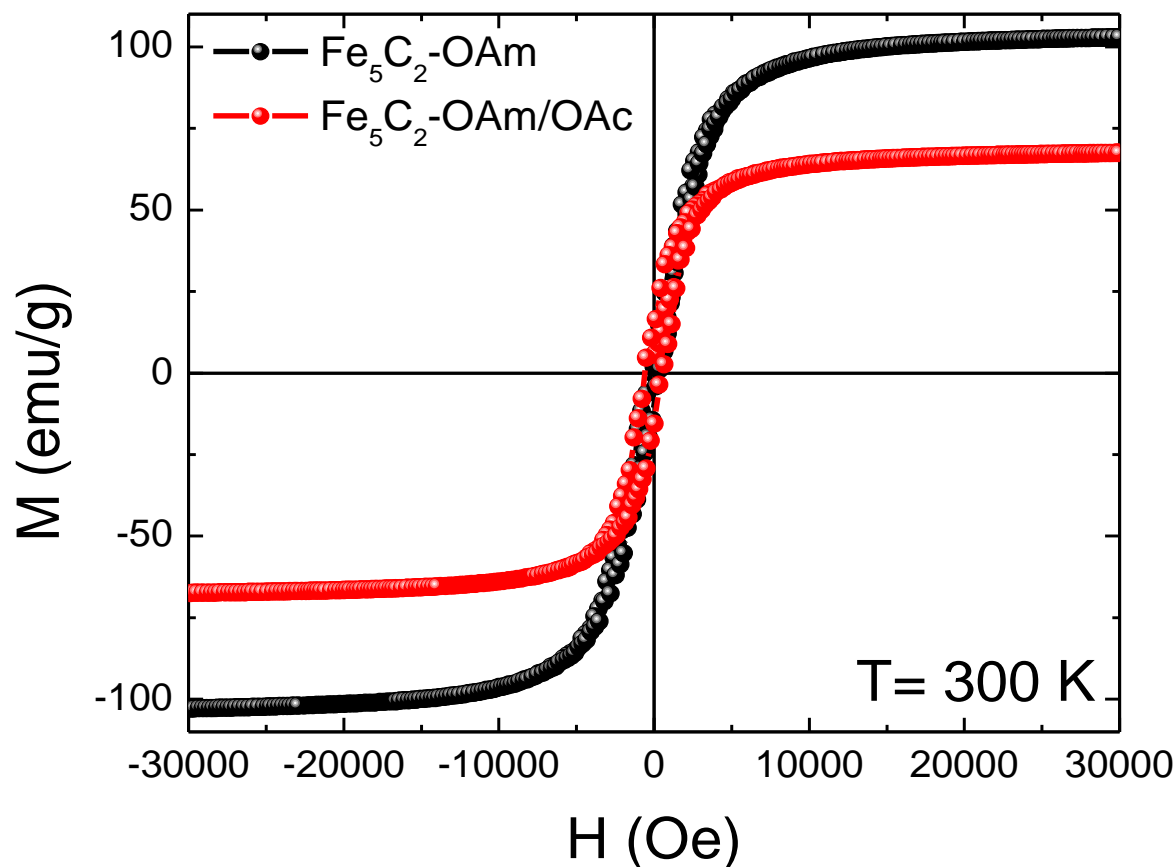


Figure 7.9. Room temperature dependence of magnetization on the external magnetic field for Fe_5C_2 NPs

7.3.2. Removal of Cr (VI) from Aqueous Solution by Fe_5C_2 NPs

7.3.2.1. The Effect of pH on Cr(VI) Removal

The effect of initial pH on the removal of Cr(VI) by Fe_5C_2 NPs, IGO- NH_2 and $\text{Fe}_5\text{C}_2\text{-IGO-NH}_2$ is shown in Figure 7.10. The adsorption capacity increases when the pH increases from 1 to 3 and the maximum adsorption of Cr(VI) occurs at pH 2 for Fe_5C_2 and $\text{Fe}_5\text{C}_2\text{-IGO-NH}_2$, and pH 3 for IGO- NH_2 . However, the adsorption capacity decreased significantly from pH 3 to 8. The results show that at high pH values, the removal efficiency of Cr(VI) decreased. Figure 7.10B shows a visual image of the solutions after conducting adsorption studies at different pH values. The sample

vial to the far right shows the retention of the color after the experiment showing the least adsorption at pH 8. This may be attributed to the competition between Cr(VI) anions and OH⁻ ions on the adsorption sites of iron carbide NPs. Hydroxyl ions are a strong competitor for adsorption because of its small size. With the decrease of solution pH values, the amount of Cr(VI) adsorbed at equilibrium (q_e) increase due to the presence of Cr(VI) in different ionic forms at acidic pH conditions (e.g. $\text{Cr}_4\text{O}_{13}^{2-}$, $\text{Cr}_2\text{O}_7^{2-}$, HCrO_4^-).²³⁰ The predominant Cr(VI) species at pH 2 is HCrO_4^- which is favorably adsorbed since it has a low adsorption free energy so the maximum uptake occurred at pH 2. All adsorption experiments were conducted at pH of 2 for (Fe_5C_2 and $\text{Fe}_5\text{C}_2\text{-IGO-NH}_2$) and at pH 3 for IGO-NH_2 .

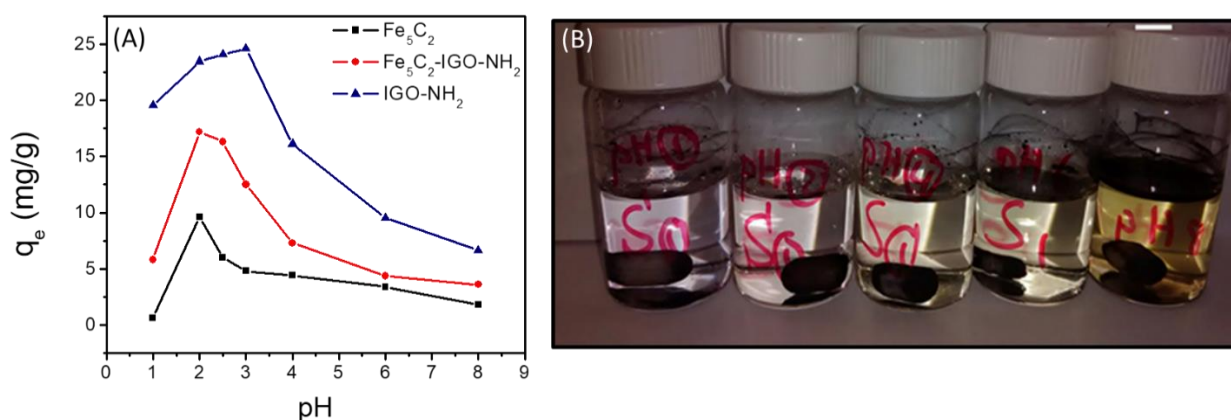


Figure 7.10. (A) Effect of pH of the solution on the removal of Cr(VI) by Fe_5C_2 , IGO-NH_2 , and $\text{Fe}_5\text{C}_2\text{-IGO-NH}_2$ nanocomposite. (Conditions: $C_0 = 22$ mg/L for Fe_5C_2 NPs, and 25 mg/L for IGO-NH_2 , and $\text{Fe}_5\text{C}_2\text{-IGO-NH}_2$ nanocomposite. $T = 273$ K, adsorbent dose = 0.005 g in 5 mL and (B) visual images of solutions of Cr(VI) at different pH values (from left to right pH 1, 2, 4, 6 and 8).

7.3.2.2. The Effect of Initial Concentration

The effect of initial concentration on the removal of Cr(VI) by Fe_5C_2 NPs, IGO-NH_2 and $\text{Fe}_5\text{C}_2\text{-IGO-NH}_2$ was studied at the optimum pH value for each sample (2 for Fe_5C_2 , $\text{Fe}_5\text{C}_2\text{-IGO-NH}_2$ and 3 for IGO-NH_2) at room temperature. As shown in Figure 7.11, it was observed that the equilibrium sorption capacities of the sorbents increase with the initial Cr(VI) concentration until

the equilibrium is reached. This is mainly due to the large concentration gradient at the solid-liquid interface created by the high initial Cr(VI) concentration which caused an increase of the amount of Cr(VI) adsorbed on the adsorbent. When the initial concentration of Cr(VI) was increased from 0.5 to 25 mg/L at 25 °C for Fe₅C₂ and from 10 mg/L to 200 mg/L for Fe₅C₂-IGO-NH₂ and IGO-NH₂ adsorbents, The amount of Cr(VI) adsorbed at equilibrium (q_e) increased from 0.44 to 11.74 mg/g, 8.0 to 21.0, and 10 to 50.4 for Fe₅C₂, Fe₅C₂-IGO-NH₂, and IGO-NH₂, respectively. However, the removal efficiencies were decreased from 88.0% to 39.0%, 80.0% to 10.5%, and 100.0% to 25.2% for Fe₅C₂, Fe₅C₂-IGO-NH₂, and IGO-NH₂, respectively. As expected, the adsorption capacity was increased with the Cr(VI) concentration. With more Cr(VI) present in the solution, a large fraction of active sites involves in the adsorption process. When the concentration was further increased q_e reached a plateau indicating saturation of the available binding sites of the adsorbent.

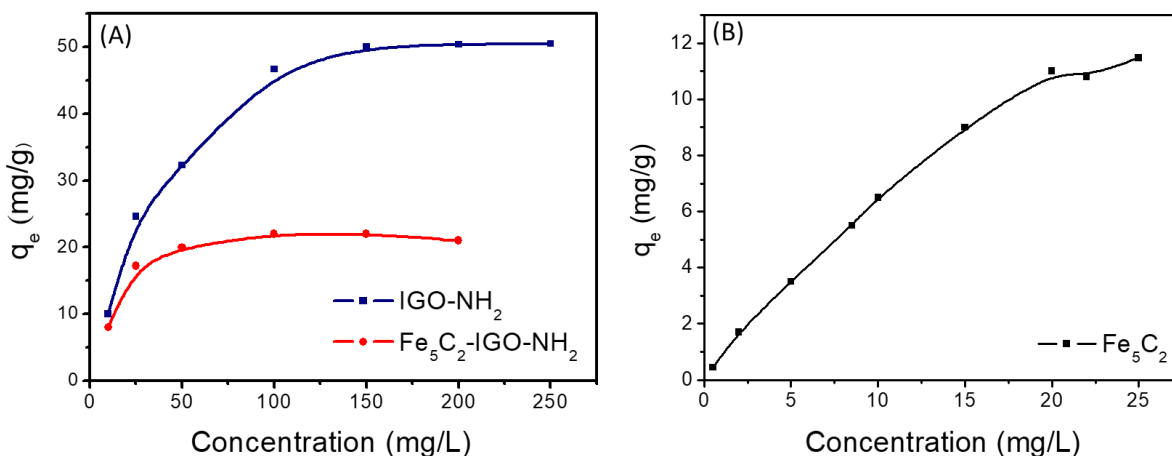


Figure 7.11. The effect of the initial concentration of Cr(VI) on the removal by (A) IGO-NH₂, Fe₅C₂-IGO-NH₂ and (B) Fe₅C₂, nanocomposite. (Conditions: [Cr(VI)] = 0.5 -250 mg/L, T = 273K, pH = 2 for Fe₅C₂, Fe₅C₂-IGO-NH₂ and pH = 3 for IGO-NH₂, Adsorbent dose = 0.005 g/5 mL)

7.3.2.3. The Effect of Contact Time

The effect of contact time on Cr(VI) removal was evaluated by varying the contact time (5-420 min), while other parameters were kept constant. According to the data shown in Figure 7.12, q_e increased with time and reached equilibrium. The adsorption rate was quite high in the beginning, followed by a much slower subsequent removal rate and then leading to an equilibrium condition. This is due to the availability of many vacant adsorption sites on the adsorbent surface at the initial stage and the high initial concentration driving force available for mass transfer from the liquid to the adsorbent active sites. Thereafter, the adsorption rate was slowed down near the adsorption equilibrium and the maximum removal of Cr(VI) occurred within 300, 180, and 90 min for Fe_5C_2 , IGO- NH_2 , and Fe_5C_2 - IGO- NH_2 respectively.

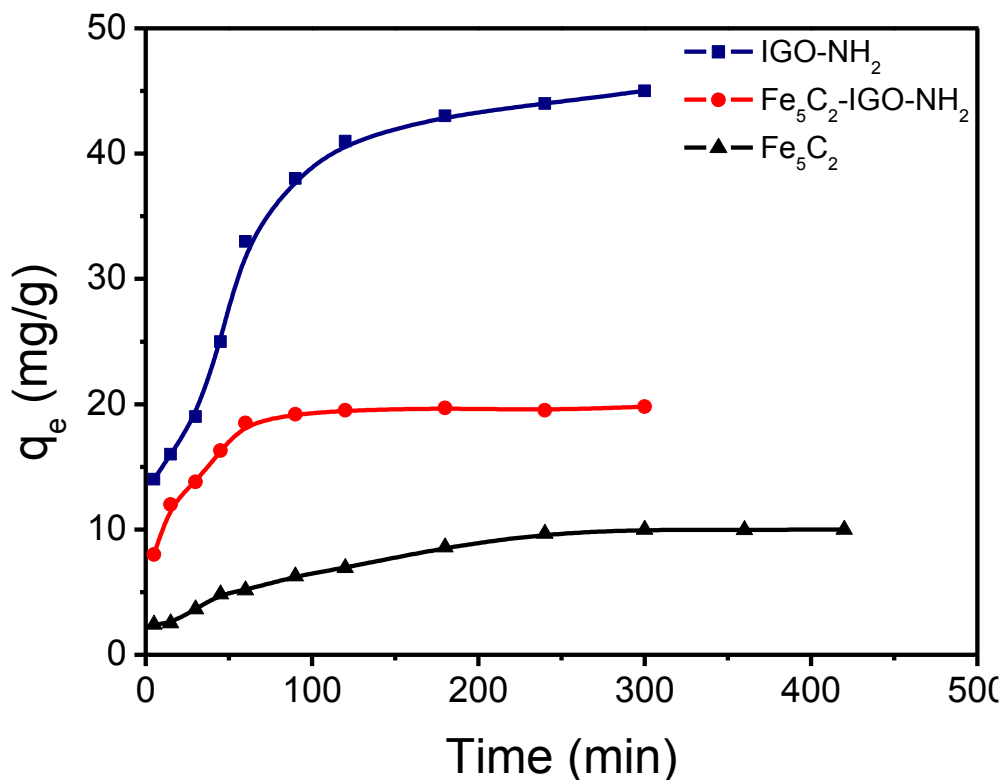


Figure 7.12. The effect of contact time on the removal of Cr(VI) by Fe₅C₂, IGO-NH₂, and Fe₅C₂-IGO-NH₂ nanocomposite. (Conditions: [Cr(VI)] = 22, 50, 100 for Fe₅C₂, IGO-NH₂, and Fe₅C₂-IGO-NH₂ respectively. T = 273 K, pH = 2 for Fe₅C₂, Fe₅C₂-IGO-NH₂ nanocomposite, pH = 3 for IGO-NH₂, Adsorbent dose = 0.005 g/5 mL)

7.3.2.4. The Effect of Adsorbent Dosage

The effect of adsorbent dose on the removal efficiency is shown in Figure 7.13. It could be clearly seen that when the dose was increased from 0.01 to 0.03 g, the removal efficiency was increased from 47.0 to 91.0%, from 44.0 to 76.1%, and from 46.7 to 79.5% for Fe₅C₂, Fe₅C₂-IGO-NH₂, and IGO-NH₂ respectively. This can be simply attributed to the increased sorbent surface area and availability of more sorption sites by increasing the adsorbent dose. It was also observed that as the adsorbent dose was increased from 0.005 to 0.03 g, q_e decreased from 5.5 to 3.64, from 40 to 12.68, and from 46.7 to 13.25 mg/g for Fe₅C₂, Fe₅C₂-IGO-NH₂, and IGO-NH₂ respectively. This is mainly due to the aggregation of iron carbide NPs with increasing adsorbent dose which leads

to a decrease in the number of active sites and total surface area of the adsorbent. Therefore, an optimum dose of 0.01 g/10 mL was selected for all the experiments.

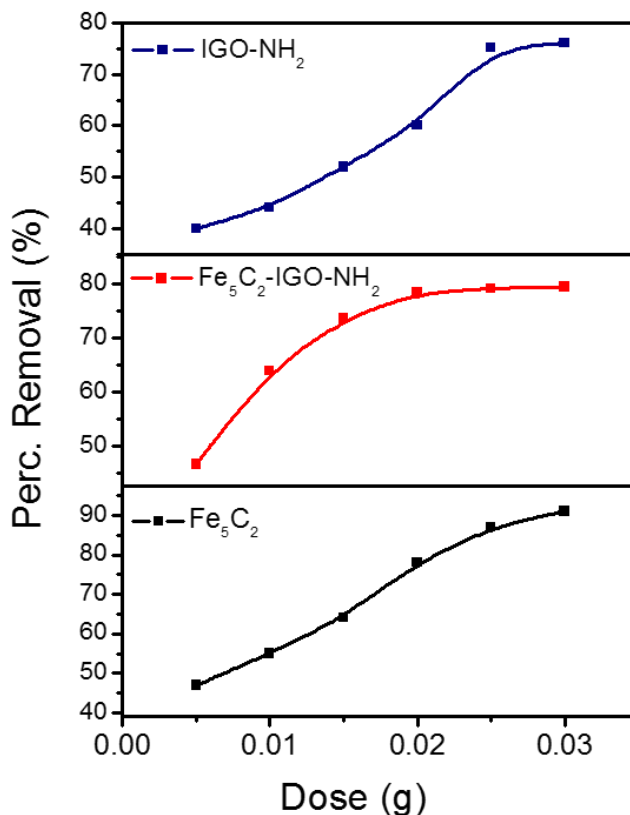


Figure 7.13. Effect of adsorbent dose on the removal of Cr(VI) by Fe₅C₂, IGO-NH₂, and Fe₅C₂-IGO-NH₂ nanocomposite. (Conditions: [Cr(VI)] = 10, 50, 100 mg L⁻¹ for Fe₅C₂, Fe₅C₂-IGO-NH₂ and IGO-NH₂, respectively. T= 273 K, pH = 2 for Fe₅C₂ and Fe₅C₂-IGO-NH₂ nanocomposite, pH = 3 for IGO-NH₂, Adsorbent dose = 0.005- 0.03 g/10 mL)

7.3.2.5. Desorption Studies

Desorption of Cr(VI) was done by disrupting the coordination between the adsorbent and the metal ions using NaOH as a desorbing agent. The subsequent release of Cr(VI) from the adsorbent surface into the desorbing medium was then studied. In order to investigate the desorption capacity, 0.005 g of Fe₅C₂, Fe₅C₂-IGO-NH₂, and IGO-NH₂ were introduced to 5 mL solutions of 15, 50, and 100 ppm Cr(VI) respectively. As the adsorption reaches equilibrium, the metal ion

concentration of the solution was measured. Then, the adsorbent loaded with Cr(VI) was collected and treated with 5 mL 0.05 M NaOH until the solution reached pH 10 to remove the adsorbed Cr(VI). As shown in Table 7.1, it was revealed that the percentage recovery was about 44.1% at pH 10 for IGO-NH₂.

Table 7.1. Desorption studies of Cr(VI) from at pH 10 using NaOH after the adsorption of 15, 50 and 100 mg/L of Cr(VI)

Adsorbent	q_e Adsorbed (mg g ⁻¹)	q_e Desorbed (mg g ⁻¹)	%Desorption
Fe ₅ C ₂	9.0	1.5	17.0
Fe ₅ C ₂ -IGO-NH ₂	20.0	9.8	49.0
IGO-NH ₂	46.7	20.6	44.2

7.3.2.6. Adsorption Capacities of Different Sorbents for Cr(VI) Removal

Table 7.2 lists the comparisons of maximum adsorption capacities of Fe₅C₂, Fe₅C₂-IGO-NH₂ and IGO-NH₂ obtained in this study with various adsorbents previously used for the adsorption of Cr(VI).^{226-231, 247-254} The adsorbents tested in this study show a higher adsorption capacity than most of the other adsorbents reported in the literature, suggesting that it may be effective for Cr(VI) removal from contaminated wastewater. Even though the maximum q_e was obtained for IGO-NH₂, Fe₅C₂-IGO-NH₂ has the advantage of easily getting extracted from the solution after adsorption due to the magnetic nature of Fe₅C₂ NPs.

Table 7.2. Comparison of the adsorption capacities of various adsorbents for Cr(VI) removal

Adsorbents	Adsorption capacities (mg/g)	References
Fe ₃ O ₄ NPs	3.56	230
Magnetic Graphene Nanocomposites	1.03	231
Maghemite NPs	1.55	229
Mixed magnetite and maghemite NPs	2.4	228
n-HAp/chitin composite	2.80	227
n-HAp/chitosan composite	3.40	227
Humic acid coated on magnetite	3.37	226
Silica gel chitosan composite	3.50	254
Grape stalks entrapped alginate beads	3.60	253
Alumina	3.71	252
Modified bentonite	4.21	251
Fe NPs embedded in orange peel pith	5.37	250
Fe@ α -Fe ₂ O ₃ core-shell nanowires.	7.74	249
Cu NPs coated polymer foam	9.16	255
Ca-Alginate composite	9.45	248
Magnetite	10.6	247
Fe ₅ C ₂ NPs	11.47	This Work
Fe ₅ C ₂ -IGO-NH ₂	21.00	
IGO-NH ₂	50.40	

7.4. Conclusions

In this project, a simple one-pot hot injection technique was introduced for the shape-controlled synthesis of anisotropic shapes of Fe_5C_2 NPs. Rod-shaped Fe_5C_2 NPs were obtained using OAm exclusively and different shapes of Fe_5C_2 NPs such as rice, heart, and polygonal shapes were obtained by changing the OAm to OAc molar ratio. Moreover, a composite material, Fe_5C_2 -IGO- NH_2 was prepared by introducing IGO- NH_2 into the reaction mixture before introducing the Fe source. Magnetic nature of the Fe_5C_2 NPs and the superior Cr(VI) removal efficiency of IGO- NH_2 , makes Fe_5C_2 -IGO- NH_2 composite an ideal adsorbent which can be easily extracted after the application, using a magnet for regeneration and recycling.

Fe_5C_2 NPs, Fe_5C_2 -IGO- NH_2 , and IGO- NH_2 were successfully evaluated as efficient adsorbents for removal of Cr (VI) from aqueous solutions. The results showed that the solution pH, contact time, adsorbent dosage and initial concentration significantly affected the adsorption amount of Cr(VI). It was found that the sorption process is pH-dependent and maximum sorption was obtained at pH 2 for (Fe_5C_2 and Fe_5C_2 -IGO- NH_2) and of pH 3 for IGO- NH_2 . The sorption studies were carried out using different Cr(VI) concentrations. It was found that the extent of Cr(VI) sorption increases upon increasing Cr(VI) concentration within the range studied. The maximum adsorption capacity is 11.47, 21.00, and 50.40 mg/g for Fe_5C_2 , Fe_5C_2 -IGO- NH_2 , and IGO- NH_2 , respectively. It was also found that the extent of Cr(VI) adsorption increases upon increasing the contact time until equilibrium is reached (300, 180, and 90 min for Fe_5C_2 , IGO- NH_2 , and Fe_5C_2 -IGO- NH_2 , respectively).

Chapter 08: Summary and Conclusions

The work presented in this dissertation reports the utility of nanostructured materials in solar desalination and water treatment (photodegradation and heavy metal removal). Under solar desalination, three materials were reported namely, plasmonic graphene polyurethane nanocomposite, plasmonic functionalized cotton, and carbonized cotton. Under photodegradation, the synthesis of unique “sea urchin” shaped zinc oxide nanorod clusters was reported for photodegradation of organic dyes in wastewater. Under heavy metal removal, the synthesis of iron carbide and aminated improved graphene oxide nanocomposite and its applications in Cr(VI) removal from wastewater was described.

In the third chapter, a new class of PGPU nanocomposite foam for efficient solar water desalination is described. With the characteristics of high optical absorption, low thermal conductivity, effective water transmission, and the capacity of self-floating, the PGPU foam can be an attractive material for efficient solar steam generation. Moreover, the functional foam exhibited excellent stability due to the covalent bonds formed between GO and PU matrix. Under the solar intensities of 1 and 8 kW m⁻², Ag/Au-GO-PU material exhibited the highest steam generation rate (1.00 and 11.34 kg m⁻² h⁻¹ respectively). However, plasmonic-free GO-PU composite exhibited competitive steam generation rates showing 0.82 and 10.62 kg m⁻² h⁻¹ under 1 and 8 kW m⁻² respectively. Considering reduced fabrication cost by removing expensive plasmonic metal NPs, GO-PU can be a competitive candidate for large scale applications of this material. The current contribution offers the opportunity for improved solar photothermal energy conversion for many applications including domestic water heating, solar-driven desalination, solar steam for industrial purposes, solar crop drying technologies, and basic solar stills to purify water in remote regions.

In the fourth chapter, a new class of PFC nanocomposite fibers was reported for efficient solar water desalination and wastewater treatment. With the unique features such as high optical absorption, low thermal conductivity, effective water transmission, and the capacity of self-floating, the PFC foam can be considered as an attractive material for solar desalination and wastewater treatment. Following the same trend as in the case of PGPU, PFC composite with both Au and Ag NPs exhibited the highest steam generation rates showing 1.4, 6.7 and 11.3 kg m⁻² h⁻¹ under 1, 5 and 8 kW m⁻² respectively. This is due to the efficient absorption of solar energy in a broad range of the solar spectrum by both Au and Ag NPs. Moreover, the material exhibits excellent stability over multiple cycles indicating its reusability in practical applications. Utilization of low-cost materials such as cotton and low plasmonic metal loading leads to fabricate an economically feasible material compared to other desalination techniques such as reverse osmosis and membrane-based filters.

Chapter five reports a novel low-cost carbonized cotton device for efficient solar steam generation and wastewater treatment. The special design of this device minimized the area that contact with bulk water which efficiently minimized the conductive heat loss. Despite the absence of well-known solar absorbers such as plasmonic NPs and GO, CC device exhibited almost similar steam generation rates and solar-to-vapor efficiencies to the PGPU and PFC materials. The characteristic features such as durability, minimized conductive heat loss, and self-floating capability make CC device a perfect candidate for efficient solar steam generation and wastewater treatment. Moreover, the use of low-cost materials such as cotton makes it an economically viable device for energy-yielding applications such as SWD.

Chapter six describes the synthesis of unique sea urchin shaped ZnO nanostructures for photodegradation of organic dyes. According to TEM and XRD data, it was proven that the key

step behind the sequential growth of SU shape is the formation of seed clusters during the seep preparation step. When the seeds were kept separated using a surfactant, CTAB, SU shape was not formed. The obtained 3D nanostructures were in the range of 0.5-1.5 μm in size and possess a specific surface area of 26.94 m^2/g . The high photocatalytic activity of the material was assessed by the photodegradation efficiency of three organic dyes, MB, IC and Rh B in aqueous solutions. Weak chemical adsorption of anionic MB on the catalyst surface brought a slightly negative effect on its photodegradation but still achieved 86% of removal efficiency after one hour of UV irradiation. Therefore, SU ZnO shows the potential to be a versatile catalyst in photodegrading industrial wastewater containing organic dyes.

In chapter seven, shape-controlled synthesis of magnetic Fe_5C_2 NPs and synthesis of Fe_5C_2 -IGO- NH_2 magnetic composite for the removal of Cr(VI) in wastewater was reported. A simple one-pot hot injection technique was introduced for the shape-controlled synthesis of anisotropic shapes of Fe_5C_2 NPs. Rod-shaped Fe_5C_2 NPs were obtained using OAm exclusively and different shapes of Fe_5C_2 NPs such as rice, heart, and polygonal shapes were obtained by changing the OAm to OAc molar ratio. Moreover, a composite material, Fe_5C_2 -IGO- NH_2 was prepared by introducing IGO- NH_2 into the reaction mixture before introducing the Fe source. Magnetic nature of the Fe_5C_2 NPs and the superior Cr(VI) removal efficiency of IGO- NH_2 , makes Fe_5C_2 -IGO- NH_2 composite an ideal adsorbent which can be easily extracted after the application, using a magnet for regeneration and recycling.

Fe_5C_2 NPs, Fe_5C_2 -IGO- NH_2 , and IGO- NH_2 were successfully evaluated as efficient adsorbents for removal of Cr (VI) from aqueous solutions. The results showed that the solution pH, contact time, adsorbent dosage and initial concentration significantly affected the adsorption amount of Cr(VI). It was found that the sorption process is pH-dependent and maximum sorption was obtained at pH

2 for (Fe_5C_2 and $\text{Fe}_5\text{C}_2\text{-IGO-NH}_2$) and of pH 3 for IGO-NH_2 . The sorption studies were carried out using different Cr(VI) concentrations. It was found that the extent of Cr(VI) sorption increases upon increasing Cr(VI) concentration within the range studied. The maximum adsorption capacity is 11.47, 21.00, and 50.40 mg/g for Fe_5C_2 , $\text{Fe}_5\text{C}_2\text{-IGO-NH}_2$, and IGO-NH_2 , respectively. It was also found that the extent of Cr(VI) adsorption increases upon increasing the contact time until equilibrium is reached (300, 180, and 90 min for Fe_5C_2 , IGO-NH_2 , and $\text{Fe}_5\text{C}_2\text{-IGO-NH}_2$, respectively).

Even though this dissertation covers three techniques to find solutions for water-related issues, solar desalination can be highlighted as the main area of research. The primary objective to introduce a cost-effective, durable and scalable solar desalination device with high photothermal properties was successfully achieved by considerably reducing the fabrication cost from the PGPU nanocomposite to the CC device. Continuing research in the El-Shall lab is now focused on fabricating a large-scale low-cost solar desalination device for practical applications.

References

1. Mekonnen, M. M.; Hoekstra, A. Y., Four billion people facing severe water scarcity. *Sci. Adv.* **2016**, *2*, e1500323.
2. Vörösmarty, C. J.; Green, P.; Salisbury, J.; Lammers, R. B., Global water resources: vulnerability from climate change and population growth. *Science* **2000**, *289*, 284-288.
3. Erzin, A. E.; Hoekstra, A. Y., Water footprint scenarios for 2050: A global analysis. *Environment International* **2014**, *64*, 71-82.
4. Gleick, P. H., Water in crisis. *Pacific Institute for Studies in Dev., Environment & Security. Stockholm Env. Institute, Oxford Univ. Press.* 473p **1993**, 9.
5. Connor, R.; Renata, A.; Ortigara, C.; Koncagül, E.; Uhlenbrook, S.; Lamizana-Diallo, B. M.; Zadeh, S. M.; Qadir, M.; Kjellén, M.; Sjödin, J., The united nations world water development report 2017. wastewater: The untapped resource. *The United Nations World Water Development Report* **2017**.
6. Al-Karaghoul, A.; Renne, D.; Kazmerski, L. L., Solar and wind opportunities for water desalination in the Arab regions. *Renewable Sustainable Energy Rev.* **2009**, *13*, 2397-2407.
7. Kabeel, A.; Hamed, M. H.; Omara, Z.; Sharshir, S., Water desalination using a humidification-dehumidification technique—a detailed review. *Nat. Resour.* **2013**, *4*, 286.
8. Delyannis, E., Historic background of desalination and renewable energies. *Solar Energy* **2003**, *75*, 357-366.
9. Qiblawey, H. M.; Banat, F., Solar thermal desalination technologies. *Desalination* **2008**, *220*, 633-644.
10. Laboratory, N. R. E. Reference air mass 1.5 spectra. <https://www.nrel.gov/grid/solar-resource/spectra-am1.5.html>.
11. Al-Hayeka, I.; Badran, O. O., The effect of using different designs of solar stills on water distillation. *Desalination* **2004**, *169*, 121-127.
12. Chong, T.-L.; Huang, B.-J.; Wu, P.-H.; Kao, Y.-C., Multiple-effect diffusion solar still coupled with a vacuum-tube collector and heat pipe. *Desalination* **2014**, *347*, 66-76.
13. Huang, B.-J.; Chong, T.-L.; Wu, P.-H.; Dai, H.-Y.; Kao, Y.-C., Spiral multiple-effect diffusion solar still coupled with vacuum-tube collector and heat pipe. *Desalination* **2015**, *362*, 74-83.

14. Rady, H. S.; Emam, A. N.; Mohamed, M. B.; El-Shall, M. S., Graphene oxide interface enhances the photochemical synthesis, stability and photothermal effect of plasmonic gold nanostructures. *Chem. Phys. Lett.* **2017**, 690, 153-158.
15. Zedan, A. F.; Moussa, S.; Turner, J.; Atkinson, G.; El-Shall, M. S., Ultrasmall Gold Nanoparticles Anchored to Graphene and Enhanced Photothermal Effects by Laser Irradiation of Gold Nanostructures in Graphene Oxide Solutions. *ACS Nano* **2013**, 7, 627-636.
16. Abdelsayed, V.; Moussa, S.; Hassan, H. M.; Aluri, H. S.; Collinson, M. M.; El-Shall, M. S., Photothermal deoxygenation of graphite oxide with laser excitation in solution and graphene-aided increase in water temperature. *J. Phys. Chem. Lett.* **2010**, 1, 2804-2809.
17. Neumann, O.; Urban, A. S.; Day, J.; Lal, S.; Nordlander, P.; Halas, N. J., Solar Vapor Generation Enabled by Nanoparticles. *ACS Nano* **2013**, 7, 42-49.
18. Jaque, D.; Martínez Maestro, L.; del Rosal, B.; Haro-Gonzalez, P.; Benayas, A.; Plaza, J. L.; Martín Rodríguez, E.; García Solé, J., Nanoparticles for photothermal therapies. *Nanoscale* **2014**, 6, 9494-9530.
19. Hammer, B.; Norskov, J. K., Why gold is the noblest of all the metals. *Nature* **1995**, 376, 238-240.
20. Gao, Y.; Yuan, Z.; Gao, S., Semiclassical approach to plasmon–electron coupling and Landau damping of surface plasmons. *J. Chem. Phys.* **2011**, 134, 134702.
21. Li, C.; Wang, Z.; Wang, P.-I.; Peles, Y.; Koratkar, N.; Peterson, G. P., Nanostructured Copper Interfaces for Enhanced Boiling. *Small* **2008**, 4, 1084-1088.
22. Zhou, L.; Tan, Y.; Wang, J.; Xu, W.; Yuan, Y.; Cai, W.; Zhu, S.; Zhu, J., 3D self-assembly of aluminium nanoparticles for plasmon-enhanced solar desalination. *Nat. Photonics* **2016**, 10, 393.
23. Zhang, L.; Xing, J.; Wen, X.; Chai, J.; Wang, S.; Xiong, Q., Plasmonic heating from indium nanoparticles on a floating microporous membrane for enhanced solar seawater desalination. *Nanoscale* **2017**, 9, 12843-12849.
24. Ito, Y.; Tanabe, Y.; Han, J.; Fujita, T.; Tanigaki, K.; Chen, M., Multifunctional porous graphene for high-efficiency steam generation by heat localization. *Adv. Mater.* **2015**, 27, 4302-4307.
25. Gao, X.; Ren, H.; Zhou, J.; Du, R.; Yin, C.; Liu, R.; Peng, H.; Tong, L.; Liu, Z.; Zhang, J., Synthesis of hierarchical graphdiyne-based architecture for efficient solar steam generation. *Chem. Mater.* **2017**, 29, 5777-5781.

26. Liu, K.-K.; Jiang, Q.; Tadepalli, S.; Raliya, R.; Biswas, P.; Naik, R. R.; Singamaneni, S., Wood–graphene oxide composite for highly efficient solar steam generation and desalination. *ACS Appl. Mater. Interfaces* **2017**, *9*, 7675-7681.
27. Yin, Z.; Wang, H.; Jian, M.; Li, Y.; Xia, K.; Zhang, M.; Wang, C.; Wang, Q.; Ma, M.; Zheng, Q.-s., Extremely black vertically aligned carbon nanotube arrays for solar steam generation. *ACS Appl. Mater. Interfaces* **2017**, *9*, 28596-28603.
28. Zhu, L.; Gao, M.; Peh, C. K. N.; Wang, X.; Ho, G. W., Self-Contained Monolithic Carbon Sponges for Solar-Driven Interfacial Water Evaporation Distillation and Electricity Generation. *Adv. Energy Mater.* **2018**, *8*, 1702149.
29. Xu, N.; Hu, X.; Xu, W.; Li, X.; Zhou, L.; Zhu, S.; Zhu, J., Mushrooms as efficient solar steam-generation devices. *Adv. Mater.* **2017**, *29*, 1606762.
30. Hu, X.; Xu, W.; Zhou, L.; Tan, Y.; Wang, Y.; Zhu, S.; Zhu, J., Tailoring Graphene Oxide-Based Aerogels for Efficient Solar Steam Generation under One Sun. *Adv. Mater.* **2017**, *29*, 1604031.
31. Hu, M.; Mi, B., Enabling graphene oxide nanosheets as water separation membranes. *Environ. Sci. Technol.* **2013**, *47*, 3715-3723.
32. Shi, L.; Yang, J.; Huang, Z.; Li, J.; Tang, Z.; Li, Y.; Zheng, Q., Fabrication of transparent, flexible conducting graphene thin films via soft transfer printing method. *Appl. Surf. Sci.* **2013**, *276*, 437-446.
33. Eda, G.; Fanchini, G.; Chhowalla, M., Large-area ultrathin films of reduced graphene oxide as a transparent and flexible electronic material. *Nat. Nanotechnol.* **2008**, *3*, 270.
34. Tian, L.; Anilkumar, P.; Cao, L.; Kong, C. Y.; Meziani, M. J.; Qian, H.; Veca, L. M.; Thorne, T. J.; Tackett, K. N.; Edwards, T., Graphene oxides dispersing and hosting graphene sheets for unique nanocomposite materials. *ACS nano* **2011**, *5*, 3052-3058.
35. Renteria, J. D.; Ramirez, S.; Malekpour, H.; Alonso, B.; Centeno, A.; Zurutuza, A.; Cocemasov, A. I.; Nika, D. L.; Balandin, A. A., Strongly anisotropic thermal conductivity of free-standing reduced graphene oxide films annealed at high temperature. *Adv. Funct. Mater.* **2015**, *25*, 4664-4672.
36. Sun, P.; Liu, H.; Wang, K.; Zhong, M.; Wu, D.; Zhu, H., Ultrafast liquid water transport through graphene-based nanochannels measured by isotope labelling. *Chem. Commun.* **2015**, *51*, 3251-3254.
37. Xue, G.; Liu, K.; Chen, Q.; Yang, P.; Li, J.; Ding, T.; Duan, J.; Qi, B.; Zhou, J., Robust and Low-Cost Flame-Treated Wood for High-Performance Solar Steam Generation. *ACS Appl. Mater. Interfaces* **2017**, *9*, 15052-15057.

38. Liu, P.-F.; Miao, L.; Deng, Z.; Zhou, J.; Su, H.; Sun, L.; Tanemura, S.; Cao, W.; Jiang, F.; Zhao, L.-D., A mimetic transpiration system for record high conversion efficiency in solar steam generator under one-sun. *Mater. Today Energy* **2018**, 8, 166-173.
39. Chen, C.; Li, Y.; Song, J.; Yang, Z.; Kuang, Y.; Hitz, E.; Jia, C.; Gong, A.; Jiang, F.; Zhu, J. Y.; Yang, B.; Xie, J.; Hu, L., Highly Flexible and Efficient Solar Steam Generation Device. *Adv. Mater.* **2017**, 29, 1701756.
40. Kisch, H., Semiconductor Photocatalysis Mechanistic and Synthetic Aspects. *Angew. Chem.-Int. Edit.* **2013**, 52, 812-847.
41. Sakthivel, S.; Neppolian, B.; Palanichamy, M.; Arabindoo, B.; Murugesan, V., Photocatalytic degradation of leather dye, Acid green 16 using ZnO in the slurry and thin film forms. **1999**.
42. Sakthivel, S.; Shankar, M.; Palanichamy, M.; Arabindoo, B.; Murugesan, V., Photocatalytic decomposition of leather dye: comparative study of TiO₂ supported on alumina and glass beads. *J. Photochem. Photobiol., A* **2002**, 148, 153-159.
43. Zhao, H.; Li, R. K., A study on the photo-degradation of zinc oxide (ZnO) filled polypropylene nanocomposites. *Polymer* **2006**, 47, 3207-3217.
44. Wang, W.; Serp, P.; Kalck, P.; Faria, J. L., Visible light photodegradation of phenol on MWNT-TiO₂ composite catalysts prepared by a modified sol-gel method. *J. Mol. Catal. A: Chem.* **2005**, 235, 194-199.
45. Zhou, J.; Zhang, Y.; Zhao, X.; Ray, A. K., Photodegradation of benzoic acid over metal-doped TiO₂. *Ind. Eng. Chem. Res.* **2006**, 45, 3503-3511.
46. Ong, C. B.; Ng, L. Y.; Mohammad, A. W., A review of ZnO nanoparticles as solar photocatalysts: Synthesis, mechanisms and applications. *Renewable Sustainable Energy Rev.* **2018**, 81, 536-551.
47. Sakthivel, S.; Neppolian, B.; Shankar, M. V.; Arabindoo, B.; Palanichamy, M.; Murugesan, V., Solar photocatalytic degradation of azo dye: comparison of photocatalytic efficiency of ZnO and TiO₂. *Sol. Energy Mater. Sol. Cells* **2003**, 77, 65-82.
48. Tong, H.; Ouyang, S.; Bi, Y.; Umezawa, N.; Oshikiri, M.; Ye, J., Nano-photocatalytic Materials: Possibilities and Challenges. *Adv. Mater.* **2012**, 24, 229-251.
49. Rauf, M.; Ashraf, S. S., Fundamental principles and application of heterogeneous photocatalytic degradation of dyes in solution. *Chem. Eng. J.* **2009**, 151, 10-18.
50. Rajamanickam, D.; Shanthi, M., Photocatalytic degradation of an organic pollutant by zinc oxide-solar process. *Arabian J. Chem.* **2016**, 9, S1858-S1868.

51. Fu, F.; Wang, Q., Removal of heavy metal ions from wastewaters: a review. *J. Environ. Manage.* **2011**, 92, 407-418.
52. Srivastava, N.; Majumder, C., Novel biofiltration methods for the treatment of heavy metals from industrial wastewater. *J. Hazard. Mater.* **2008**, 151, 1-8.
53. Wuana, R. A.; Okieimen, F. E., Heavy metals in contaminated soils: a review of sources, chemistry, risks and best available strategies for remediation. *Isrn Ecology* **2011**, 2011.
54. Awad, F. S.; AbouZeid, K. M.; El-Maaty, W. M. A.; El-Wakil, A. M.; El-Shall, M. S., Efficient removal of heavy metals from polluted water with high selectivity for mercury (II) by 2-imino-4-thiobiuret–partially reduced graphene oxide (IT-PRGO). *ACS Appl. Mater. Interfaces* **2017**, 9, 34230-34242.
55. Bensaadi, S.; Nasrallah, N.; Amrane, A.; Trari, M.; Kerdjoudj, H.; Arous, O.; Amara, M., Dialysis and photo-electrodialysis processes using new synthesized polymeric membranes for the selective removal of bivalent cations. *J. Environ. Chem. Eng.* **2017**, 5, 1037-1047.
56. Abejón, A.; Garea, A.; Irabien, A., Arsenic removal from drinking water by reverse osmosis: Minimization of costs and energy consumption. *Separation and Purification Technology* **2015**, 144, 46-53.
57. Nidheesh, P.; Singh, T. A., Arsenic removal by electrocoagulation process: recent trends and removal mechanism. *Chemosphere* **2017**, 181, 418-432.
58. Lam, B.; Déon, S.; Morin-Crini, N.; Crini, G.; Fievet, P., Polymer-enhanced ultrafiltration for heavy metal removal: Influence of chitosan and carboxymethyl cellulose on filtration performances. *J. Cleaner Prod.* **2018**, 171, 927-933.
59. Sunil, K.; Karunakaran, G.; Yadav, S.; Padaki, M.; Zadorozhnyy, V.; Pai, R. K., Al-Ti₂O₆ a mixed metal oxide based composite membrane: A unique membrane for removal of heavy metals. *Chem. Eng. J.* **2018**, 348, 678-684.
60. El-Din, A. F. T.; El-Khouly, M. E.; Elshehy, E. A.; Atia, A. A.; El-Said, W. A., Cellulose acetate assisted synthesis of worm-shaped mesopores of MgP ion-exchanger for cesium ions removal from seawater. *Microporous Mesoporous Mater.* **2018**, 265, 211-218.
61. Kameda, T.; Suzuki, Y.; Yoshioka, T., Removal of arsenic from an aqueous solution by coprecipitation with manganese oxide. *J. Environ. Chem. Eng.* **2014**, 2, 2045-2049.
62. Barakat, M., New trends in removing heavy metals from industrial wastewater. *Arabian J. Chem.* **2011**, 4, 361-377.
63. Khorzughy, S. H.; Eslamkish, T.; Ardejani, F. D.; Heydartaemeh, M. R., Cadmium removal from aqueous solutions by pumice and nano-pumice. *Korean J. Chem. Eng.* **2015**, 32, 88-96.

64. Nguyen, T.; Ngo, H.; Guo, W.; Zhang, J.; Liang, S.; Yue, Q.; Li, Q.; Nguyen, T., Applicability of agricultural waste and by-products for adsorptive removal of heavy metals from wastewater. *Bioresour. Technol.* **2013**, *148*, 574-585.
65. Allen, S.; McKay, G.; Porter, J. F., Adsorption isotherm models for basic dye adsorption by peat in single and binary component systems. *J. Colloid Interface Sci.* **2004**, *280*, 322-333.
66. Limousin, G.; Gaudet, J.-P.; Charlet, L.; Szenknect, S.; Barthes, V.; Krimissa, M., Sorption isotherms: a review on physical bases, modeling and measurement. *Appl. Geochem.* **2007**, *22*, 249-275.
67. Zhang, P.; Wang, L., Extended Langmuir equation for correlating multilayer adsorption equilibrium data. *Sep. Purif. Technol.* **2010**, *70*, 367-371.
68. Srivastava, V. C.; Swamy, M. M.; Mall, I. D.; Prasad, B.; Mishra, I. M., Adsorptive removal of phenol by bagasse fly ash and activated carbon: equilibrium, kinetics and thermodynamics. *Colloids Surf., A* **2006**, *272*, 89-104.
69. Wang, S.; Peng, Y., Natural zeolites as effective adsorbents in water and wastewater treatment. *Chem. Eng. J.* **2010**, *156*, 11-24.
70. El-Aziz, M. A.; Kamal, K. H.; Ali, K.; Abdel-Aziz, M.; Kamel, S., Biodegradable grafting cellulose/clay composites for metal ions removal. *Int. J. Biol. Macromol.* **2018**, *118*, 2256-2264.
71. Nomanbhay, S. M.; Palanisamy, K., Removal of heavy metal from industrial wastewater using chitosan coated oil palm shell charcoal. *Electron. J. Biotechnol.* **2005**, *8*, 43-53.
72. Yantasee, W.; Lin, Y.; Fryxell, G. E.; Alford, K. L.; Busche, B. J.; Johnson, C. D., Selective removal of copper (II) from aqueous solutions using fine-grained activated carbon functionalized with amine. *Ind. Eng. Chem. Res.* **2004**, *43*, 2759-2764.
73. Antochshuk, V.; Olkhovyk, O.; Jaroniec, M.; Park, I.-S.; Ryoo, R., Benzoylthiourea-modified mesoporous silica for mercury (II) removal. *Langmuir* **2003**, *19*, 3031-3034.
74. Kampalanonwat, P.; Supaphol, P., Preparation and adsorption behavior of aminated electrospun polyacrylonitrile nanofiber mats for heavy metal ion removal. *ACS Appl. Mater. Interfaces* **2010**, *2*, 3619-3627.
75. Sarma, G. K.; Gupta, S. S.; Bhattacharyya, K. G., Nanomaterials as versatile adsorbents for heavy metal ions in water: a review. *Environ. Sci. Pollut. Res.* **2019**, *26*, 6245-6278.
76. Zhang, W.; Shi, X.; Zhang, Y.; Gu, W.; Li, B.; Xian, Y., Synthesis of water-soluble magnetic graphene nanocomposites for recyclable removal of heavy metal ions. *J. Mater. Chem. A* **2013**, *1*, 1745-1753.

77. Ge, F.; Li, M.-M.; Ye, H.; Zhao, B.-X., Effective removal of heavy metal ions Cd²⁺, Zn²⁺, Pb²⁺, Cu²⁺ from aqueous solution by polymer-modified magnetic nanoparticles. *J. Hazard. Mater.* **2012**, *211*, 366-372.
78. Liu, J.-F.; Zhao, Z.-s.; Jiang, G.-b., Coating Fe₃O₄ magnetic nanoparticles with humic acid for high efficient removal of heavy metals in water. *Environ. Sci. Technol.* **2008**, *42*, 6949-6954.
79. Elimelech, M.; Phillip, W. A., The Future of Seawater Desalination: Energy, Technology, and the Environment. *Science* **2011**, *333*, 712-717.
80. Ziolkowska, J. R., Is Desalination Affordable?—Regional Cost and Price Analysis. *Water Resour. Manag.* **2015**, *29*, 1385-1397.
81. Siva Reddy, V.; Kaushik, S. C.; Ranjan, K. R.; Tyagi, S. K., State-of-the-art of solar thermal power plants—A review. *Renewable Sustainable Energy Rev.* **2013**, *27*, 258-273.
82. Köhl, M.; International Energy, A.; Solar, H.; Cooling, P., *Polymeric materials for solar thermal applications*. Wiley-VCH: Weinheim, 2012.
83. Sharon, H.; Reddy, K. S., A review of solar energy driven desalination technologies. *Renewable Sustainable Energy Rev.* **2015**, *41*, 1080-1118.
84. M, C.; Yadav, A., Water desalination system using solar heat: A review. *Renewable Sustainable Energy Rev.* **2017**, *67*, 1308-1330.
85. Zhang, L.; Tang, B.; Wu, J.; Li, R.; Wang, P., Hydrophobic Light-to-Heat Conversion Membranes with Self-Healing Ability for Interfacial Solar Heating. *Adv. Mater.* **2015**, *27*, 4889-4894.
86. Surwade, S. P.; Smirnov, S. N.; Vlassiounk, I. V.; Unocic, R. R.; Veith, G. M.; Dai, S.; Mahurin, S. M., Water desalination using nanoporous single-layer graphene. *Nat. Nanotechnol.* **2015**, *10*, 459.
87. Ni, G.; Li, G.; Boriskina, Svetlana V.; Li, H.; Yang, W.; Zhang, T.; Chen, G., Steam generation under one sun enabled by a floating structure with thermal concentration. *Nat. Energy* **2016**, *1*, 16126.
88. Politano, A.; Argurio, P.; Di Profio, G.; Sanna, V.; Cupolillo, A.; Chakraborty, S.; Arafat, H. A.; Curcio, E., Photothermal Membrane Distillation for Seawater Desalination. *Adv. Mater.* **2017**, *29*, 1603504.
89. Teperik, T. V.; García de Abajo, F. J.; Borisov, A. G.; Abdelsalam, M.; Bartlett, P. N.; Sugawara, Y.; Baumberg, J. J., Omnidirectional absorption in nanostructured metal surfaces. *Nat. Photonics* **2008**, *2*, 299.

90. Aubry, A.; Lei, D. Y.; Fernández-Domínguez, A. I.; Sonnefraud, Y.; Maier, S. A.; Pendry, J. B., Plasmonic Light-Harvesting Devices over the Whole Visible Spectrum. *Nano Letters* **2010**, *10*, 2574-2579.
91. Aydin, K.; Ferry, V. E.; Briggs, R. M.; Atwater, H. A., Broadband polarization-independent resonant light absorption using ultrathin plasmonic super absorbers. *Nat. Commun.* **2011**, *2*, 517.
92. Bae, K.; Kang, G.; Cho, S. K.; Park, W.; Kim, K.; Padilla, W. J., Flexible thin-film black gold membranes with ultrabroadband plasmonic nanofocusing for efficient solar vapour generation. *Nat. Commun.* **2015**, *6*, 10103.
93. Zhou, L.; Tan, Y.; Wang, J.; Xu, W.; Yuan, Y.; Cai, W.; Zhu, S.; Zhu, J., 3D self-assembly of aluminium nanoparticles for plasmon-enhanced solar desalination. *Nat. Photonics* **2016**, *10*, 393.
94. Zhou, L.; Zhuang, S.; He, C.; Tan, Y.; Wang, Z.; Zhu, J., Self-assembled spectrum selective plasmonic absorbers with tunable bandwidth for solar energy conversion. *Nano Energy* **2017**, *32*, 195-200.
95. Tian, L.; Luan, J.; Liu, K.-K.; Jiang, Q.; Tadepalli, S.; Gupta, M. K.; Naik, R. R.; Singamaneni, S., Plasmonic Biofoam: A Versatile Optically Active Material. *Nano Letters* **2016**, *16*, 609-616.
96. Richardson, H. H.; Hickman, Z. N.; Govorov, A. O.; Thomas, A. C.; Zhang, W.; Kordesch, M. E., Thermo-optical Properties of Gold Nanoparticles Embedded in Ice: Characterization of Heat Generation and Melting. *Nano Letters* **2006**, *6*, 783-788.
97. Govorov, A. O.; Richardson, H. H., Generating heat with metal nanoparticles. *Nano Today* **2007**, *2*, 30-38.
98. Neumann, O.; Feronti, C.; Neumann, A. D.; Dong, A.; Schell, K.; Lu, B.; Kim, E.; Quinn, M.; Thompson, S.; Grady, N.; Nordlander, P.; Oden, M.; Halas, N. J., Compact solar autoclave based on steam generation using broadband light-harvesting nanoparticles. *Proc. Natl. Acad. Sci.* **2013**, *110*, 11677-11681.
99. Ghasemi, H.; Ni, G.; Marconnet, A. M.; Loomis, J.; Yerci, S.; Miljkovic, N.; Chen, G., Solar steam generation by heat localization. *Nat. Commun.* **2014**, *5*, ncomms5449.
100. Zhu, M.; Li, Y.; Chen, F.; Zhu, X.; Dai, J.; Li, Y.; Yang, Z.; Yan, X.; Song, J.; Wang, Y.; Hitz, E.; Luo, W.; Lu, M.; Yang, B.; Hu, L., Plasmonic Wood for High-Efficiency Solar Steam Generation. *Adv. Energy Mater.* **2018**, *8*, 1701028.
101. Linic, S.; Aslam, U.; Boerigter, C.; Morabito, M., Photochemical transformations on plasmonic metal nanoparticles. *Nat. Mater.* **2015**, *14*, 567.

102. Liu, G.; Xu, J.; Wang, K., Solar water evaporation by black photothermal sheets. *Nano Energy* **2017**, *41*, 269-284.
103. Wang, X.; He, Y.; Liu, X.; Cheng, G.; Zhu, J., Solar steam generation through bio-inspired interface heating of broadband-absorbing plasmonic membranes. *Appl. Energy* **2017**, *195*, 414-425.
104. Ito, Y.; Tanabe, Y.; Han, J.; Fujita, T.; Tanigaki, K.; Chen, M., Multifunctional Porous Graphene for High-Efficiency Steam Generation by Heat Localization. *Adv. Mater.* **2015**, *27*, 4302-4307.
105. Li, X.; Xu, W.; Tang, M.; Zhou, L.; Zhu, B.; Zhu, S.; Zhu, J., Graphene oxide-based efficient and scalable solar desalination under one sun with a confined 2D water path. *Proc. Natl. Acad. Sci.* **2016**, *113*, 13953.
106. Wang, X.; Ou, G.; Wang, N.; Wu, H., Graphene-based Recyclable Photo-Absorbers for High-Efficiency Seawater Desalination. *ACS Appl. Mater. Interfaces* **2016**, *8*, 9194-9199.
107. Hu, X.; Xu, W.; Zhou, L.; Tan, Y.; Wang, Y.; Zhu, S.; Zhu, J., Tailoring Graphene Oxide-Based Aerogels for Efficient Solar Steam Generation under One Sun. *Adv. Mater.* **2017**, *29*, 1604031.
108. Wang, G.; Fu, Y.; Guo, A.; Mei, T.; Wang, J.; Li, J.; Wang, X., Reduced Graphene Oxide–Polyurethane Nanocomposite Foam as a Reusable Photoreceiver for Efficient Solar Steam Generation. *Chem. Mater.* **2017**, *29*, 5629-5635.
109. Zhang, P.; Li, J.; Lv, L.; Zhao, Y.; Qu, L., Vertically aligned graphene sheets membrane for highly efficient solar thermal generation of clean water. *ACS nano* **2017**, *11*, 5087-5093.
110. Yang, J.; Pang, Y.; Huang, W.; Shaw, S. K.; Schiffbauer, J.; Pillers, M. A.; Mu, X.; Luo, S.; Zhang, T.; Huang, Y.; Li, G.; Ptasińska, S.; Lieberman, M.; Luo, T., Functionalized Graphene Enables Highly Efficient Solar Thermal Steam Generation. *ACS Nano* **2017**, *11*, 5510-5518.
111. Moussa, S.; Atkinson, G.; SamyEl-Shall, M.; Shehata, A.; AbouZeid, K. M.; Mohamed, M. B., Laser assisted photocatalytic reduction of metal ions by graphene oxide. *J. Mater. Chem.* **2011**, *21*, 9608-9619.
112. Awad, F. S.; Kiriarachchi, H. D.; AbouZeid, K. M.; Özgür, Ü.; El-Shall, M. S., Plasmonic Graphene Polyurethane Nanocomposites for Efficient Solar Water Desalination. *ACS Appl. Energy Mater.* **2018**, *1*, 976-985.
113. Awad, F. S.; AbouZeid, K. M.; El-Maaty, W. M. A.; El-Wakil, A. M.; El-Shall, M. S., Efficient Removal of Heavy Metals from Polluted Water with High Selectivity for Mercury(II) by 2-Imino-4-thiobiuret–Partially Reduced Graphene Oxide (IT-PRGO). *ACS Appl. Mater. Interfaces* **2017**, *9*, 34230-34242.

114. Hassan, H. M. A.; Abdelsayed, V.; Khder, A. E. R. S.; AbouZeid, K. M.; Turner, J.; El-Shall, M. S.; Al-Resayes, S. I.; El-Azhary, A. A., Microwave synthesis of graphene sheets supporting metal nanocrystals in aqueous and organic media. *J. Mater. Chem.* **2009**, *19*, 3832-3837.
115. Hung, W.-S.; Tsou, C.-H.; De Guzman, M.; An, Q.-F.; Liu, Y.-L.; Zhang, Y.-M.; Hu, C.-C.; Lee, K.-R.; Lai, J.-Y., Cross-Linking with Diamine Monomers To Prepare Composite Graphene Oxide-Framework Membranes with Varying d-Spacing. *Chem. Mater.* **2014**, *26*, 2983-2990.
116. Chandra, V.; Park, J.; Chun, Y.; Lee, J. W.; Hwang, I.-C.; Kim, K. S., Water-Dispersible Magnetite-Reduced Graphene Oxide Composites for Arsenic Removal. *ACS Nano* **2010**, *4*, 3979-3986.
117. Fang, J.; Liu, Q.; Zhang, W.; Gu, J.; Su, Y.; Su, H.; Guo, C.; Zhang, D., Ag/diatomite for highly efficient solar vapor generation under one-sun irradiation. *J. Mater. Chem. A* **2017**, *5*, 17817-17821.
118. Zhou, L.; Tan, Y.; Ji, D.; Zhu, B.; Zhang, P.; Xu, J.; Gan, Q.; Yu, Z.; Zhu, J., Self-assembly of highly efficient, broadband plasmonic absorbers for solar steam generation. *Sci. Adv.* **2016**, *2*, e1501227.
119. Wang, G.; Fu, Y.; Ma, X.; Pi, W.; Liu, D.; Wang, X., Reusable reduced graphene oxide based double-layer system modified by polyethyleneimine for solar steam generation. *Carbon* **2017**, *114*, 117-124.
120. Jiang, Q.; Tian, L.; Liu, K.-K.; Tadepalli, S.; Raliya, R.; Biswas, P.; Naik, R. R.; Singamaneni, S., Bilayered Biofoam for Highly Efficient Solar Steam Generation. *Adv. Mater.* **2016**, *28*, 9400-9407.
121. Xu, N.; Hu, X.; Xu, W.; Li, X.; Zhou, L.; Zhu, S.; Zhu, J., Mushrooms as Efficient Solar Steam-Generation Devices. *Adv. Mater.* **2017**, *29*, 1606762.
122. Hogan, N. J.; Urban, A. S.; Ayala-Orozco, C.; Pimpinelli, A.; Nordlander, P.; Halas, N. J., Nanoparticles Heat through Light Localization. *Nano Letters* **2014**, *14*, 4640-4645.
123. Ghasemi, H.; Ni, G.; Marconnet, A. M.; Loomis, J.; Yerci, S.; Miljkovic, N.; Chen, G., Solar steam generation by heat localization. *Nat. Commun.* **2014**, *5*, 4449.
124. Zhu, M.; Li, Y.; Chen, F.; Zhu, X.; Dai, J.; Li, Y.; Yang, Z.; Yan, X.; Song, J.; Wang, Y.; Hitz, E.; Luo, W.; Lu, M.; Yang, B.; Hu, L., Plasmonic Wood for High-Efficiency Solar Steam Generation. *Adv. Energy Mater.* **2018**, *8*, 1701028.

125. Li, X.; Xu, W.; Tang, M.; Zhou, L.; Zhu, B.; Zhu, S.; Zhu, J., Graphene oxide-based efficient and scalable solar desalination under one sun with a confined 2D water path. *Proc. Natl. Acad. Sci.* **2016**, *113*, 13953-13958.
126. Pongprayoon, T.; O'Rear, E. A.; Yanumet, N.; Yuan, W.-L., Wettability of Cotton Modified by Admicellar Polymerization. *Langmuir* **2003**, *19*, 3770-3778.
127. Chen, S.; Li, X.; Li, Y.; Sun, J., Intumescent Flame-Retardant and Self-Healing Superhydrophobic Coatings on Cotton Fabric. *ACS Nano* **2015**, *9*, 4070-4076.
128. Siqueira, G.; Bras, J.; Dufresne, A., New Process of Chemical Grafting of Cellulose Nanoparticles with a Long Chain Isocyanate. *Langmuir* **2010**, *26*, 402-411.
129. Tursi, A.; Beneduci, A.; Chidichimo, F.; De Vietro, N.; Chidichimo, G., Remediation of hydrocarbons polluted water by hydrophobic functionalized cellulose. *Chemosphere* **2018**, *201*, 530-539.
130. Matolín, V.; Cabala, M.; Matolínová, I.; Škoda, M.; Libra, J.; Václavů, M.; Prince, K. C.; Skála, T.; Yoshikawa, H.; Yamashita, Y.; Ueda, S.; Kobayashi, K., Au⁺ and Au³⁺ ions in CeO₂rf-sputtered thin films. *J. Phys. D: Appl. Phys.* **2009**, *42*, 115301.
131. Matsumoto, T.; Nickut, P.; Tsunoyama, H.; Watanabe, K.; Tsukuda, T.; Al-Shamery, K.; Matsumoto, Y., Thermal and photochemical reactivity of oxygen atoms on gold nanocluster surfaces. *Surf. Sci.* **2007**, *601*, 5226-5231.
132. Deng, Q.; Duan, X.; Ng, D. H. L.; Tang, H.; Yang, Y.; Kong, M.; Wu, Z.; Cai, W.; Wang, G., Ag Nanoparticle Decorated Nanoporous ZnO Microrods and Their Enhanced Photocatalytic Activities. *ACS Appl. Mater. Interfaces* **2012**, *4*, 6030-6037.
133. Schmidt, M.; Masson, A.; Bréchnignac, C., Oxygen and Silver Clusters: Transition from Chemisorption to Oxidation. *Phys. Rev. Lett.* **2003**, *91*, 243401.
134. Agnihotri, S.; Bajaj, G.; Mukherji, S.; Mukherji, S., Arginine-assisted immobilization of silver nanoparticles on ZnO nanorods: an enhanced and reusable antibacterial substrate without human cell cytotoxicity. *Nanoscale* **2015**, *7*, 7415-7429.
135. Abbas, A.; Zhao, Y.; Zhou, J.; Wang, X.; Lin, T., Improving thermal conductivity of cotton fabrics using composite coatings containing graphene, multiwall carbon nanotube or boron nitride fine particles. *Fibers Polym.* **2013**, *14*, 1641-1649.
136. Adham, S.; Hussain, A.; Matar, J. M.; Does, R.; Janson, A., Application of Membrane Distillation for desalting brines from thermal desalination plants. *Desalination* **2013**, *314*, 101-108.
137. Liu, Y.; Wang, X.; Wu, H., High-performance wastewater treatment based on reusable functional photo-absorbers. *Chem. Eng. J.* **2017**, *309*, 787-794.

138. Kiriarachchi, H. D.; Awad, F. S.; Hassan, A. A.; Bobb, J. A.; Lin, A.; El-Shall, M. S., Plasmonic chemically modified cotton nanocomposite fibers for efficient solar water desalination and wastewater treatment. *Nanoscale* **2018**, *10*, 18531-18539.
139. Neumann, O.; Feronti, C.; Neumann, A. D.; Dong, A.; Schell, K.; Lu, B.; Kim, E.; Quinn, M.; Thompson, S.; Grady, N., Compact solar autoclave based on steam generation using broadband light-harvesting nanoparticles. *Proc. Natl. Acad. Sci.* **2013**, *110*, 11677-11681.
140. Janarthanan, B.; Chandrasekaran, J.; Kumar, S., Evaporative heat loss and heat transfer for open- and closed-cycle systems of a floating tilted wick solar still. *Desalination* **2005**, *180*, 291-305.
141. Zedan, A. F.; Moussa, S.; Turner, J.; Atkinson, G.; El-Shall, M. S., Ultrasmall gold nanoparticles anchored to graphene and enhanced photothermal effects by laser irradiation of gold nanostructures in graphene oxide solutions. *ACS Nano* **2012**, *7*, 627-636.
142. Wang, M.; Wang, P.; Zhang, J.; Li, C.; Jin, Y., Ternary Pt/Au/TiO₂-Decorated Plasmonic Wood Carbon for High-Efficiency Interfacial Solar Steam Generation and Photodegradation of Tetracycline. *Chem. Sus. Chem.* **2018**, *12*, 467.
143. Chen, M.; Wu, Y.; Song, W.; Mo, Y.; Lin, X.; He, Q.; Guo, B., Plasmonic nanoparticle-embedded poly (p-phenylene benzobisoxazole) nanofibrous composite films for solar steam generation. *Nanoscale* **2018**, *10*, 6186-6193.
144. Yang, X.; Yang, Y.; Fu, L.; Zou, M.; Li, Z.; Cao, A.; Yuan, Q., An Ultrathin Flexible 2D Membrane Based on Single-Walled Nanotube–MoS₂ Hybrid Film for High-Performance Solar Steam Generation. *Adv. Funct. Mater.* **2018**, *28*, 1704505.
145. Ding, D.; Huang, W.; Song, C.; Yan, M.; Guo, C.; Liu, S., Non-stoichiometric MoO_{3-x} quantum dots as a light-harvesting material for interfacial water evaporation. *Chem. Commun.* **2017**, *53*, 6744-6747.
146. Guo, Z.; Ming, X.; Wang, G.; Hou, B.; Liu, X.; Mei, T.; Li, J.; Wang, J.; Wang, X., Super-hydrophilic copper sulfide films as light absorbers for efficient solar steam generation under one sun illumination. *Semicond. Sci. Technol.* **2018**, *33*, 025008.
147. Yin, Z.; Wang, H.; Jian, M.; Li, Y.; Xia, K.; Zhang, M.; Wang, C.; Wang, Q.; Ma, M.; Zheng, Q.-s.; Zhang, Y., Extremely Black Vertically Aligned Carbon Nanotube Arrays for Solar Steam Generation. *ACS Appl. Mater. Interfaces* **2017**, *9*, 28596-28603.
148. Jia, C.; Li, Y.; Yang, Z.; Chen, G.; Yao, Y.; Jiang, F.; Kuang, Y.; Pastel, G.; Xie, H.; Yang, B.; Das, S.; Hu, L., Rich Mesostructures Derived from Natural Woods for Solar Steam Generation. *Joule* **2017**, *1*, 588-599.

149. Fang, J.; Liu, J.; Gu, J.; Liu, Q.; Zhang, W.; Su, H.; Zhang, D., Hierarchical Porous Carbonized Lotus Seedpods for Highly Efficient Solar Steam Generation. *Chem. Mater.* **2018**, *30*, 6217-6221.
150. Liu, Y.; Chen, J.; Guo, D.; Cao, M.; Jiang, L., Floatable, Self-Cleaning, and Carbon-Black-Based Superhydrophobic Gauze for the Solar Evaporation Enhancement at the Air–Water Interface. *ACS Appl. Mater. Interfaces* **2015**, *7*, 13645-13652.
151. Xu, N.; Hu, X.; Xu, W.; Li, X.; Zhou, L.; Zhu, S.; Zhu, J., Mushrooms as Efficient Solar Steam-Generation Devices. *Adv. Mater.* **2017**, *29*.
152. Xu, L.-L.; Guo, M.-X.; Liu, S.; Bian, S.-W., Graphene/cotton composite fabrics as flexible electrode materials for electrochemical capacitors. *RSC Adv.* **2015**, *5*, 25244-25249.
153. Li, B.; Dai, F.; Xiao, Q.; Yang, L.; Shen, J.; Zhang, C.; Cai, M., Nitrogen-doped activated carbon for a high energy hybrid supercapacitor. *Energy Environ. Sci.* **2016**, *9*, 102-106.
154. Sevilla, M.; Fuertes, A. B., The production of carbon materials by hydrothermal carbonization of cellulose. *Carbon* **2009**, *47*, 2281-2289.
155. Zhang, M.; Wang, C.; Wang, H.; Jian, M.; Hao, X.; Zhang, Y., Carbonized Cotton Fabric for High-Performance Wearable Strain Sensors. *Adv. Funct. Mater.* **2017**, *27*.
156. Chen, Y.; Shi, Y.; Kou, H.; Liu, D.; Huang, Y.; Chen, Z.; Zhang, B., Self-Floating Carbonized Tissue Membrane Derived from Commercial Facial Tissue for Highly Efficient Solar Steam Generation. *ACS Sustainable Chem. Eng.* **2019**, *7*, 2911-2915.
157. Almanza, O.; Rodríguez-Pérez, M. A.; De Saja, J. A., Applicability of the transient plane source method to measure the thermal conductivity of low-density polyethylene foams. *J. Polym. Sci., Part B: Polym. Phys.* **2004**, *42*, 1226-1234.
158. Zhang, S. B.; Wei, S. H.; Zunger, A., Intrinsic n-type versus p-type doping asymmetry and the defect physics of ZnO. *Phys. Rev. B* **2001**, *63*, 075205.
159. Lu, J. G.; Ye, Z. Z.; Zhuge, F.; Zeng, Y. J.; Zhao, B. H.; Zhu, L. P., p-type conduction in N–Al co-doped ZnO thin films. *Appl. Phys. Lett.* **2004**, *85*, 3134-3135.
160. Herring, N. P.; Panchakarla, L. S.; El-Shall, M. S., P-type nitrogen-doped ZnO nanostructures with controlled shape and doping level by facile microwave synthesis. *Langmuir* **2014**, *30*, 2230-2240.
161. Liu, W.; Xiu, F.; Sun, K.; Xie, Y.-H.; Wang, K. L.; Wang, Y.; Zou, J.; Yang, Z.; Liu, J., Na-Doped p-Type ZnO Microwires. *J. Am. Chem. Soc.* **2010**, *132*, 2498-2499.

162. Shen, Z.; Liang, P.; Wang, S.; Liu, L.; Liu, S., Green Synthesis of Carbon-and Silver-Modified Hierarchical ZnO with Excellent Solar Light Driven Photocatalytic Performance. *ACS Sustainable Chem. Eng.* **2015**, *3*, 1010-1016.
163. Vallejos, S.; Pizúrová, N. z. d.; Gràcia, I.; Sotelo-Vazquez, C.; Čechal, J.; Blackman, C.; Parkin, I.; Cané, C., ZnO Rods with Exposed {100} Facets Grown via a Self-Catalyzed Vapor–Solid Mechanism and Their Photocatalytic and Gas Sensing Properties. *ACS Appl. Mater. Interfaces* **2016**, *8*, 33335-33342.
164. Jeem, M.; Zhang, L.; Ishioka, J.; Shibayama, T.; Iwasaki, T.; Kato, T.; Watanabe, S., Tuning Optoelectrical Properties of ZnO Nanorods with Excitonic Defects via Submerged Illumination. *Nano Letters* **2017**, *17*, 2088-2093.
165. King, L. A.; Parkinson, B. A., Probing the Relative Photoinjection Yields of Monomer and Aggregated Dyes into ZnO Crystals. *Langmuir* **2017**, *33*, 468-474.
166. Ahmad, M.; Yingying, S.; Nisar, A.; Sun, H.; Shen, W.; Wei, M.; Zhu, J., Synthesis of hierarchical flower-like ZnO nanostructures and their functionalization by Au nanoparticles for improved photocatalytic and high performance Li-ion battery anodes. *J. Mater. Chem.* **2011**, *21*, 7723-7729.
167. Huang, M. H.; Mao, S.; Feick, H.; Yan, H.; Wu, Y.; Kind, H.; Weber, E.; Russo, R.; Yang, P., Room-Temperature Ultraviolet Nanowire Nanolasers. *Science* **2001**, *292*, 1897-1899.
168. Li, Z.; Yang, R.; Yu, M.; Bai, F.; Li, C.; Wang, Z. L., Cellular Level Biocompatibility and Biosafety of ZnO Nanowires. *J. Phys. Chem. C* **2008**, *112*, 20114-20117.
169. Hong, H.; Wang, F.; Zhang, Y.; Graves, S. A.; Eddine, S. B. Z.; Yang, Y.; Theuer, C. P.; Nickles, R. J.; Wang, X.; Cai, W., Red Fluorescent Zinc Oxide Nanoparticle: A Novel Platform for Cancer Targeting. *ACS Appl. Mater. Interfaces* **2015**, *7*, 3373-3381.
170. Lupan, O.; Postica, V.; Gröttrup, J.; Mishra, A. K.; de Leeuw, N. H.; Carreira, J. F. C.; Rodrigues, J.; Ben Sedrine, N.; Correia, M. R.; Monteiro, T.; Cretu, V.; Tiginyanu, I.; Smazna, D.; Mishra, Y. K.; Adelung, R., Hybridization of Zinc Oxide Tetrapods for Selective Gas Sensing Applications. *ACS Appl. Mater. Interfaces* **2017**, *9*, 4084-4099.
171. Gedamu, D.; Paulowicz, I.; Kaps, S.; Lupan, O.; Wille, S.; Haidarschin, G.; Mishra, Y. K.; Adelung, R., Rapid Fabrication Technique for Interpenetrated ZnO Nanotetrapod Networks for Fast UV Sensors. *Adv. Mater.* **2014**, *26*, 1541-1550.
172. Yu, J.; Yu, X., Hydrothermal Synthesis and Photocatalytic Activity of Zinc Oxide Hollow Spheres. *Environ. Sci. Technol.* **2008**, *42*, 4902-4907.
173. Wang, X.; Hu, P.; Fangli, Y.; Yu, L., Preparation and Characterization of ZnO Hollow Spheres and ZnO–Carbon Composite Materials Using Colloidal Carbon Spheres as Templates. *J. Phys. Chem. C* **2007**, *111*, 6706-6712.

174. Yao, K. X.; Zeng, H. C., ZnO/PVP nanocomposite spheres with two hemispheres. *J. Phys. Chem. C* **2007**, *111*, 13301-13308.
175. Yang, L.; Wang, G.; Tang, C.; Wang, H.; Zhang, L., Synthesis and photoluminescence of corn-like ZnO nanostructures under solvothermal-assisted heat treatment. *Chem. Phys. Lett.* **2005**, *409*, 337-341.
176. Gao, P. X.; Wang, Z. L., Nanopropeller arrays of zinc oxide. *Appl. Phys. Lett.* **2004**, *84*, 2883-2885.
177. Zhang, T.; Dong, W.; Keeter-Brewer, M.; Konar, S.; Njabon, R. N.; Tian, Z. R., Site-Specific Nucleation and Growth Kinetics in Hierarchical Nanosyntheses of Branched ZnO Crystallites. *J. Am. Chem. Soc.* **2006**, *128*, 10960-10968.
178. Li, J.; Lu, G.; Wang, Y.; Guo, Y.; Guo, Y., A high activity photocatalyst of hierarchical 3D flowerlike ZnO microspheres: Synthesis, characterization and catalytic activity. *J. Colloid Interface Sci.* **2012**, *377*, 191-196.
179. Rahman, Q. I.; Ahmad, M.; Misra, S. K.; Lohani, M. B., Hexagonal ZnO nanorods assembled flowers for photocatalytic dye degradation: Growth, structural and optical properties. *Superlattices Microstruct.* **2013**, *64*, 495-506.
180. Li, B.; Wang, Y., Facile Synthesis and Enhanced Photocatalytic Performance of Flower-like ZnO Hierarchical Microstructures. *J. Phys. Chem. C* **2010**, *114*, 890-896.
181. Umar, A.; Lee, S.; Im, Y. H.; Hahn, Y. B., Flower-shaped ZnO nanostructures obtained by cyclic feeding chemical vapour deposition: structural and optical properties. *Nanotechnol.* **2005**, *16*, 2462.
182. Bahng, J. H.; Yeom, B.; Wang, Y.; Tung, S. O.; Hoff, J. D.; Kotov, N., Anomalous dispersions of 'hedgehog' particles. *Nature* **2015**, *517*, 596-599.
183. Jiechao, G.; Bo, T.; Linhai, Z.; Zhiqiang, S., A rapid hydrothermal route to sisal-like 3D ZnO nanostructures via the assembly of CTA + and Zn(OH)₄²⁻: growth mechanism and photoluminescence properties. *Nanotechnol.* **2006**, *17*, 1316.
184. Herring, N. P.; AbouZeid, K.; Mohamed, M. B.; Pinski, J.; El-Shall, M. S., Formation mechanisms of gold–zinc oxide hexagonal nanopyrramids by heterogeneous nucleation using microwave synthesis. *Langmuir* **2011**, *27*, 15146-15154.
185. Sun, Y.; Hu, J.; Wang, N.; Zou, R.; Wu, J.; Song, Y.; Chen, H.; Chen, H.; Chen, Z., Controllable hydrothermal synthesis, growth mechanism, and properties of ZnO three-dimensional structures. *New J. Chem.* **2010**, *34*, 732-737.

186. Ajmal, A.; Majeed, I.; Malik, R. N.; Idriss, H.; Nadeem, M. A., Principles and mechanisms of photocatalytic dye degradation on TiO₂ based photocatalysts: a comparative overview. *RSC Adv.* **2014**, *4*, 37003-37026.
187. Baruah, S.; Jaisai, M.; Imani, R.; Nazhad, M. M.; Dutta, J., Photocatalytic paper using zinc oxide nanorods. *Sci. Technol. Adv. Mater.* **2010**, *11*, 055002.
188. Li, Q.; Kumar, V.; Li, Y.; Zhang, H.; Marks, T. J.; Chang, R. P. H., Fabrication of ZnO Nanorods and Nanotubes in Aqueous Solutions. *Chem. Mater.* **2005**, *17*, 1001-1006.
189. Lin, H.; Huang, C. P.; Li, W.; Ni, C.; Shah, S. I.; Tseng, Y.-H., Size dependency of nanocrystalline TiO₂ on its optical property and photocatalytic reactivity exemplified by 2-chlorophenol. *Appl. Catal., B* **2006**, *68*, 1-11.
190. Jiang, P.; Zhou, J. J.; Fang, H. F.; Wang, C. Y.; Wang, Z. L.; Xie, S. S., Hierarchical Shelled ZnO Structures Made of Bunched Nanowire Arrays. *Adv. Funct. Mater.* **2007**, *17*, 1303-1310.
191. Degen, A.; Kosec, M., Effect of pH and impurities on the surface charge of zinc oxide in aqueous solution. *J. Eur. Ceram. Soc.* **2000**, *20*, 667-673.
192. Zhang, X.; Qin, J.; Hao, R.; Wang, L.; Shen, X.; Yu, R.; Limpanart, S.; Ma, M.; Liu, R., Carbon-Doped ZnO Nanostructures: Facile Synthesis and Visible Light Photocatalytic Applications. *J. Phys. Chem. C* **2015**, *119*, 20544-20554.
193. Hariharan, C., Photocatalytic degradation of organic contaminants in water by ZnO nanoparticles: Revisited. *Appl. Catal., A* **2006**, *304*, 55-61.
194. Sun, S. H., Recent advances in chemical synthesis, self-assembly, and applications of FePt nanoparticles. *Adv. Mater.* **2006**, *18*, 393-403.
195. Terris, B. D.; Thomson, T., Nanofabricated and self-assembled magnetic structures as data storage media. *J. Phys. D: Appl. Phys.* **2005**, *38*, R199-R222.
196. Gupta, A. K.; Gupta, M., Synthesis and surface engineering of iron oxide nanoparticles for biomedical applications. *Biomaterials* **2005**, *26*, 3995-4021.
197. Pankhurst, Q. A.; Connolly, J.; Jones, S. K.; Dobson, J., Applications of magnetic nanoparticles in biomedicine. *J. Phys. D: Appl. Phys.* **2003**, *36*, R167-R181.
198. Bulte, J. W. M.; Kraitchman, D. L., Iron oxide MR contrast agents for molecular and cellular imaging. *NMR Biomed.* **2004**, *17*, 484-499.
199. Polshettiwar, V.; Varma, R. S., Green chemistry by nano-catalysis. *Green Chemistry* **2010**, *12*, 743-754.

200. Yang, C.; Zhao, H.; Hou, Y.; Ma, D., Fe₅C₂ nanoparticles: a facile bromide-induced synthesis and as an active phase for Fischer–Tropsch synthesis. *J. Am. Chem. Soc.* **2012**, *134*, 15814-15821.
201. Li, C.; Sayaka, I.; Chisato, F.; Fujimoto, K., Development of high performance graphite-supported iron catalyst for Fischer-Tropsch synthesis. *Appl. Catal., A* **2016**, *509*, 123-129.
202. Wang, H.; Zhou, W.; Liu, J.-X.; Si, R.; Sun, G.; Zhong, M.-Q.; Su, H.-Y.; Zhao, H.-B.; Rodriguez, J. A.; Penneycook, S. J.; Idrobo, J.-C.; Li, W.-X.; Kou, Y.; Ma, D., Platinum-Modulated Cobalt Nanocatalysts for Low-Temperature Aqueous-Phase Fischer–Tropsch Synthesis. *J. Am. Chem. Soc.* **2013**, *135*, 4149-4158.
203. Wu, C.; Yin, P.; Zhu, X.; OuYang, C.; Xie, Y., Synthesis of hematite (alpha-Fe₂O₃) nanorods: Diameter-size and shape effects on their applications in magnetism, lithium ion battery, and gas sensors. *J. Phys. Chem. B* **2006**, *110*, 17806-17812.
204. Sugawara, T.; Matsushita, M. M., Spintronics in organic pi-electronic systems. *J. Mater. Chem.* **2009**, *19*, 1738-1753.
205. Peng, E.; Wang, F.; Xue, J. M., Nanostructured magnetic nanocomposites as MRI contrast agents. *J. Mater. Chem. B* **2015**, *3*, 2241-2276.
206. Yu, J.; Yang, C.; Li, J.; Ding, Y.; Zhang, L.; Yousaf, M. Z.; Lin, J.; Pang, R.; Wei, L.; Xu, L.; Sheng, F.; Li, C.; Li, G.; Zhao, L.; Hou, Y., Multifunctional Fe₅C₂ nanoparticles: a targeted theranostic platform for magnetic resonance imaging and photoacoustic tomography-guided photothermal therapy. *Adv. Mater. (Weinheim, Ger.)* **2014**, *26*, 4114-4120.
207. Tang, W.; Zhen, Z.; Yang, C.; Wang, L.; Cowger, T.; Chen, H.; Todd, T.; Hekmatyar, K.; Zhao, Q.; Hou, Y.; Xie, J., Fe₅C₂ Nanoparticles with High MRI Contrast Enhancement for Tumor Imaging. *Small* **2014**, *10*, 1245-1249.
208. Huang, G.; Hu, J.; Zhang, H.; Zhou, Z.; Chi, X.; Gao, J., Highly magnetic iron carbide nanoparticles as effective T2 contrast agents. *Nanoscale* **2014**, *6*, 726-730.
209. Yu, J.; Ju, Y.; Zhao, L.; Chu, X.; Yang, W.; Tian, Y.; Sheng, F.; Lin, J.; Liu, F.; Dong, Y.; Hou, Y., Multistimuli-Regulated Photochemothermal Cancer Therapy Remotely Controlled via Fe₅C₂ Nanoparticles. *ACS Nano* **2015**, Ahead of Print.
210. Yu, J.; Huang, D.-Y.; Yousaf, M. Z.; Hou, Y.-L.; Gao, S., Magnetic nanoparticle-based cancer therapy. *Chin. Phys. B* **2013**, *22*, 027506/1-027506/12.
211. Chen, H.; Zhen, Z.; Todd, T.; Chu, P. K.; Xie, J., Nanoparticles for improving cancer diagnosis. *Materials Science and Engineering: R: Reports* **2013**, *74*, 35-69.

212. Pham, T. H.; Qi, Y.; Yang, J.; Duan, X.; Qian, G.; Zhou, X.; Chen, D.; Yuan, W., Insights into Hägg Iron-Carbide-Catalyzed Fischer–Tropsch Synthesis: Suppression of CH₄ Formation and Enhancement of C–C Coupling on χ -Fe₅C₂ (510). *ACS Catal.* **2015**, *5*, 2203-2208.
213. Pham, T. H.; Duan, X.; Qian, G.; Zhou, X.; Chen, D., CO Activation Pathways of Fischer-Tropsch Synthesis on χ -Fe₅C₂ (510): Direct versus Hydrogen-Assisted CO Dissociation. *J. Phys. Chem. C* **2014**, *118*, 10170-10176.
214. Park, H.; Youn, D. H.; Kim, J. Y.; Kim, W. Y.; Choi, Y. H.; Lee, Y. H.; Choi, S. H.; Lee, J. S., Selective Formation of Haegg Iron Carbide with g-C₃N₄ as a Sacrificial Support for Highly Active Fischer-Tropsch Synthesis. *ChemCatChem* **2015**, *7*, 3488-3494.
215. Hong, S. Y.; Chun, D. H.; Yang, J.-I.; Jung, H.; Lee, H.-T.; Hong, S.; Jang, S.; Lim, J. T.; Kim, C. S.; Park, J. C., A new synthesis of carbon encapsulated Fe₅C₂ nanoparticles for high-temperature Fischer-Tropsch synthesis. *Nanoscale* **2015**, *7*, 16616-16620.
216. Aldrich, M. V.; Gardea-Torresdey, J. L.; Peralta-Videa, J. R.; Parsons, J. G., Uptake and Reduction of Cr(VI) to Cr(III) by Mesquite (*Prosopis* spp.): Chromate–Plant Interaction in Hydroponics and Solid Media Studied Using XAS. *Environ. Sci. Technol.* **2003**, *37*, 1859-1864.
217. Paustenbach, D. J.; Sheehan, P. J.; Pauli, J. M.; Wisser, L. M.; Finley, B. L., Review of the allergic contact dermatitis hazard posed by chromium-contaminated soil: Identifying a “safe” concentration. *J. Toxicol. Environ. Health* **1992**, *37*, 177-207.
218. Hartwig, A.; Schwerdtle, T., Interactions by carcinogenic metal compounds with DNA repair processes: toxicological implications. *Toxicol. Lett.* **2002**, *127*, 47-54.
219. Rengaraj, S.; Joo, C. K.; Kim, Y.; Yi, J., Kinetics of removal of chromium from water and electronic process wastewater by ion exchange resins: 1200H, 1500H and IRN97H. *J. Hazard. Mater.* **2003**, *102*, 257-275.
220. Rengaraj, S.; Yeon, K.-H.; Moon, S.-H., Removal of chromium from water and wastewater by ion exchange resins. *J. Hazard. Mater.* **2001**, *87*, 273-287.
221. Modrzejewska, Z.; Kaminski, W., Separation of Cr(VI) on Chitosan Membranes. *Ind. Eng. Chem. Res.* **1999**, *38*, 4946-4950.
222. Rad, S. M.; Mirbagheri, S.; Mohammadi, T., Using reverse osmosis membrane for chromium removal from aqueous solution. *World Acad. Sci. Eng. Technol* **2009**, *3*, 332-336.
223. Gao, P.; Chen, X.; Shen, F.; Chen, G., Removal of chromium (VI) from wastewater by combined electrocoagulation–electroflotation without a filter. *Sep. Purif. Technol.* **2005**, *43*, 117-123.

224. Pan, C.; Troyer, L. D.; Catalano, J. G.; Giammar, D. E., Dynamics of chromium (VI) removal from drinking water by iron electrocoagulation. *Environ. Sci. Technol.* **2016**, *50*, 13502-13510.
225. Pan, C.; Troyer, L. D.; Liao, P.; Catalano, J. G.; Li, W.; Giammar, D. E., Effect of humic acid on the removal of chromium (VI) and the production of solids in iron electrocoagulation. *Environ. Sci. Technol.* **2017**, *51*, 6308-6318.
226. Jiang, W.; Cai, Q.; Xu, W.; Yang, M.; Cai, Y.; Dionysiou, D. D.; O'Shea, K. E., Cr (VI) adsorption and reduction by humic acid coated on magnetite. *Environ. Sci. Technol.* **2014**, *48*, 8078-8085.
227. Kousalya, G.; Gandhi, M. R.; Meenakshi, S., Removal of toxic Cr (VI) ions from aqueous solution using nano-hydroxyapatite-based chitin and chitosan hybrid composites. *Adsorpt. Sci. Technol.* **2010**, *28*, 49-64.
228. Chowdhury, S. R.; Yanful, E. K., Arsenic and chromium removal by mixed magnetite–maghemite nanoparticles and the effect of phosphate on removal. *J. Environ. Manage.* **2010**, *91*, 2238-2247.
229. Jiang, W.; Pelaez, M.; Dionysiou, D. D.; Entezari, M. H.; Tsoutsou, D.; O'Shea, K., Chromium (VI) removal by maghemite nanoparticles. *Chem. Eng. J.* **2013**, *222*, 527-533.
230. Sharma, Y.; Srivastava, V., Comparative studies of removal of Cr (VI) and Ni (II) from aqueous solutions by magnetic nanoparticles. *J. Chem. Eng. Data* **2010**, *56*, 819-825.
231. Zhu, J.; Wei, S.; Gu, H.; Rapole, S. B.; Wang, Q.; Luo, Z.; Haldolaarachchige, N.; Young, D. P.; Guo, Z., One-pot synthesis of magnetic graphene nanocomposites decorated with core@double-shell nanoparticles for fast chromium removal. *Environ. Sci. Technol.* **2011**, *46*, 977-985.
232. Gupta, V.; Agarwal, S.; Saleh, T. A., Chromium removal by combining the magnetic properties of iron oxide with adsorption properties of carbon nanotubes. *Water Res.* **2011**, *45*, 2207-2212.
233. Huang, J.; Cao, Y.; Shao, Q.; Peng, X.; Guo, Z., Magnetic nanocarbon adsorbents with enhanced hexavalent chromium removal: morphology dependence of fibrillar vs particulate structures. *Ind. Eng. Chem. Res.* **2017**, *56*, 10689-10701.
234. Rajput, S.; Pittman Jr, C. U.; Mohan, D., Magnetic magnetite (Fe₃O₄) nanoparticle synthesis and applications for lead (Pb²⁺) and chromium (Cr⁶⁺) removal from water. *J. Colloid Interface Sci.* **2016**, *468*, 334-346.
235. Gao, F.; Gu, H.; Wang, H.; Wang, X.; Xiang, B.; Guo, Z., Magnetic amine-functionalized polyacrylic acid-nanomagnetite for hexavalent chromium removal from polluted water. *RSC Adv.* **2015**, *5*, 60208-60219.

236. Shang, J.; Pi, J.; Zong, M.; Wang, Y.; Li, W.; Liao, Q., Chromium removal using magnetic biochar derived from herb-residue. *J. Taiwan Inst. Chem. Eng.* **2016**, *68*, 289-294.
237. Shih, Y.-C.; Ke, C.-Y.; Yu, C.-J.; Lu, C.-Y.; Tseng, W.-L., Combined Tween 20-Stabilized Gold Nanoparticles and Reduced Graphite Oxide–Fe₃O₄ Nanoparticle Composites for Rapid and Efficient Removal of Mercury Species from a Complex Matrix. *ACS Appl. Mater. Interfaces* **2014**, *6*, 17437-17445.
238. Zare-Dorabei, R.; Rahimi, R.; Koochi, A.; Zargari, S., Preparation and characterization of a novel tetrakis(4-hydroxyphenyl)porphyrin–graphene oxide nanocomposite and application in an optical sensor and determination of mercury ions. *RSC Adv.* **2015**, *5*, 93310-93317.
239. Kabiri, S.; Tran, D. N. H.; Azari, S.; Losic, D., Graphene-Diatom Silica Aerogels for Efficient Removal of Mercury Ions from Water. *ACS Appl. Mater. Interfaces* **2015**, *7*, 11815-11823.
240. Gao, H.; Sun, Y.; Zhou, J.; Xu, R.; Duan, H., Mussel-Inspired Synthesis of Polydopamine-Functionalized Graphene Hydrogel as Reusable Adsorbents for Water Purification. *ACS Appl. Mater. Interfaces* **2013**, *5*, 425-432.
241. Tadjarodi, A.; Moazen Ferdowsi, S.; Zare-Dorabei, R.; Barzin, A., Highly efficient ultrasonic-assisted removal of Hg(II) ions on graphene oxide modified with 2-pyridinecarboxaldehyde thiosemicarbazone: Adsorption isotherms and kinetics studies. *Ultrason. Sonochem.* **2016**, *33*, 118-128.
242. Marcano, D. C.; Kosynkin, D. V.; Berlin, J. M.; Sinitskii, A.; Sun, Z.; Slesarev, A.; Alemany, L. B.; Lu, W.; Tour, J. M., Improved Synthesis of Graphene Oxide. *ACS Nano* **2010**, *4*, 4806-4814.
243. Jia, C.-J.; Sun, L.-D.; Luo, F.; Han, X.-D.; Heyderman, L. J.; Yan, Z.-G.; Yan, C.-H.; Zheng, K.; Zhang, Z.; Takano, M.; Hayashi, N.; Eltschka, M.; Kläui, M.; Rüdiger, U.; Kasama, T.; Cervera-Gontard, L.; Dunin-Borkowski, R. E.; Tzvetkov, G.; Raabe, J., Large-Scale Synthesis of Single-Crystalline Iron Oxide Magnetic Nanorings. *J. Am. Chem. Soc.* **2008**, *130*, 16968-16977.
244. Ferrari, A. C.; Meyer, J.; Scardaci, V.; Casiraghi, C.; Lazzeri, M.; Mauri, F.; Piscanec, S.; Jiang, D.; Novoselov, K.; Roth, S., Raman spectrum of graphene and graphene layers. *Phys. Rev. Lett.* **2006**, *97*, 187401.
245. El-Gendy, A. A.; Qian, M.; Huba, Z. J.; Khanna, S. N.; Carpenter, E. E., Enhanced magnetic anisotropy in cobalt-carbide nanoparticles. *Appl. Phys. Lett.* **2014**, *104*, 023111.
246. El-Gendy, A. A.; Almugaiteeb, T.; Carpenter, E. E., CoxC nanorod magnets: Highly magnetocrystalline anisotropy with lower Curie temperature for potential applications. *J. Magn. Mater.* **2013**, *348*, 136-139.

247. Yuan, P.; Fan, M.; Yang, D.; He, H.; Liu, D.; Yuan, A.; Zhu, J.; Chen, T., Montmorillonite-supported magnetite nanoparticles for the removal of hexavalent chromium [Cr (VI)] from aqueous solutions. *J. Hazard. Mater.* **2009**, *166*, 821-829.
248. Gopalakannan, V.; Periyasamy, S.; Viswanathan, N., One pot eco-friendly synthesis of highly dispersed alumina supported alginate biocomposite for efficient chromium (VI) removal. *Journal of Water Process Engineering* **2016**, *10*, 113-119.
249. Cao, X.; Wang, W.; Zhang, X.; Li, L.; Cheng, Y.; Liu, H.; Du, S.; Zheng, R., Magnetic properties of fluffy Fe@ α -Fe₂O₃ core-shell nanowires. *Nanoscale Res. Lett.* **2013**, *8*, 423.
250. López-Téllez, G.; Barrera-Díaz, C. E.; Balderas-Hernández, P.; Roa-Morales, G.; Bilyeu, B., Removal of hexavalent chromium in aquatic solutions by iron nanoparticles embedded in orange peel pith. *Chem. Eng. J.* **2011**, *173*, 480-485.
251. Moradi, M.; Dehpahlavan, A.; Rezaei Kalantary, R.; Ameri, A.; Farzadkia, M.; Izanloo, H., Application of modified bentonite using sulfuric acid for the removal of hexavalent chromium from aqueous solutions. *Environ. Health Eng. Manage. J.* **2015**, *2*, 99-106.
252. Gandhi, M. R.; Viswanathan, N.; Meenakshi, S., Preparation and application of alumina/chitosan biocomposite. *Int. J. Biol. Macromol.* **2010**, *47*, 146-154.
253. Escudero, C.; Fiol, N.; Villaescusa, I.; Bollinger, J.-C., Effect of chromium speciation on its sorption mechanism onto grape stalks entrapped into alginate beads. *Arabian J. Chem.* **2017**, *10*, S1293-S1302.
254. Gandhi, M. R.; Meenakshi, S., Preparation and characterization of La (III) encapsulated silica gel/chitosan composite and its metal uptake studies. *J. Hazard. Mater.* **2012**, *203*, 29-37.
255. Li, C.; Du, Z.; Zou, W.; Li, H.; Zhang, C., Fabrication of copper coated polymer foam and their application for hexavalent chromium removal. *React. Funct. Polym.* **2015**, *88*, 24-30.

Vita

Hiran Danushka Kiriarachchi was born on January 6th, 1987, in Negombo, Sri Lanka, and is a Sri Lankan citizen. He graduated from Pannala National School, Pannala, Sri Lanka in 2005. He received his Bachelor of Science in Chemistry from University of Kelaniya, Dalugama, Kelaniya, Sri Lanka in 2013. He joined Virginia Commonwealth University in 2014 as a graduate student. The title of his thesis is “Nanostructured Materials for Photocatalysis, Water Treatment, and Solar Desalination” and Dr. M. Samy El-Shall was his principal doctoral advisor.

Selected Publications and Presentations

- [1] **Kiriarachchi, H. D.**; Awad, F. S.; Hassan, A. A.; Bobb, J., A.; Lin, A; El-Shall, M., S. “Plasmonic Chemically Modified Cotton Nanocomposite Fibers for Efficient Solar Water Desalination and Wastewater Treatment” *Nanoscale* **2018**, 10, 18531-18539.
- [2] Awad, F.; **Kiriarachchi, H. D.**; AbouZeid, K. M.; Ozgur, U.; El-Shall, M. S. “Plasmonic Graphene Polyurethane Nanocomposites for Efficient Solar Water Desalination” *ACS Applied Energy Materials* **2018**, 1, 976-985. (Co-first author)
- [3] **Kiriarachchi, H. D.**; AbouZeid, K. M.; El-Shall, M. S. “Growth Mechanism of ‘Sea Urchin’ Shaped ZnO Nanostructures and their Photocatalytic Activity in the Degradation of Organic Dyes” 254th ACS National Meeting, Washington, DC, 08/20/2017-08/24/2017, Poster Presentation.

Professional Experience

Graduate Research Assistant , <i>Virginia Commonwealth University</i>	<i>May 2017 - Present</i>
Graduate Teaching Assistant , <i>Virginia Commonwealth University</i>	<i>Aug. 2014 – May 2017</i>
Teaching Assistant , <i>University of Kelaniya</i>	<i>Apr. 2013- June 2014</i>

Awards and Scholarships

Dissertation Assistantship Award, Graduate School of Virginia Commonwealth University (2018-2019)

Altria Fellowship, Department of Chemistry, Virginia Commonwealth University (2018-2019)

Distinguished Chemist Fund Award, Department of Chemistry, Virginia Commonwealth University (2018)